2020-04-13

Superconductivity at its Limit: Simulating Superconductor Dynamics Near the Superconducting Superheating Field in Eilenberger and Ginzburg-Landau Theory

Alden Roy Pack
Brigham Young University

Superconductivity at its Limit: Simulating Superconductor Dynamics Near the Superconducting Superheating Field in Eilenberger and Ginzburg-Landau Theory

Alden Roy Pack

A dissertation submitted to the faculty of
Brigham Young University
in partial fulfillment of the requirements for the degree of

Doctor of Philosophy

Mark Transtrum, Advisor
Richard Hennig
Branton Campbell
Eric Hirschmann
Jean-Francois Van Huele

Department of Physics and Astronomy

Brigham Young University

ABSTRACT

Superconductivity at its Limit: Simulating Superconductor Dynamics Near the Superconducting Superheating Field in Eilenberger and Ginzburg-Landau Theory

Alden Roy Pack
Department of Physics and Astronomy, BYU
Doctor of Philosophy

We computationally explore the dynamics of superconductivity near the superheating field in two ways. First, we use a finite element method to solve the time-dependent Ginzburg-Landau equations of superconductivity. We present a novel way to evaluate the superheating field H_{sh} and the critical mode that leads to vortex nucleation using saddle-node bifurcation theory. We simulate how surface roughness, grain boundaries, and islands of deficient Sn change those results in 2 and 3 spatial dimensions. We study how AC magnetic fields and heat waves impact vortex movement. Second, we use automatic differentiation to abstract away the details of deriving the equations of motion and stability for Ginzburg-Landau and Eilenberger theory. We present calculations of H_{sh} and the critical wavenumber using linear stability analysis.

Keywords: superconductivity, superheating field, linear stability analysis, finite element methods, Ginzburg-Landau theory, Eilenberger Theory

ACKNOWLEDGMENTS

I'd like to thank Mark Transtrum for the good advice, words of encouragement, and hard work. He had a lot of students and it meant a lot to me that he made time to help when it was needed. I'd like to thank my committee for taking time to review this work and ensure it is of good quality. I'd like to thank all the many professors who were patient enough to take time outside of classes to help me understand the material. I'd also like to thank Nan Ellen AhYou for making sure students had a safe and comfortable experience. She reached out in small ways that had a large impact. I'd like to thank Shelena Shamo for guiding graduate students through administrative requirements. Finally, I'd like to thank my wife for being patient when I worked late, for always having a listening ear, and for being a joint provider.

Contents

List of Figures

List of Tables

Chapter 1

Introduction

In the development of new technology materials are often pushed to their limits. Metal in jet turbines must withstand more heat and stress, batteries must hold more and more charge, etc. Similarly, superconductors are being pushed to operate at large magnetic fields and high temperatures.

In this dissertation we develop computational methods to bridge the gap between experimental observations of superconductors in extreme conditions and the theories that describe them. Some physics is small, fast, and difficult measure accurately in a lab. Though theory brings additional insight there are limitations to what can be understood using pen and paper. By transforming theoretical problems into something a computer can process, we find approximate solutions to the complicated equations that describe superconductivity. In other words, we simulate physics that is hard to measure.

In the rest of this chapter we review the historical context for the theories we study. Then we discuss how the various phases of superconductivity are described by these theories and review recent relevant literature. Having given a brief background, we review our research goals and the organization of the rest of the dissertation. Finally, we describe the impact of this work on society and how this work is part of a larger collaboration.

1.1 Historical Context

The two hallmark features of superconductivity are zero resistance and perfect diamagnetism. The first was discovered by Kamerlingh Onnes in 1911 [1]. The second was found by Walther Meissner and Robert Ochsenfeld in 1933 and is known as the "Meissner effect" [2].

Since then there has been a large effort to theoretically explain superconductivity. In 1950 Ginzburg and Landau developed a phenomenological theory describing superconductivity as a Taylor series of a superconducting complex order parameter [3]. Due to its ability to capture mesoscopic behavior while maintaining relative simplicity Ginzburg-Landau (GL) theory remains a popular tool for modeling superconductivity today.

Despite the power of GL theory, it does not actually explain how superconductivity arises. The first theory to describe the microscopic origin of superconductivity is BCS theory [4]. Bardeen, Cooper, and Schrieffer showed that if there was a net attractive force between two electrons then they could from Cooper pairs. These Cooper pairs can form a Bose-Einstein condensate that leads to superconductivity. In this dissertation we are interested in mesoscopic scales so we will not discuss BCS theory further.

Since then theories have become increasingly complicated in order to correctly match what has been observed experimentally. Gorkov generalized BCS theory to fit in a quantum field theoretical framework and showed that GL theory could be derived from microscopic theories in the limit that the temperature approaches T_c [5, 6]. Eliashberg generalized Gorkov theory to include strong coupling between electrons and phonons [7].

Though the last two theories are very general, their complexity makes them difficult to work with computationally. In this dissertation we will focus on two simpler theories. The first is GL theory. As the simplest of all the theories mentioned, it is easy to make mesoscopic simulations of defects while still capturing interesting behavior like vortex nucleation. The second is Eilenberger theory [8]. Eilenberger theory is less complicated than Gorkov theory but is accurate for low

temperatures unlike GL theory.

In the next section we give an overview of the physics these theories describe. We leave the specific details of Eilenberger theory to chapter 5 and the details of GL theory to chapter 2.

1.2 Phases of superconductivity

This section is intended as a reference for terminology the reader may not be familiar with. It follows a similar section from my masters thesis. [9].

The utility of these two theories is their ability to mesoscopically describe superconductivity. Both can be formulated as differences between the free energy of the superconducting and nonsuperconducting states. (In the future any time we mention free energies we mean the difference between the superconducting and nonsuperconducting free energies). These free energies depend on an order parameter Δ and a magnetic vector potential $\mathbf{A}$. The order parameter is related to the local density of superconducting electrons and the curl of the magnetic vector potential gives the magnetic field. For GL theory the order parameter is often referred to as ψ. The characteristic lengths of Δ and $\mathbf{A}$ are the coherence length ξ and the penetration depth λ respectively. In Eilenberger theory ξ and λ depend on temperature.

Taking the first variation of the free energies with respect to Δ and $\mathbf{A}$ produces equations of motion used to calculate Δ and $\mathbf{A}$. The second variation contains information on the stability of the system. For small magnetic fields Δ will be nonzero, indicating a superconducting state. For large magnetic fields Δ will drop to zero, indicating a loss of superconductivity.

The critical magnetic field H_c occurs when the contributions of the magnetic field cancel out the contributions of Δ in the free energy. Below H_c the system persists in a purely superconducting state (Meissner state). Above H_c it is energetically favorable to allow magnetic flux into the superconductor. Depending on the geometry it is possible for superconductivity to persist beyond

H_c in a metastable state due an energy barrier [10]. The magnetic field at which the metastable state vanishes is the superheating field H_{sh}.

The intermediate behavior between superconducting and nonsuperconducting states is determined by $\kappa = \frac{\lambda}{\xi}$. Type I superconductors are characterized by $\kappa < \frac{1}{\sqrt{2}}$ while type II superconductors have $\kappa > \frac{1}{\sqrt{2}}$. Transtrum numerically created Fig. 1.1 within GL theory based on an infinite superconducting slab (half of space filled with vacuum and half of space filled with a superconducting material) [11]. As the external magnetic field increases, a type I superconductor has only one critical field strength H_c. Type II superconductors have two critical field strengths, H_{c1} and H_{c2}. Between these two field strengths is a mixed state. In this state it is energetically favorable for vortices, filaments of magnetic field, to enter the surface of the material and form a vortex lattice. These vortices are nonsuperconducting in the center. As they move through the material, they dissipate heat. The second critical field marks where all superconductivity is lost.

We are interested in the transition from superconducting states to mixed states for type II superconductors. We will simulate the physics near H_{sh} as this is the largest field attainable by a Type II superconductor before vortices form.

1.3 Literature review

We are not the first to contribute to calculations of H_{sh} and simulations of vortex dynamics. GL theory has plenty of literature because it is one of the simplest methods for identifying the different behaviors between type I and type II superconductors. Using finite element methods, finite difference methods, or pen and paper analysis there are many approaches to evaluating H_{sh} in GL theory [12–20]. Often slab geometry is assumed: half of space is filled with vacuum and the other half with a superconductor. Generalizations to study the impact of surface indentations on the flux entry field (H_{sh}) have also been performed [21–24].

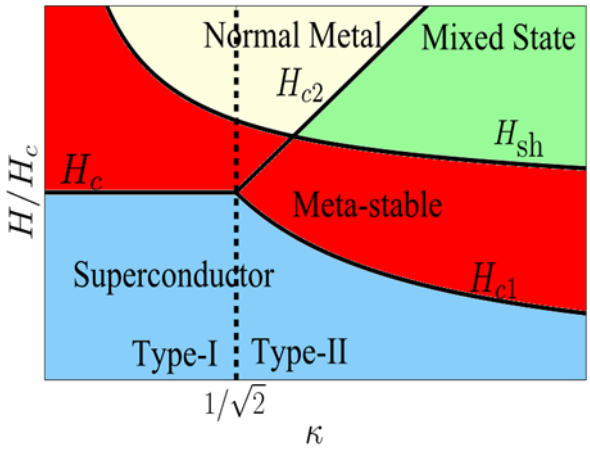

Figure 1.1 In Eilenberger and Ginzburg-Landau theory type I superconductors are characterized by $\kappa < \frac{1}{\sqrt{2}}$ while type II superconductors have $\kappa > \frac{1}{\sqrt{2}}$. Type I superconductors have a single critical magnetic field H_c while type II have two: H_{c1} and H_{c2}. Between those two critical magnetic fields is a mixed state of both superconducting and nonsuperconducting regions. Vortices, or filaments of magnetic field, reside in the nonsuperconducting regions. It is possible to be in a metastable state with magnetic fields greater than the critical field (known as the superheating field) as an energy barrier must be crossed for state transitions to occur. This diagram was produced within Ginzburg-Landau theory.

GL theory also does a good job of simulating vortex dynamics. The impact of L shaped domains, pinning sites, and surface indentations all have been done previously [25–35]. This continues to be an active area of research as many applications need material specific simulations of superconductors.

For Eilenberger theory there is much less literature on calculations of H_{sh}. The challenge of evaluating H_{sh} has been performed for large κ in both the clean [36] and dirty [37] limits. Generalizing to low and intermediate values of κ was attempted previously but the results were not completely converged for low temperatures [38]. One reason for the lack of literature is the sheer complexity in deriving the first and second variations of the Eilenberger free energy. Another is that accurate evaluations of H_{sh} can be very computationally expensive. See chapter 5 for more details.

1.4 Research Goals

The goal of this dissertation is to computationally study the behavior of superconductors in large magnetic fields. This has two parts, to simulate vortex dynamics in Ginzburg-Landau theory and to use automatic differentiation to abstract away the process of evaluating the first and second variations in Ginzburg-Landau and Eilenberger theory.

The first project relies very heavily on experimental observations performed by our collaborators at the Center for Bright Beams (CBB) as well as Sam Posen at Fermi National Lab. (See section 1.6 below.) They have observed a large variety of defects in Nb_3Sn superconducting resonant frequency (SRF) cavities including surface roughness, grain boundaries, and islands of depleted Sn. We want to know how this impacts H_{sh}. Another aspect to consider is that SRF cavities operate in AC magnetic fields. It is hypothesized that very high frequencies don't give vortices enough time to nucleate [39], leading to larger H_{sh}. We will simulate how AC fields impact H_{sh}. Finally, there are also open questions as to how the initial cooling influences how much residual flux remains in the

SRF cavity. We will show that temperature gradients can move vortices.

The second project stems from the fact that SRF cavities operate well below T_c. The value of H_{sh} may differ at lower temperatures where GL theory is inaccurate. One of the challenges of using Eilenberger theory is the complicated derivation of the first and second variations. To avoid these complications we propose a new method that evaluates these variations using automatic differentiation. We first show how this works for GL theory and then apply it to Eilenberger theory.

1.5 Organization

Chapter 2 is a paper that presents a new method for evaluating H_{sh} using saddle-node bifurcation theory and TDGL theory. We present the TDGL equations and explain how to introduce variations of T_c. We show that our new approach matches previous calculations of H_{sh} and k_c. We then show how surface roughness and internal variations of T_c quantitatively impact H_{sh}. We also give an example of how defects can lead to an increase in H_{sh} in 3 dimensions.

In chapter 3 we will review a paper that shows how our work fits in with other work performed at CBB. Our contribution comes from section IV where we run simulations of grain boundaries found in Nb_3Sn. These simulations are based on experimental images and calculations of T_c provided by our collaborators. We observe that vortices prefer to nucleate in grain boundaries. We show that for large applied fields the vortices fill up the grain boundaries until they get pushed into the grains themselves.

In chapter 4 we generalize our formulation to include parameters besides T_c. We simulate how islands of deficient Sn concentration reduce H_{sh} if they are near the surface. We show how AC fields can lead to vortex anti-vortex annihilation and demonstrate the dependence of H_{sh} on frequency. Finally we simulate a temperature wave during the cooling of an SRF cavity and show how they push vortices.

In chapter 5 we present a new method for evaluating H_{sh} using linear stability analysis and dual numbers. We first test this in GL theory and show we can match previous calculations of H_{sh} and k_c. We then extend this work to Eilenberger theory.

In chapter 6 we review the impact of this research, discuss limitations of this work, and propose future projects.

1.6 Broader Impacts of Research

The broader impacts of this research has not changed from my Masters to PhD. For this reason the following section comes mostly from my Masters thesis [9].

Imaging is an essential component of medicine, engineering, and science. The smaller the object the more difficult the acquisition of a clear image. Biologists studying proteins, engineers developing semiconductor technology, and physicists studying magnetic materials all need bright, coherent, and tunable x-ray beams for their research [40–42]. A common source for x-ray beams is synchrotrons. Unfortunately the current size and costs of these accelerators restricts their accessibility to researchers.

This work is part of a collaboration with the Center for Bright Beams (CBB), an NSF funded science and technology center, which seeks to increase the quality and decrease the cost of beams produced by accelerators. There are three main areas of improvement targeted by this center: beam creation, beam acceleration, and beam storage. Our efforts are directed at the field of beam acceleration. We explore how small defects lead to quenching of superconducting radio frequency cavities.

Beam acceleration is the process of speeding up charged particles to relativistic velocities. This is done in accelerators by using superconducting radio frequency (SRF) cavities [43]. Fig. 1.2 portrays what SRF cavities look like. This image shows a series of cavities all connected together.

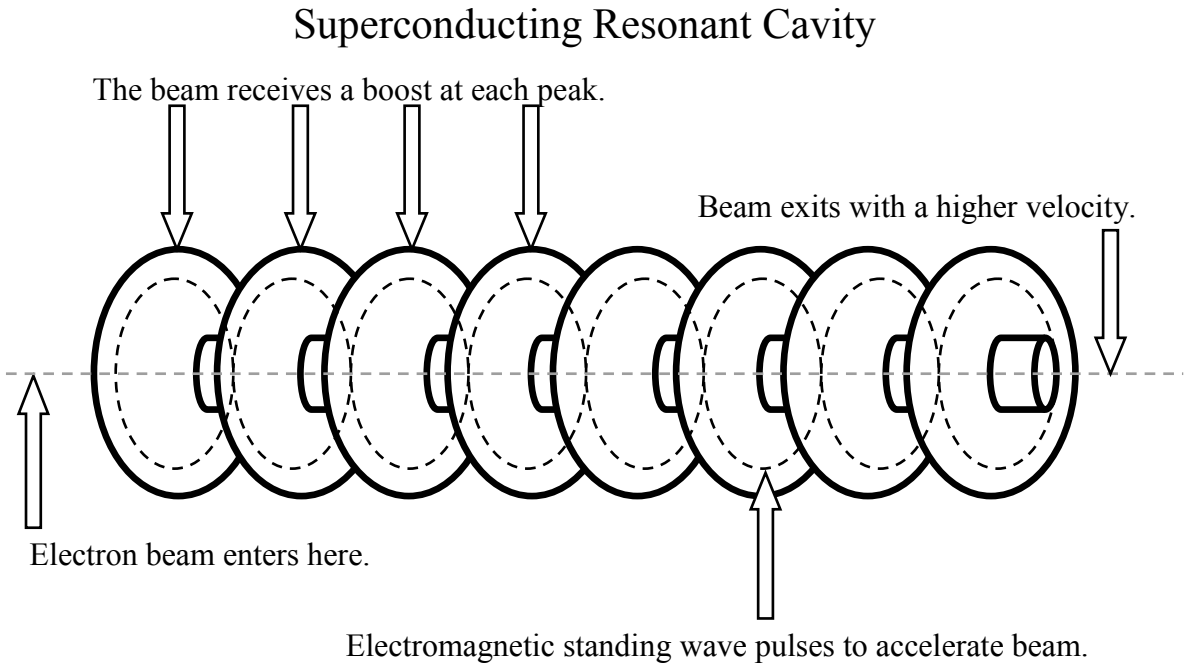

Figure 1.2 Diagrammatic sketch of a series of superconducting radio frequency cavities connected together. The inside of the cavities are plated with niobium, a superconductor. An AC current is tuned so that an entering bunch of electrons is accelerated at the center of each cavity.

The interiors of the cavities are plated with a superconductor, such as niobium. An AC current running through the cavities creates internal electromagnetic fields. The frequency of the AC current is tuned such that an entering cluster of electrons receives a boost of energy at the center of each cavity. The electrons are then used as an electron beam, or deflected to produce x-rays.

Much of the costs of operating SRF cavities comes from large cryogenic facilities that cool them to around 2 degrees kelvin, well below the boiling point of liquid helium. The largest electromagnetic fields and highest frequencies are achieved at this temperature, producing the brightest beams. Raising this operating temperature by improving SRF cavity stability would eliminate large portions of the cryogenic facilities, decreasing the size and cost of maintaining

accelerators.

Superconducting materials like Nb and Nb_3Sn face limitations from material inhomogeneities [44, 45]. Upon transitioning to a superconducting state magnetic fields can be trapped by imperfections. Applied AC currents move the trapped fields, thereby dissipating heat and lowering cavity quality. Some of these inhomogeneities include grain boundaries, surface roughness, and variations in Sn concentrations. Experts in cavity design need to know which material inhomogeneities are the most influential in reducing cavity stability.

Building and testing SRF cavities is expensive and the physics behind dynamic superconductivity is difficult to measure. By using numerical methods we can paint a picture of what should happen experimentally. We can simulate how material inhomogeneities influence accelerator performance and guide development efforts.

1.7 Note on Collaborative efforts

Much of the Ginzburg-Landau work is based on foundational code I developed during my masters thesis [9]. The capabilities of this code are well suited for simulating defects in Nb_3Sn cavities of interest to the Center for Bright beams. As our collaboration with the Center for Bright Beams grew it became apparent that there was more work than I could handle if I wanted to work on Eilenberger theory. Thankfully the complexity of Ginzburg-Landau theory and finite-element methods is abstracted away in the code. Instead of performing all these tasks by myself, Dr. Transtrum and I recruited undergraduate students to help out. They tweak the domain's geometry, applied field, included defects etc, run the simulation and then analyze the results. My task was to supervise their efforts by teaching them how to use the code, fixing any bugs beyond their reach, and helping interpret results. Some industrious students have added new functionality to the code. For this reason much of the Ginzburg-Landau results have joint ownership between many students and

myself. I will give credit where it is due.

Chapter 2

Time-Dependent Ginzburg-Landau simulations

Here we include a paper demonstrating our ability to model the impact of surface roughness and variations of T_c on H_{sh}. This contains the background necessary to understand how our code works. Of important note is our use of saddle-node bifurcation theory to evaluate H_{sh} and the critical mode that leads to vortex nucleation, ability to simulate interior material inhomogeneities, and simulation of defects in 3 dimensions. As of this writing, the manuscript has been accepted at PRB with some pending edits but a copy is available at arXiv, https://arxiv.org/abs/1911.02132. There are some minor differences between this document and what becomes published due to differences in editing suggestions. We have permission from PRB to include this paper.

Role of surface defects and material inhomogeneities for vortex nucleation in superconductors within time-dependent Ginzburg-Landau theory in 2 and 3 dimensions

Alden R. Pack,* Jared Carlson, Spencer Wadsworth, and Mark K. Transtrum†
Department of Physics and Astronomy, Brigham Young University, Provo, Utah 84602, USA
(Dated: April 4, 2020)

We use Time-Dependent Ginzburg-Landau theory to study the nucleation of vortices in type II superconductors in the presence of both geometric and material inhomogeneities. The superconducting Meissner state is meta-stable up to a critical magnetic field, known as the superheating field. For a uniform surface and homogenous material, the superheating transition is driven by a non-local critical mode in which an array of vortices simultaneously penetrate the surface. In contrast, we show that even a small amount of disorder localizes the critical mode and can have a significant reduction in the effective superheating field for a particular sample. Vortices can be nucleated by either surface roughness or local variations in material parameters, such as T_c. Our approach uses a finite element method to simulate a cylindrical geometry in 2 dimensions and a film geometry in 2 and 3 dimensions. We combine saddle node bifurcation analysis along with a fitting procedure to evaluate the superheating field and identify the unstable mode. We demonstrate agreement with previous results for homogenous geometries and surface roughness and extend the analysis to include variations in material properties. Finally, we show that in three dimensions, surface divots not aligned with the applied field can increase the super heating field. We discuss implications for fabrication and performance of superconducting resonant frequency cavities in particle accelerators.

I. INTRODUCTION

A hallmark feature of type-II superconductors is a phase transition from a purely superconducting (i.e., Meissner) state to a mixed state characterized by arrays of magnetic vortices. The mixed state can be understood as the compromise in the competition between magnetic pressure and the condensation of Cooper pairs. If the characteristic length scales for these phenomena are appropriately separated, a balance is struck in which filaments of magnetic field and small, non-superconducting cores are trapped by vortices of supercurrent. This configuration is thermodynamically stable between a lower and upper critical field (H_{c1} and H_{c2} respectively). Olsen et. al. beautifully captured this behavior using magneto-optical imaging [1]. For time-independent configurations, a stable array of vortices can be achieved, while for alternating magnetic fields, vortex motion leads to heat dissipation [2].

Ginzburg-Landau (GL) theory succinctly captures the relevant physics for describing the Meissner and vortex states, as well as the transition between the two. The theory is described by two characteristic length scales, the London penetration depth λ and the superconducting coherence length ξ. For materials in which the ratio $\kappa = \lambda/\xi$ (known as the GL parameter) is less than $1/\sqrt{2}$ the material is type I and will transition directly from the Meissner state to the nonsuperconducting state. However, for type II superconductors ($\kappa > 1/\sqrt{2}$) the material transitions first to a mixed, vortex state. The density of vortices increases with larger applied magnetic field until the system transitions to a nonsuperconducting state at H_{c2}.

Although vortices are thermodynamically stable for fields above H_{c1}, surface effects lead to an energy barrier to vortex nucleation [3]. The Meissner state can persist above H_{c1} up to a maximum magnetic field, known as the *superheating field* H_{sh} above which the energy barrier vanishes. For homogenous materials with smooth surfaces, this transition is driven by critical perturbations with a characteristic wavenumber k_c. For applications requiring a Meissner state (i.e., for which vortex nucleation is detrimental), H_{sh} is the fundamental limit to performance. As such, estimates of H_{sh} within Ginzburg-Landau theory have a long history [4–12]. This technique has since been extended to Eilenberger theory in both the clean [13] and dirty [14] limits. Often real systems have rough surfaces and interior defects that don't match this geometry. The role of surface roughness on H_{sh} in two dimensional geometries with surface defects has been studied extensively within Ginzburg-Landau theory [15–18]. There has also been considerable effort to simulate vortex nucleation and subsequent dynamics for more complicated domains within time-dependent Ginzburg-Landau (TDGL) theory [19–29].

Particle accelerators are an application of importance to a wide variety of fields [30–32] to which quantitative studies of the superheating field and vortex motion are particularly relevant. Superconducting Radio Frequency (SRF) cavities transfer energy to particle beams. Large AC currents running along the interior surface of the cavity induce electromagnetic fields that are timed to boost particle bunches as they pass through [33]. Traditionally cavities have been fabricated from Nb, but engineering advances have pushed these cavities to near their funda-

* a.pack@byu.edu
† mktranstrum@byu.edu

mental limits [34].

To more efficiently reach higher accelerating gradients, the accelerator community is exploring new materials for next-generation cavities [35]. Of particular interest is Nb_3Sn, which theoretically has $H_{sh} = 425[mT]$ and $T_c = 18[K]$ (compared to Niobium which has $H_{sh} = 219[mT]$ and $T_c = 9.2[K]$) [36]. In practice current Nb_3Sn cavities perform far-below theoretical limits [34, 37].

In addition to surface roughness, the alloyed nature of these materials often leads to variations in material parameters, such as Sn concentration, that can have a strong effect on the superconducting properties [38–43]. To guide future development and keep pace with experimental advancements, more sophisticated theoretical and computational tools are needed to identify the relevant physics for vortex nucleation and quantify their effect on H_{sh} in real materials. They need to be flexible enough to not only capture the impact of surface roughness, but also interior material inhomogeneities. These advances also offer an opportunity to validate theories of traditional superconductors in extreme conditions.

In this paper, we perform bifurcation analysis of the Meissner state using TDGL and a finite-element formulation. Our method quantitatively confirms previous estimates of H_{sh} derived in the symmetric, time-independent theory. We account for asymmetric geometries, such as surface divots, and variation in material parameters in two and three dimensions. We show that local reductions in the superconducting critical temperature is a potentially important nucleation mechanism in inhomogenous alloyed superconductors. Our method identifies the critical fluctuations that drive the vortex nucleation. Unlike the symmetric case in which arrays of vortices nucleate in tandem, a small amount of disorder acts as a nucleation site for individual vortices, indicating that near H_{sh}, the free energy surface has several shallow directions. We quantify this effect for both surface roughness and material inhomogeneity, a result that will guide the manufacture of precision samples to maximize performance. Finally, in three dimensions we show that the relative orientation of defects and the external field has a strong role in vortex nucleation. We demonstrate that defects aligned perpendicular to the applied field lead to an increase in H_{sh}.

The rest of this paper is organized as follows. Section II formulates the time-dependent Ginzburg-Landau (TDGL) equations to account for spatial variations in T_c and introduces the two- and three-dimensional geometries we consider. We use saddle-node bifurcation analysis to efficiently identify the critical modes that drive vortex nucleation and estimate H_{sh}. In section III we first confirm that our simulations for homogenous systems match previous work. Then we report on the effect of surface roughness and material inhomogeneity in two and three dimensions. Finally, in section IV, we discuss implications and limitations of our approach and potential future extensions.

II. METHODS

A. Problem Formulation

The time-dependent Ginzburg-Landau (TDGL) equations are a series of partial differential equations relating the superconducting order parameter to the electric potential and magnetic vector potential on mesoscopic scales. Although originally a phenomenological theory, the equations can be rigorously derived from the time-dependent Gorkov equations [44]. The TDGL equations in Gaussian units described by Kopnin in [45] are

$$-\Gamma\Big(\frac{\partial\psi}{\partial t} + \frac{2ie\phi}{\hbar}\psi\Big) = -|\alpha|\psi + \beta|\psi|^2\psi + \gamma\Big(-i\hbar\nabla - \frac{2e}{c}\mathbf{A}\Big)^2\psi \tag{1}$$

$$\begin{aligned}\mathbf{j} =& \frac{c}{4\pi}\nabla\times\nabla\times\mathbf{A}\\ =& \sigma_n\Big(-\frac{1}{c}\frac{\partial\mathbf{A}}{\partial t} - \nabla\phi\Big) + 2e\gamma\Big[\psi^*\Big(-i\hbar\nabla - \frac{2e}{c}\mathbf{A}\Big)\psi + \psi\Big(i\hbar\nabla - \frac{2e}{c}\mathbf{A}\Big)\psi^*\Big].\end{aligned} \tag{2}$$

These equations depend on the order parameter ψ, the magnetic vector potential $\mathbf{A}$, and the electric potential ϕ all of which can vary in space and time. The rest of the quantities are material parameters and fundamental constants: Γ is the rate of relaxation of the order parameter, e is the charge of an electron, $\hbar$ is Planck's constant divided by 2π, c is the speed of light, α is a material-specific constant proportional to $1 - T/T_c$ (T is temperature and T_c is the critical temperature), β is anther material parameter that is approximately constant with respect to T_c, γ is related to the effective mass of the cooper pairs, and σ_n is the conductivity of the normal electrons.

Typically, all physical constants can be absorbed into the units of fields. However, we relax this assumption in order to model spatial variations in T_c by allowing $\alpha(r) \propto 1 - T/T_c$ to vary in space over a range of values. This has been done previously to model pinning sites by setting $\alpha(r)$ to zero at fixed points in the domain [20, 26–28]. We define $\alpha(r) = \alpha_0 a(r)$ where α_0 is a reference value (to be subsumed by units), and $a(r)$ is a dimensionless number characterizing the spatial material variation. The quantities α_0 and $a(r)$ are defined with

respect to some reference point in the bulk material such that $a(r_0) = 1$ and $\alpha(r_0) = \alpha_0$. With this convention, α_0 can be absorbed into the units of the field. Values of a less than one correspond to a local T_c less than the reference value with $a < 0$ corresponding to T_c less than the operating temperature. The critical temperature of Nb_3Sn can depend strongly on the local concentration of Sn[43], so local reductions in T_c are an important potential mechanism for vortex nucleation.

With these modifications and assuming our boundary conditions are a fixed applied magnetic field on the surface with no current leaking into vacuum, we arrive at

$$\frac{\partial \psi}{\partial t} + i\phi\psi = -a\psi + |\psi|^2\psi + \left(\frac{-i}{\kappa_0}\nabla - \mathbf{A}\right)^2 \psi \tag{3}$$

$$\begin{aligned}\mathbf{j} =& \nabla \times \nabla \times \mathbf{A} \\ =& -\frac{1}{u_0}\left(\frac{\partial \mathbf{A}}{\partial t} + \frac{1}{\kappa_0}\nabla\phi\right) - \frac{i}{2\kappa_0}\left(\psi^*\nabla\psi - \psi\nabla\psi^*\right) - |\psi|^2\mathbf{A}\end{aligned} \tag{4}$$

$$\left(\frac{i}{\kappa_0}\nabla\psi + \mathbf{A}\psi\right)\cdot n = 0 \text{ on surface} \tag{5}$$

$$(\nabla \times \mathbf{A}) \times n = \mathbf{H} \times n \text{ on surface} \tag{6}$$

$$-\left(\nabla\phi + \frac{\partial \mathbf{A}}{\partial t}\right)\cdot n = 0 \text{ on surface,} \tag{7}$$

where we have introduced two new constants, u_0 and κ_0. The constant $u_0 = \tau_\psi/\tau_j$ is the ratio of the timescales for variations in the order parameter and the current. They are defined as,

$$\tau_\psi = \frac{\Gamma}{|\alpha_0|} \tag{8}$$

$$\tau_j = \frac{\beta\sigma_n}{8e^2\gamma|\alpha_0|} = \frac{\sigma_n}{8e^2\gamma\psi_0^2}. \tag{9}$$

The constant κ_0 is the Ginzburg-Landau parameter, the ratio of the penetration depth λ_0 and the coherence length ξ_0. All of these are defined with respect to the reference point r_0.

Eqs.(3)-(7) are a set of coupled partial differential equations in three dimensions. A common simplification is to assume a symmetry in the z-direction and only consider variations in the x-y plane. This assumption leads to a two-dimensional formulation which greatly reduces the computational overhead, but does limit the types of geometries that can be simulated. We perform both two-dimensional and three-dimensional simulations in this paper.

We numerically solve the TDGL equations using a finite element method (FEM) implemented in FEniCS [46]. Because the TDGL equations are diffusion-like, the time-step is implemented through an implicit formula. We use a backwards Euler formula, but higher order backwards difference formulas could also be applied. A more detailed description of previous methods is given by Gao et. al. [25].

One reason for the large variety of FEM formulations is the need to choose a gauge. Although physical quantities should remain the same in different gauges, the efficiency and accuracy of numerical methods with each gauge varies. We follow the formulations and conventions of Gao et. al. [25, 47]. Although the TDGL equations are nonlinear, by using solutions from the previous time steps, each time step can be formulated as a series of *linear* equations. For the two-dimensional case, the problem can be reduced to a series of Laplace and diffusion equations of coupled scalar fields which we implement as Lagrange elements. In three dimensions, the problem also reduces to a series of linear equations; however, the geometric nature of the magnetic field and vector potential in 3D require they be modeled as Ravier-Thomas and Nedelec elements of different orders. The complexity of the three-dimensional formulation incurs a substantial computational cost (both in time and memory).

In the two dimensional case, we define two geometries: an infinite cylinder and a thin film. In these geometries the magnetic field points in the $\hat{z}$ direction, i.e., perpendicular to the plane of simulation. Fig. 1 show these cross sections. For large radii and wide films these geometries approximate an infinite flat surface [4].

In the 3D case we consider a rectangular box cut out of a thin film as in Fig. 2. This is done by extending the domain of simulation along the z axis (the inner solid box). In this geometry we can orient the applied magnetic field in many directions along the surface of the film. The process of meshing these geometries is given in the appendix.

We take as initial conditions the case of a perfectly superconducting material in the absence of an applied field. We raise the applied magnetic field exponentially to values near H_{sh} in order to capture the dynamics of vortex nucleation. The time dependence of the magnetic field is $\mathbf{H_a}(t) = \mathbf{H}_{max}(1 - e^{-t/\tau})$. This allows us to quickly raise

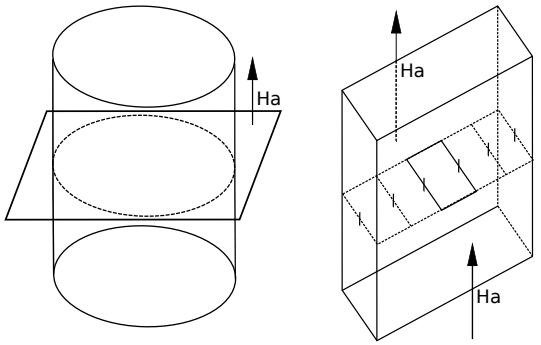

FIG. 1. **Two Dimensional Geometries.** We consider an infinite superconducting cylinder (left) and an infinite superconducting film (right). In both cases, the magnetic field is perpendicular to the plane of simulation and does not vary spatially. Boundary conditions require matching the applied magnetic field on the surface. For the film (right), we have periodic boundary conditions on the left and right sides.

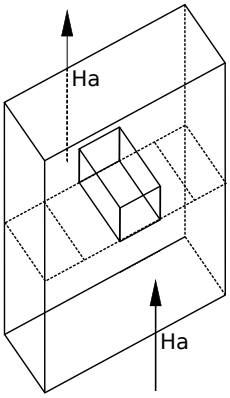

FIG. 2. **Three Dimensional Geometry.** We generalize the 2D film geometry by extending the x-y plane along the $\hat{z}$ direction. In this geometry we are free to rotate the direction of the magnetic field.

the field but slow down close to the asymptotic value **H** where vortex nucleation is sensitive to small fluctuations in ψ and **A**.

B. Inhomogeneities

This formulation allows for a wide variety of potential simulations. We go beyond the bulk geometry [4–12] by considering the influence of surface roughness and spatial variations of T_c (α).

We introduce surface roughness in two ways. First we model the surface of a wire (cylinder) as a Gaussian process (random sum of sinusoidal functions). Second, motivated by observed morphology of grain boundaries [48], we introduce a divot with a cutout of the form $Ae^{-|x|/\sigma}$.

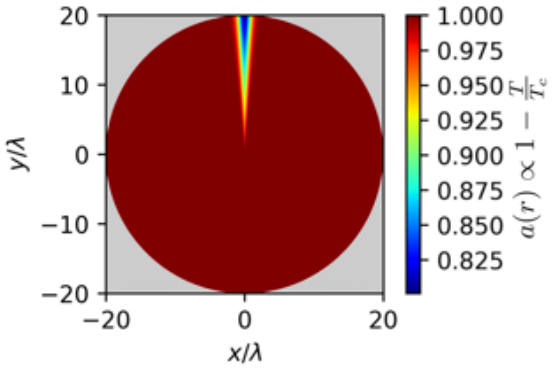

FIG. 3. **Spatial Dependence of a(r).** The dependence of the GL equations on the critical temperature comes from a coefficient a. We model the influence of Sn segregation as a local suppression of the superconducting critical temperature by allowing a to vary spatially. Here we show the value of a throughout the domain. $a < 1$ leads to a reduction of the superconducting order parameter.

Examples of these geometries are shown along with results in the next section and are described further in the appendix.

We model spatial variations of T_c within the cylindrical geometry as a Gaussian function $a(r,\theta) = 1 - Be^{\frac{-\theta^2}{2s^2}}(\frac{r}{R})^l$, see Figure 3. B is the lowest value of alpha, s sets the width of our defect, R is the cylinder radius, and l adjusts how quickly a drops off radially. This "line" of lowered T_c mimics the effect of Sn segregation in the grain boundaries of Nb_3Sn cavities [49].

C. Bifurcation Analysis and Mode Extraction

One of the contributions of this work is a method for calculating $H_{\rm sh}$ for arbitrary geometries and material properties. The superheating field occurs when the meta-stable Meissner state becomes unstable to a critical fluctuation. At $H_{\rm sh}$, the free energy landscape near the Meissner state transitions from a local minimum to a saddle point, and dynamics exhibit a saddle-node bifurcation. The free energy flattens (to lowest order) in the direction characterizing the critical fluctuation that nucleates magnetic vortices. Because the free energy landscape is flat near the bifurcation, simulation dynamics are slow for applied fields near $H_{\rm sh}$. Rather than solve the TDGL equations near the bifurcation, we use normal-form theory to quickly extract $H_{\rm sh}$ from simulations with applied fields below $H_{\rm sh}$.

The normal form of the saddle-node bifurcation is

$$\frac{dx}{dt} = -r + x^2 \tag{10}$$

where r is the bifurcation parameter [50] and, in our case, an implicit, unknown function of the applied field. x is some combination of finite element degrees of freedom that becomes the unstable, critical fluctuation.

Eq. (10) is stable for $r > 0$ and unstable for $r < 0$. Near the bifurcation, the system decays to equilibrium with a characteristic rate $\gamma = \frac{1}{2\sqrt{r}}$. We extract the critical mode, x by first finding the meta-stable Meissner state for applied fields below $H_{\rm sh}$. We then perturb the state with random white noise and extract the slowest mode and the decay rate γ using a fitting procedure [51]. Repeating this calculation for several different applied fields, we then extrapolate to find the applied field at which r becomes zero. We also apply an iterative technique to improve the numerical stability of this method. We repeatedly amplify the remaining noise and relax the system to cleanly separate the decaying mode and identify γ and r (see [52]). One of the benefits of this method is that it avoids running simulations where $r \approx 0$ and the timescale diverges.

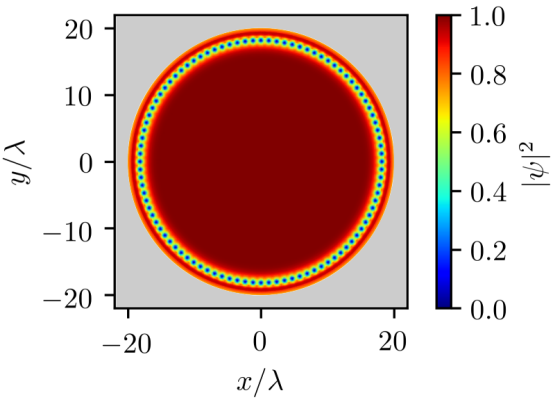

FIG. 4. **Vortex Nucleation.** The order parameter above $H_{\rm sh}$ after vortex nucleation for the cylinder geometry. We raise the magnetic field to a fixed value. If the magnetic field is larger than $H_{\rm sh}$ vortices nucleate. For the smooth cylinder there is no preferred location for vortex nucleation. They penetrate uniformly around the surface.

III. RESULTS

A. Agreement with Previous Work

We first demonstrate that our formulation correctly reproduces several known qualitative and quantitative results. We reproduce vortex nucleation and numerical estimates of $H_{\rm sh}$ using a cylindrical geometry without defects. Fig. 4 illustrates magnetic vortices shortly after nucleation for an applied magnetic field of $H_a = 0.8\sqrt{2}H_c$ and a cylinder of radius 20λ with $\kappa = 4$. Note that magnetic fields will always be measured in units of $\sqrt{2}H_c$ where H_c is the thermodynamic critical field. We will drop the $\sqrt{2}H_c$ from now on.

As described in section II C we extract the slowest decaying mode for fluctuations in the order parameter below but near H_{sh}. Fig. 5 shows this mode for a radius of 20λ. This pattern is roughly sinusoidal on the surface with a wavenumber k_c that we estimate from the number of times the pattern crosses zero. Fluctuations in this mode drive the transition from the Meissner state to the vortex state. Notice that the mode is non-local. The coordination of multiple penetrating magnetic vortices lowers the barrier to entry for any single vortex.

The procedure for calculating $H_{\rm sh}$ and k_c differ from those based on linear-stability analysis in the time-independent case [4]. Here, using bifurcation analysis, we extract the numerical value of the bifurcation parameter r using the observed decay rate of the critical mode. Repeating this for several different applied fields gives an empirical relationship between r and H_a, represented in Figure 6. The superheating field occurs at H_a such that $r = 0$. We estimate $H_{\rm sh}$ by fitting empirical estimates of $r(H_a)$ to a second-order polynomial and solving for $r = 0$. We also calculate k_c by counting the number of sign changes in the critical mode in Fig. 5. Table I summarizes our calculations of H_{sh} and k_c for varying κ and compares them to previous estimates from [4].

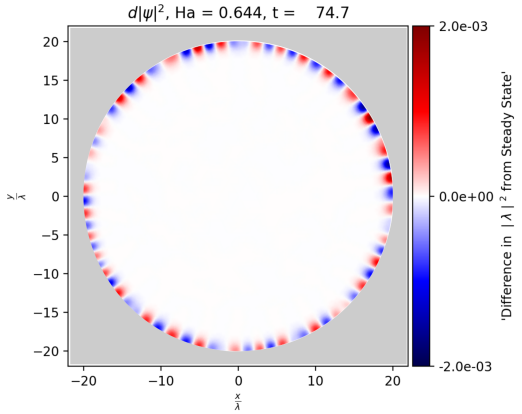

FIG. 5. **Critical Fluctuation.** We raise the magnetic field to a value below Hsh. The system is stable and small added perturbations decay away. We extract the slowest decaying mode by adding a small random perturbation. This mode is the critical fluctuation that drives the phase transition at $H_{\rm sh}$. Note that the alternating pattern of low and high values roughly match the pattern of vortices in Figure 4 and previous calculations of k_c in bulk geometries.

In addition to linear stability analysis, previous work has also used the time-dependent theory to estimate the entry field [15–29]. An advantage of using the time-dependent theory, is the ability to explore rough geometries. Typically, the field is raised until vortices nucleate, but efficiently and accurately determining the transition

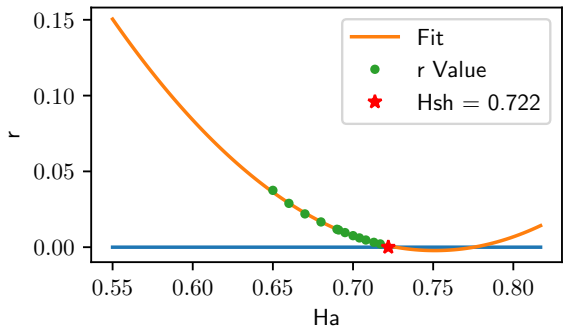

FIG. 6. **Extracting H_{sh}.** Varying the applied magnetic field changes the decay rate of the slowest decaying mode. We use that decay rate to find the bifurcation parameter r. This bifurcation parameter changes sign when the system loses stability. Extrapolating the bifurcation parameter r to zero gives H_{sh}.

	Cylinder H_{sh}	Slab H_{sh}	Absolute Relative Difference
$\kappa = 2$	0.803	0.7980	0.00615
$\kappa = 4$	0.721	0.7233	0.00320
$\kappa = 6$	0.683	0.6879	0.00711
$\kappa = 8$	0.660	0.6663	0.00944
	Cylinder k_c	Slab k_c	
$\kappa = 2$	0.975	1.1423	0.1465
$\kappa = 4$	2.125	2.31769	0.0831
$\kappa = 6$	3.125	3.27868	0.0468
$\kappa = 8$	3.925	4.15077	0.0544

TABLE I. **Numerical Results.** H_{sh} and k_c for different values of κ calculated using bifurcation analysis with a cylinder of radius 40. For comparison, we include estimates from [4] where H_{sh} and k_c were found using linear stability analysis with time-independent Ginzburg-Landau theory and a slab geometry. Due to the added complications of fitting the decay rate of the critical mode we are accurate to about three decimal places. We do not know the accuracy of the previous work as it was not provided. We evaluate the relative difference between these values. Note that as κ increases our values of H_{sh} decrease and our values of k_c increase giving the correct qualitative behavior.

point can be tedious as the relevant time scales diverge near H_{sh}. The bifurcation analysis we describe above extracts the same information without having to explicitly nucleate vortices. In the next section we demonstrate qualitative agreement to previous studies.

B. Random Surfaces

Vortex nucleation is a surface effect; surface roughness changes how vortices nucleate. Fig. 7 shows a simulation that captures vortex nucleation for a random surface. Note that $H_a = 0.7$ for this simulation and is less

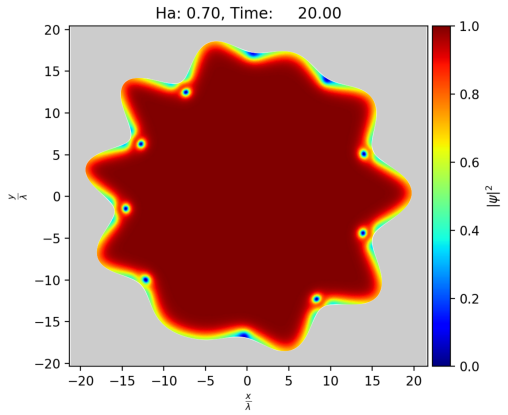

FIG. 7. **Vortex Nucleation for Rough Surfaces.** The norm squared of the order parameter just after vortex nucleation on a very rough cylinder. When we add surface roughness to the cylinder, vortices penetrate in the troughs of the surface.

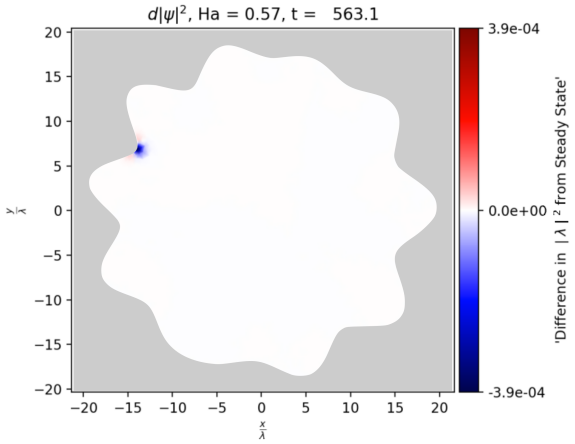

FIG. 8. **Critical Mode for the Rough Surface.** Adding surface roughness to the cylinder localizes the slowest decaying mode. Vortices nucleate at the same location where the slowest decaying mode has the highest magnitude.

than $H_{\rm sh}$ for the symmetric case. Also note that the critical fluctuation is no longer a periodic array. Instead the mode is large at concave regions of the surface, where the vortices first form (See Fig. 8). Using bifurcation analysis we calculate $H_{\rm sh}$= 0.566 for this geometry, a significant reduction in the value for a smooth surface ($H_{\rm sh}$= 0.72).

The roughness in Figure 7 is somewhat extreme, but illustrates the relevant physics in qualitative agreement with previous results. Although, less roughness leads to a smaller reduction in $H_{\rm sh}$, we find that even a very small roughness leads to a large, qualitative change in the critical mode. Indeed, even very small, individual divots act

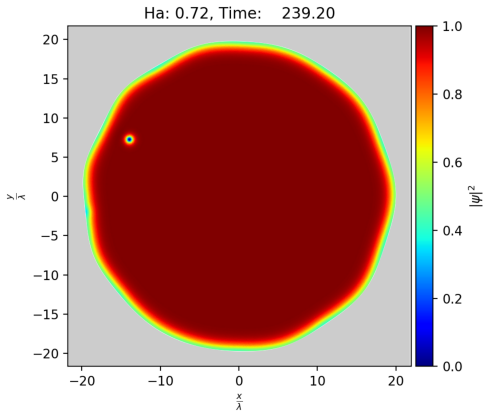

FIG. 9. **Vortex Nucleation for Small Roughness.** Even a little roughness qualitatively changes the vortex nucleation pattern. The applied field is tuned so that initially only one vortex nucleates.

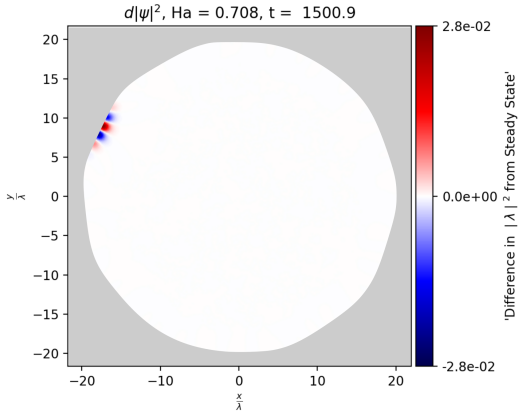

FIG. 10. **Critical Mode for Small Roughness.** Even a small amount of surface roughness localizes the critical mode. The critical mode is centered where the first vortex enters. Compare with Fig.9.

as nucleation points for vortices, as illustrated in Figures 9 and 10.

C. Single Divot

It has long been known that surface roughness is a relevant parameter for vortex nucleation within GL theory. To explore which geometric properties affect nucleation, we introduce a single exponential cut out on the surface of the cylinder. We vary the height and depth of this defect and calculate the corresponding reduction in $H_{\rm sh}$. Results are summarized in Fig. 11; divots that are narrow and deep lead to the largest reduction in $H_{\rm sh}$. A

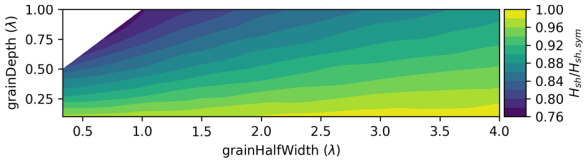

FIG. 11. **Role of Geometry in Vortex Nucleation.** The ratio of $H_{\rm sh}$ in the presence of a divot to the bulk value. A value of one means the divot has no impact. A value less than one means the divot is reducing H_{sh}. Divots that are thin and deep are the most detrimental.

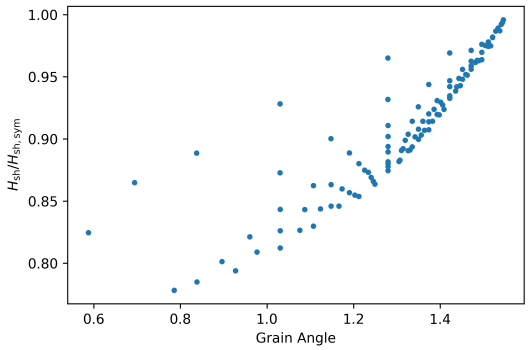

FIG. 12. **$H_{\rm sh}$ vs. Opening Angle.** Scatter plot of many calculated values of H_{sh} as the opening angle of the divot changes. There are multiple values of H_{sh} for individual opening angles. This means the amount that a divot reduces H_{sh} can not be explained just in terms of opening angles. The size of the divot relative to vortex size or the local curvature of the cylinder may also have an impact.

similar study assuming large κ and using London theory also found single divots to be detrimental [17].

An alternative parametrization of the divot geometry is in terms of the opening angle. A potential hypothesis is that the opening is the relevant parameter determining vortex nucleation; however, Figure 12 shows that this is not the case. We see that individual opening angles can have multiple values of H_{sh}. We hypothesize other factors such as the size of the divot relative to vortex size or to the local curvature of the cylinder impact H_{sh}.

D. Variations of T_c

In addition to surface roughness, material inhomogeneities also act as nucleation sites. We model variations in material properties by spatially varying $\alpha(r) \propto 1 - T/T_c$ as described in section II B. Fig. 13 shows that for $H_a > H_{sh}$ vortices first nucleate where T_c is lowest on the surface. Similar to surface roughness, even a small, local reduction in T_c leads to a localization in the critical

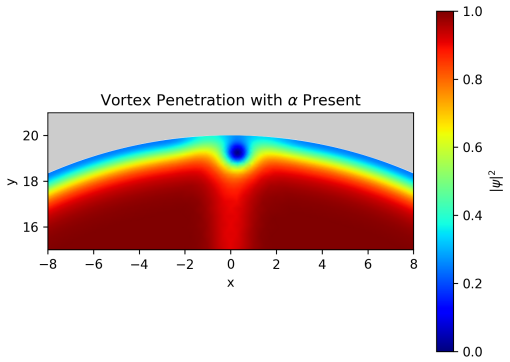

FIG. 13. **Nucleation Due to Material Inhomogeneity.** Plot of the norm squared of the order parameter above H_{sh} when $a(r)$ varies as shown in Fig. 3. Vortices nucleate in regions of low $a \propto 1 - T/T_c$ (i.e., lower T_c).

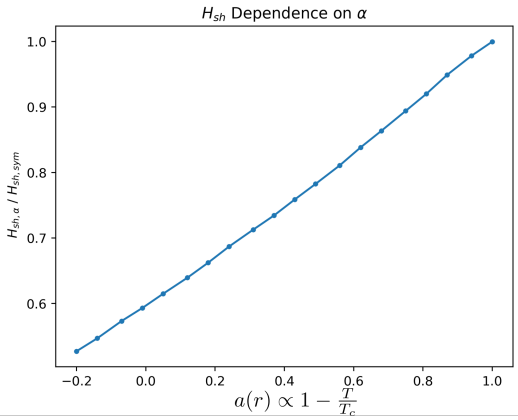

FIG. 14. **Reduction in H_{sh} vs. Material Parameter** The minimum value of $a(r)$ in the weakly-superconducting region determines the field at which vortices first nucleate. Here we plot the values of H_{sh} as blue dots with blue lines connecting the data points. As the minimum value of $a(r)$ drops, so does H_{sh}.

mode.

Variation in T_c can also lead to a significant drop in H_{sh} as seen in Fig. 14. As a point of comparison, for Nb_3Sn, the variation in Sn concentration can cause T_c to vary from about 18K at the optimal stoichiometry to as low at 6K in Sn depleted regions Sn seen in typical SRF cavities [38–43]. For an SRF cavity operating near 4K, this means that vortices could nucleate at an applied field around 0.6, an effect comparable to the extreme roughness of Figure 7. These results suggest that realistic variations in T_c could be an important mechanism for vortex nucleation.

E. Film Geometry

Up to this point, all our results have been reported for the two-dimensional cylindrical geometry. To control for the effects of curvature, we repeat our calculations using a film geometry. We apply the same magnetic fields to the top and bottom of the rectangular domain and enforce periodic boundary conditions on the left and right sides. Our results for the film geometry are nearly identical to those of the cylinder, indicating that the curvature effects are minimal.

F. 3D Film

A major limitation of the two-dimensional analysis is that the magnetic field must be parallel to the defects.

As mentioned in section II A, the 2D geometry is a cross section of a 3D domain that does not vary in the $\hat{z}$ direction. In this geometry it is not possible to simulate defects that break symmetries in the direction the magnetic field points, nor is it possible to have defects oriented differently from the applied field. To consider magnetic fields perpendicular to defects, we must move into fully three-dimensional geometries. Because three-dimensional simulations are more computationally expensive, we only consider volumes that accommodate a single vortex. Our geometry is a three-dimensional generalization of the 2D film. We fix the applied field on the faces parallel to the z-plane and apply periodic boundary conditions to the remaining sides. We use a mesh that is 2λ long in the x direction, 1.5λ in the y, and 5λ in the z direction.

Our results indicate that when defects are perpendicular to the applied field the superheating field is effectively raised. In Fig. 15, we observe a vortex nucleating on a smooth surface at an applied field of $H_a = 0.9$. The magnetic field direction is indicated by the black arrow. However, after introducing a defect perpendicular to the magnetic field, no vortex nucleates at $H_a = 0.9$. After raising the field to $H_a = 1.0$, the vortex fully enters the dented film. This demonstrates that the relative orientation of defects and the applied field also plays a crucial role in the nucleation mechanism and suggests that the most dangerous divots are those parallel to the applied magnetic field.

IV. DISCUSSION AND CONCLUSIONS

This work combines TDGL simulations with bifurcation analysis to study the transition of the metastable Meissner state to the mixed state of type II superconductors. We have implemented a finite-element method that accommodates rough geometries in two- and three-dimensions, as well as variations in material parameters. We have demonstrated accuracy by reproducing previous calculations of H_{sh} and k_c for smooth geometries. The

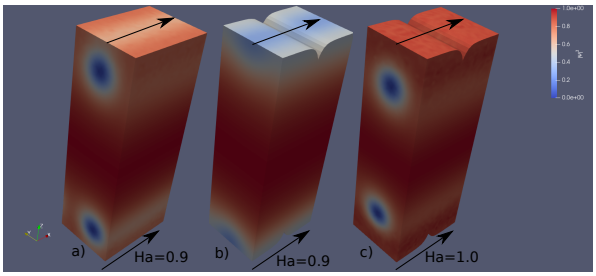

FIG. 15. **Vortex Nucleation in 3D.** Plotting the norm squared of the order parameter shows that a vortex has nucleated at $H_a = 0.9$ for the smooth surface but not the dented surface. At $H_a = 1.0$ we do see vortex nucleation perpendicular to the divot. This implies that divots perpendicular to the applied magnetic field could raise H_{sh}.

flexibility of finite element methods enable simulating geometries that are more complex, including both rough surfaces and material inhomogeneities. The bifurcation analysis allows us to efficiently extract both the superheating field as well as the accompanying critical mode without explicitly simulating vortex nucleation which occurs at diverging time scales.

We have shown that even very small surface roughness and material inhomogeneity can change the nucleation mechanism. In smooth geometries, arrays of vortices nucleate together. However, weak perturbations lead to a localization of the critical model and significant reduction in $H_{\rm sh}$. Future work will further apply these tools to geometries and material-specific parameters motivated by experimental observations.

As we are interested in defects about the size of a coherence length we focus on mesoscopic scales. We've chosen the penetration depth as our length scale in our simulations. This means that for increasing κ we must consider smaller coherence lengths. This further increases mesh density and makes simulations more computationally expensive. The value of κ determines how large of a domain we can simulate. For type-II materials, such as Nb_3Sn, simulations will be primarily limited to mesoscopic scales.

This work has been based on Ginzburg-Landau theory that has known limitations. Most importantly, GL theory is formally exact only when the system is close to its critical temperature; however, most SRF cavities operate well below T_c. Previous work applying Eilenberger theory to uniform surfaces and materials suggests that the Ginzburg-Landau predictions are surprisingly accurate (within a few percent) even at very low temperatures [13]. It is reasonable to expect that the *relative* effects of roughness and material inhomogeneity that we have quantified will hold even at low temperatures, and that inhomogeneities are likely to be bottlenecks to performance.

A critical aspect that we have ignored here is field enhancement. The field enhancement effect refers to a local increase in the applied field in response to surface roughness. Our simulations have not accounted for any field enhancement effects. This would require solving Maxwell's equations in the vacuum region outside the superconductor. This could be added in future work, but is beyond the scope of this study.

This analysis is a step toward sample-specific time-independent calculations of $H_{\rm sh}$ that includes not only surface defects, but spatially varying material parameters. We have shown that realistic variations in T_c can lower the barrier to vortex nucleation in ways similar to surface roughness and such effects are likely to be present in alloyed superconductors. We present these results as an exploration of GL theory and as a tool for quantifying detrimental defects in realistic superconducting samples. In the future we plan to extend these results to incorporate more material parameters and specific geometries into this framework and how these tools are bringing insight to the development of Nb_3Sn cavities.

We thank James Sethna, Danilo Liarte, Matthias Liepe, Tomas Arias, Sam Posen, Richard Hennig, Nathan Sitaraman, Michelle Kelley, Aiden Harbick, and Braedon Jones for helpful discussions. This work was supported by the US National Science Foundation under Award OIA-1549132, the Center for Bright Beams.

Appendix: Meshing

We simulate 3 geometries, the 2D cylinder, the 2D film, and the 3D film. In all of these geometries the mesh is refined to capture length scales smaller than the order parameter, otherwise the simulations do not accurately capture vortex dynamics.

For the smooth cylinder we want to keep the simulation as symmetric as possible to minimize the effect of numerical noise. Near $H_{\rm sh}$ small defects in the mesh can lead to vortex nucleation. For this reason we divide the domain into concentric circles. Starting with the inner circle we add points equally around the circumference. We then add points to the second largest circle such that if projected onto the inner circle they would be centered between the first set of points. We repeat this process adding extra points if the domain becomes too sparse. Finally, we are interested in dynamics near the surface so we push interior points radially outward. Fig.16 shows the end result of this process for a cylinder of radius 10λ.

Once we introduce an inhomogeneity the local defect dominates global behavior. It is no longer necessary to keep the mesh symmetric. We can let FEniCS automatically mesh the domain. We can define differing mesh densities for different regions as in Fig.17. In Fig.20 we can see the mesh close to the defect.

As a reference for future papers here is how we mesh the film. The domain is broken up into rectangles. We found that if we split the rectangles into an upper right triangle and a lower left triangle then nucleated vortices came in at an angle. To avoid this we divide each rectangle into 4 triangles as seen in the Fig. 18. When we

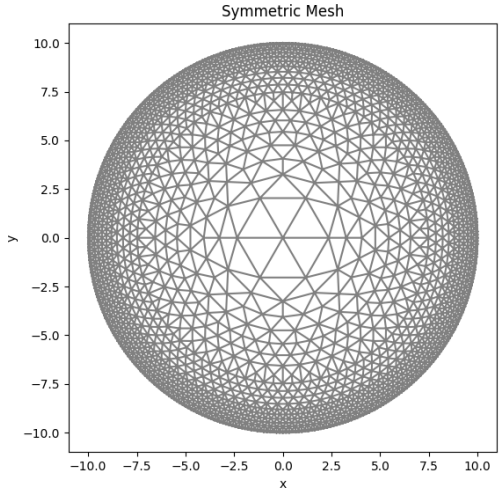

FIG. 16. We solve the time-dependent Ginzburg-Landau equations on a circular cutout of a cylinder. Forcing symmetry in the mesh ensures vortices penetrate uniformly. We refine the mesh near the surface as we are only interested in initial vortex nucleation. Length is measured in penetration depths

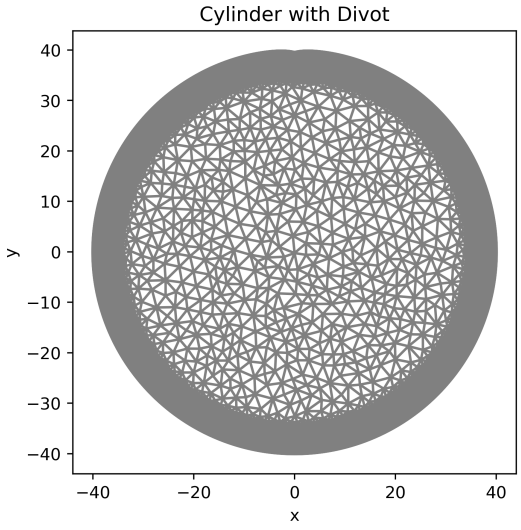

FIG. 17. We introduce a geometric defect to the cylinder based on experimentally observed grain boundaries.

introduce a divot the surface gets remeshed and this bias disappears as seen in Fig. 19

In 3D we only considered a domain that was big enough for 1 vortex to form. The surface has a symmetric grid of points. When we introduced a defect we centered the cusp on a line of vertex points. Interior points were not symmetric.

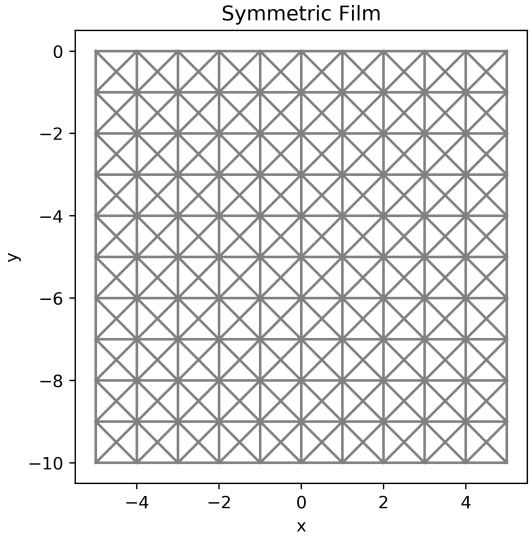

FIG. 18. Plot of the film geometry's mesh. To maintain symmetry each small square is broken up into 4 triangles. This prevents biases in vortex movement.

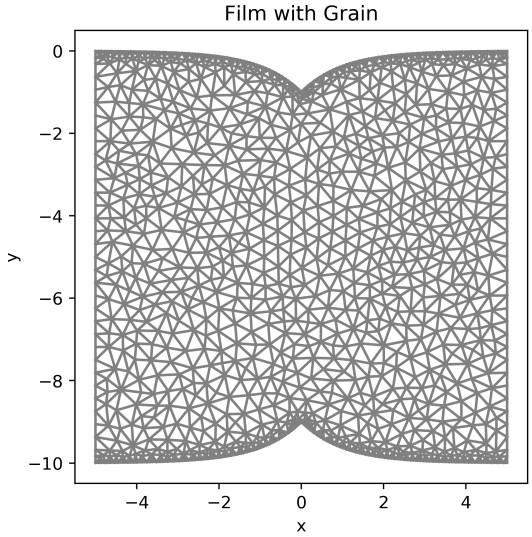

FIG. 19. Here we add a divot to the surface of the film mesh. Because this breaks symmetry we no longer worry about enforcing it in the entire domain. We refine the mesh near the surface.

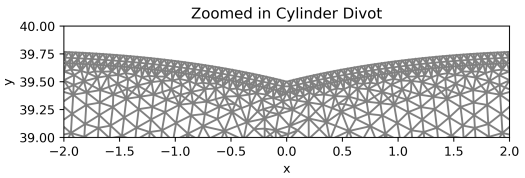

FIG. 20. We etch out an exponential-like function from the surface of our cylinder to match what is observed experimentally.

[1] Å. A. Olsen, H. Hauglin, T. Johansen, P. Goa, and D. Shantsev, Physica C: Superconductivity **408**, 537 (2004).
[2] D. B. Liarte, D. Hall, P. N. Koufalis, A. Miyazaki, A. Senanian, M. Liepe, and J. P. Sethna, Physical Review Applied **10**, 054057 (2018).
[3] C. Bean and J. Livingston, Physical Review Letters **12**, 14 (1964).
[4] M. K. Transtrum, G. Catelani, and J. P. Sethna, Physical Review B **83**, 094505 (2011).
[5] S. J. Chapman, SIAM Journal on Applied Mathematics **55**, 1233 (1995).
[6] A. J. Dolgert, S. J. Di Bartolo, and A. T. Dorsey, Physical Review B **53**, 5650 (1996).
[7] L. Kramer, Physical Review **170**, 475 (1968).
[8] P. De Gennes, Solid State Communications **3**, 127 (1965).
[9] V. Galaiko, Sov. Phys. JETP **23**, 475 (1966).
[10] L. Kramer, Zeitschrift für Physik A Hadrons and nuclei **259**, 333 (1973).
[11] H. Fink and A. Presson, Physical Review **182**, 498 (1969).
[12] P. V. Christiansen, Solid State Communications **7**, 727 (1969).
[13] G. Catelani and J. P. Sethna, Physical Review B **78**, 224509 (2008).
[14] F. P.-J. Lin and A. Gurevich, Physical Review B **85**, 054513 (2012).
[15] P. Soininen and N. Kopnin, Physical Review B **49**, 12087 (1994).
[16] D. Y. Vodolazov, Physical Review B **62**, 8691 (2000).
[17] L. Burlachkov, M. Konczykowski, Y. Yeshurun, and F. Holtzberg, Journal of applied physics **70**, 5759 (1991).
[18] A. Y. Aladyshkin, A. Mel'Nikov, I. Shereshevsky, and I. Tokman, Physica C: Superconductivity **361**, 67 (2001).
[19] M. Machida and H. Kaburaki, Physical review letters **71**, 3206 (1993).
[20] A. E. Koshelev, I. A. Sadovskyy, C. L. Phillips, and A. Glatz, Physical Review B **93**, 060508 (2016).
[21] Q. Du, Computers & Mathematics with Applications **27**, 119 (1994).
[22] B. Oripov and S. Anlage, arXiv preprint arXiv:1909.02714 (2019).
[23] A. T. Dorsey, Physical Review B **46**, 8376 (1992).
[24] B. Li and Z. Zhang, Journal of Computational Physics **303**, 238 (2015).
[25] H. Gao and W. Sun, Journal of Computational Physics **294**, 329 (2015).
[26] I. A. Sadovskyy, A. E. Koshelev, C. L. Phillips, D. A. Karpeyev, and A. Glatz, Journal of Computational Physics **294**, 639 (2015).
[27] M. P. Sørensen, N. F. Pedersen, and M. Ögren, Physica C: Superconductivity and its applications **533**, 40 (2017).
[28] J. Deang, Q. Du, M. Gunzburger, and J. Peterson, Philosophical Transactions of the Royal Society of London. Series A: Mathematical, Physical and Engineering Sciences **355**, 1957 (1997).
[29] A. Benfenati, A. Maiani, F. N. Rybakov, and E. Babaev, arXiv preprint arXiv:1911.09513 (2019).
[30] R. W. Hamm and M. E. Hamm, *Industrial accelerators and their applications* (World Scientific, 2012).
[31] U. Amaldi, Nuclear Physics A **654**, C375 (1999).
[32] E. Malumud, TheDivision of Physics of Beams of the American Physical Society, (2010).
[33] H. Padamsee, J. Knobloch, T. Hays, *et al.*, *RF superconductivity for accelerators*, Vol. 2011 (Wiley Online Library, 2008).
[34] S. Posen, N. Valles, and M. Liepe, Physical review letters **115**, 047001 (2015).
[35] S. Posen, M. Liepe, *et al.*, in *Proceedings of Particle Accelerator Conference, PAC* (2013).
[36] S. Posen, *Understanding and overcoming limitation mechanisms in Nb3Sn superconducting RF cavities*, Ph.D. thesis, Cornell University (2015).
[37] S. Posen and M. Liepe, Physical Review Special Topics-Accelerators and Beams **17**, 112001 (2014).
[38] H. Devantay, J. Jorda, M. Decroux, J. Muller, and R. Flükiger, Journal of Materials Science **16**, 2145 (1981).
[39] R. Flükiger, in *Superconductivity in d- and f-Band Metals* (1982).
[40] A. Godeke, Superconductor Science and Technology **19** (2006).
[41] C. Becker, S. Posen, N. Groll, R. Cook, C. M. Schlepütz, D. L. Hall, M. Liepe, M. Pellin, J. Zasadzinski, and T. Proslier, Applied Physics Letters **106**, 082602 (2015).
[42] J. Lee, S. Posen, Z. Mao, Y. Trenikhina, K. He, D. L. Hall, M. Liepe, and D. N. Seidman, Superconductor Science and Technology **32**, 024001 (2018).
[43] N. S. Sitaraman, J. Carlson, A. R. Pack, R. D. Porter, M. U. Liepe, M. K. Transtrum, and T. A. Arias, arXiv preprint arXiv:1912.07576 (2019).
[44] L. GoR'Kov and G. Eliashberg, in *30 Years Of The Landau InstituteSelected Papers* (World Scientific, 1996) pp. 16–22.
[45] N. Kopnin, *Theory of nonequilibrium superconductivity*, Vol. 110 (Oxford University Press, 2001).

[46] M. S. Alnæs, J. Blechta, J. Hake, A. Johansson, B. Kehlet, A. Logg, C. Richardson, J. Ring, M. E. Rognes, and G. N. Wells, Archive of Numerical Software **3**, 9 (2015).
[47] H. Gao, Communications in Computational Physics **22**, 182 (2017).
[48] S. Posen and D. L. Hall, Superconductor Science and Technology **30**, 033004 (2017).
[49] M. Jewell, A. Godeke, P. Lee, and D. Larbalestier, in *AIP Conference Proceedings*, Vol. 711 (AIP, 2004) pp. 474–484.
[50] S. H. Strogatz, *Nonlinear dynamics and chaos: with applications to physics, biology, chemistry, and engineering* (Westview press, 2014).
[51] A. R. Pack, *Computational Exploration of Vortex Nucleation In Type II Superconductors Using a Finite Element Method in Ginzburg-Landau Theory*, Master's thesis, Brigham Young University. Department of Physics and Astronomy (2017).
[52] J. Carlson, "Simulations of magnetic vortex nucleation at grain boundaries in rf superconducting cavities," (2019).

Chapter 3

Grain Boundaries in Nb_3Sn

Having developed software capable of simulating vortex nucleation with surface roughness and material inhomogeneities our next step is to simulate defects found experimentally. The following paper shows how this project fits into a larger community of researchers studying improvements to SRF cavities in particle accelerators. Our contribution comes from section IV. We show how vortices prefer to nucleate along grain boundaries where experimental measurements show an increase in Sn leading to a decrease in T_c. We find that as the magnetic field increases vortices first form along the grain boundary. At large magnetic fields the number of vortices increases until they get pushed out of the grain boundary. As of this writing, the manuscript is under review at PRB and available at arXiv, https://arxiv.org/abs/2003.03362. We will have permission from PRB to include this paper.

Analysis of Magnetic Vortex Dissipation in Sn-Segregated Boundaries in Nb_3Sn SRF Cavities

Jared Carlson,* Alden Pack, and Mark K. Transtrum†
Department of Physics and Astronomy, Brigham Young University, Provo, Utah 84602, USA

Jaeyel Lee* and David N. Seidman
Department of Materials Science and Engineering, Northwestern University, Evanston, Illinois 60201, USA

Danilo B. Liarte,* Nathan Sitaraman,* Alen Senanian, James P. Sethna, and Tomas Arias
Cornell University, Ithaca, New York 14853, USA

Sam Posen
Fermi National Accelerator laboratory, Batavia, Illinois 60510, USA
(Dated: April 2, 2020)

We study mechanisms of vortex nucleation in Nb_3Sn SRF cavities using a combination of experimental, theoretical, and computational methods. Scanning transmission electron microscopy (STEM) image and energy dispersive spectroscopy (EDS) of some Nb_3Sn cavities show Sn segregation at grain boundaries in Nb_3Sn with Sn concentration as high as $\sim$35 at.% and widths $\sim$3 nm in chemical composition. Using ab initio calculations, we estimate the effect excess tin has on the local superconducting properties of the material. We model Sn segregation as a lowering of the local critical temperature. We then use time-dependent Ginzburg-Landau theory to understand the role of segregation on magnetic vortex nucleation. Our simulations indicate that the grain boundaries act as both nucleation sites for vortex penetration and pinning sites for vortices after nucleation. Depending on the magnitude of the applied field, vortices may remain pinned in the grain boundary or penetrate the grain itself. We estimate the superconducting losses due to vortices filling grain boundaries and compare with observed performance degradation with higher magnetic fields. We estimate that the quality factor may decrease by an order of magnitude (10^{10} to 10^9) at typical operating fields if 0.03% of the grain boundaries actively nucleate vortices. We additionally estimate the volume that would need to be filled with vortices to match experimental observations of cavity heating.

I. INTRODUCTION

Superconducting Radio-Frequency (SRF) cavities are used in accelerators to transfer energy to beams of charged particles. Induced magnetic fields are a fundamental limit to performance due to stability of the superconducting Meissner effect, i.e., perfect diagmagnetism. For type-II materials, complete flux expulsion is thermodynamically stable up to a lower-critical field, H_{c1}, and a mixed state characterized by superconducting vortices is stable for fields up to an upper-critical field, H_{c2}. Thus, by limiting the fields on the walls of the SRF cavities, the superconductor can be kept in the flux-free Meissner state, so that surface dissipation is extremely small and quality factors $\sim 10^{10}$ can be achieved. For magnetic fields parallel to the cavity surface, the superconducting Meissner state can be maintained above the stability limit in a metastable state up to a limit (for an ideal surface) of the so-called superheating field H_{sh}[1]. H_{sh} has been studied extensively by the condensed matter community, primarily in the context of Ginzburg-Landau theory at ideal interfaces[2–5]. Because high-power SRF cavities routinely operate in the metastable regime[6], there has been renewed interested by the condensed matter community in the behavior of superconductors in large magnetic fields. Calculations extend results to the semiclassical theory of Eilenberger theory in both the clean[7] and dirty[8] limits and Time-Dependent Ginzburg Landau (TDGL) simulations that account for material[9] and spatial inhomogeneities[10–13]. In this paper, we explore the role of grain boundaries (GBs) in SRF cavity performance motivated by experimental observations of inhomogeneities in real-world SRF cavities. This study brings together the expertise of many areas of condensed matter and accelerator physics to explore fundamental physics of superconductors in extreme conditions and connect those results to real systems.

Recently there has been significant progress towards the employment of Nb_3Sn in SRF cavities as a higher performance alternative to the industry standard Nb for next generation particle accelerator applications [14, 15]. Nb_3Sn cavities are prepared with Nb_3Sn films $\sim$2 μm (nearly 20 penetration depths) thick coated on the surface of Nb cavities using the Sn vapor-diffusion process. Nb_3Sn is an intermetallic alloy with A15 crystal structure; it is a promising material for next-generation SRF

* These authors contributed equally
† mktranstrum@byu.edu

cavities in large part because of its large (predicted) superheating field (∼400 mT). It also has a higher critical temperature (Tc ∼18K), making possible a higher quality factor (Q_0, another critical metric of cavity performance) at a given temperature compared to Nb (Tc ∼9K).

In practice, however, real world Nb_3Sn cavities quench well below the theoretically predicted value. The maximum accelerating gradient that has been achieved within these cavities is about 24 MV/m, which corresponds to the surface magnetic field of ∼98 mT. These cavities exhibit a high Q_0 of $\sim 10^{10}$ at 4.2 K [14, 16]; however, in some cavities, Q_0 begins to degrade significantly before the limiting quench field is reached, a phenomenon described as "Q-slope"[17].

Understanding the mechanism underlying the Q-slope phenomenon is an important question for cavity development. Several mechanisms have been proposed in terms of imperfections in the Nb_3Sn coatings [6, 18, 19] such as thin grains [20, 21] and Sn-deficient regions [22]. Another potential mechanism that may have detrimental effects on the performance of Nb_3Sn cavities is Sn segregation at grain boundaries [23]. In some Nb_3Sn coatings, tin concentrations as high as ∼35 at.% have been observed in grain boundaries with the segregated zone extending by as much as ∼3 nm, comparable to the coherence length of Nb_3Sn (∼3 nm). Because of the inferior superconducting properties, magnetic flux may penetrate the segregated region, degrade Q_0, and lead to premature quench.

In support of this hypothesis, witness samples coated with high-performance (quench at ∼24 MV/m with $Q\sim10^{10}$ at 4.4 K) Nb_3Sn cavities at Fermilab did not show Sn segregation at the grain boundaries in energy dispersive X-ray spectroscopy (EDS) and in scanning transmission electron microscopy (STEM). Similarly, a direct cutout from a high-performance Nb_3Sn cavity fabricated at Cornell did not show Sn segregation at grain boundaries within the detection limit of STEM-EDS. In contrast, Nb_3Sn cavities, which show Sn segregation at grain boundaries in witness samples coated together with the cavities, displayed negative Q-slope for accelerating fields in the 5-15 MV/m range, see Fermilab cavity 1 and 2, Fig. 1. These experimental results, summarized in Fig. 1, suggest a potential link between Sn segregation at grain boundaries and cavity performance [23].

Experimentally, it is difficult to isolate the effects of Sn segregation at grain boundaries from other imperfections, such as Sn-deficient regions and surface roughness. To overcome these challenges, we use numerical tools to theoretically understand the role of segregation in grain boundaries for SRF cavity performance. We use density functional theory to estimate the effective T_c of the material within the segregation zone. Next, we use time-dependent Ginzburg-Landau simulations with spatial varying material properties motivated by the ab initio DFT calculations. Time-dependent Ginzburg-Landau theory allows us to conduct numerical experiments on a mesoscale that probe the role of grain boundaries and segregated zones for vortex nucleation, pinning, and

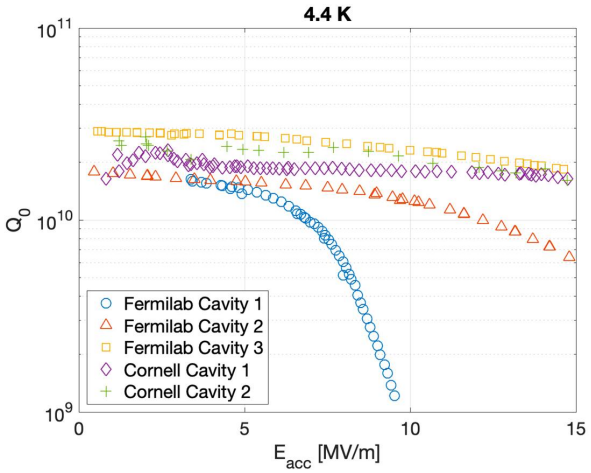

FIG. 1. Q vs E curve of various Nb_3Sn SRF cavities coated at Fermilab and Cornell. The GBs of a witness sample (Fermilab Cavity 3) and direct cutout (Cornell Cavity 2) of a high-performance cavity are characterized in STEM-EDS and showed no Sn segregation at GBs. On the other hand, witness samples of Fermilab Cavity 1 and 2, which show Q-slope starting at 8 MV/m, were found to have Sn segregation at GBs (reprint from [23]).

quenching. Finally, motivated by our TDGL simulations, we estimate power dissipated by vortex nucleation within segregated grain boundaries during an RF cycle and make quantitative comparisons to actual SRF cavities.

This paper is organized as follows: First, we present experimental images of defects in Nb_3Sn cavities in section II. We then report on first principles DFT calculations of superconducting properties for segregation zones in section III and time-dependent Ginzburg-Landau simulations of flux penetration in section IV. We estimate the effect on cavity performance in section V. Our numerical experiments isolate the effects of Sn-segregated grain boundaries from potentially confounding mechanisms. Our results indicate that the effects of Sn-segregated grain boundaries alone are consistent with observed behaviors. Specifically, grain boundaries may nucleate and then trap a limited number of vortices, leading to degredation in the cavity's quality factor. We conclude by discussing the implications of these results for cavity development and further theoretical studies in section VI.

II. EXPERIMENTAL IMAGES OF NB_3SN DEFECTS

The high angle annular dark field (HAADF)-STEM image in Figure 2 displays a Nb_3Sn coating on Nb prepared by the Sn vapor diffusion process using coating parameters from the early stage of the development of Nb_3Sn films at Fermilab [14]. EDS mapping is performed

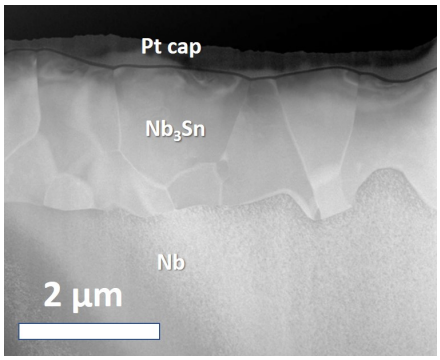

FIG. 2. HAADF-STEM image of a typical ∼2 μm thick Nb_3Sn coating on Nb prepared by Sn vapor-diffusion.

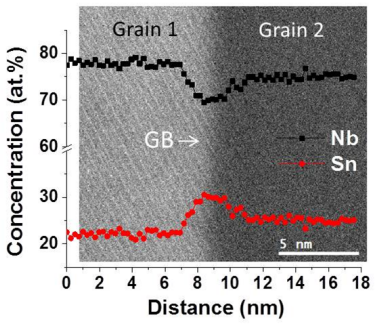

FIG. 3. The HAADF-STEM image and corresponding Nb and Sn concentration profiles across the GB between Grain 1 and Grain 2. Sn is segregated at the GB up to ∼33 at.% Sn and the width of the Sn segregated region is ∼3 nm.

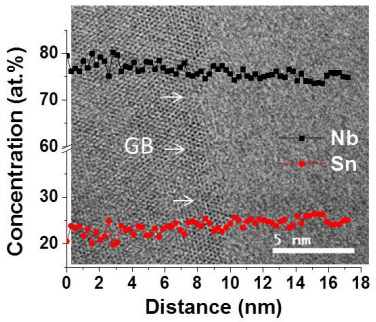

FIG. 4. BF-STEM and corresponding Nb and Sn concentration profiles across a GB from a witness sample of high-performance Nb_3Sn SRF cavity prepared at Fermilab.

across a GB in a Nb_3Sn coating prepared by the same coating parameters and it reveals that Sn is segregated at the GB, Figure 3. A maximum concentration of Sn at the GB is ∼33 at.% and a width of the Sn segregated region is ∼3 nm. The Gibbsian interfacial excess of Sn is ∼16 atom/nm^2. Previous studies on analyses of structures of Sn-segregated GBs in Nb_3Sn employing HR-STEM and first-principle calculations indicated that most of the segregated Sn exist as Sn-antisite defects near the GBs rather than forming Sn-rich phases such as Nb_6Sn_5 or other non-equilibrium phases [23, 24].

Another GB from a witness sample of a high-performance cavity prepared at Fermilab is characterized by HR-STEM EDS, Fig. 4. It is noted that there is no Sn segregation at the GB within the detection limit of EDS (∼1 at.%). This may indicate that there could be a possible correlation between the Sn segregation at GBs and cavity performance. It has been reported that Sn segregation is caused by Sn diffusion via GBs due to high Sn supply and it can be controlled using carefully selected coating parameters [23].

Also, the dips are formed on the surface at GBs and HAADF-STEM image in Fig. 5 displays the geometry of a GB on the top surface. It has ∼80 nm of depth and ∼420 nm of width. The composition and surface roughness change at the GBs, possibly providing pathways for flux to penetrate through the imperfections. These experimental observations are the motivation for our ab initio and Ginzburg-Landau modeling to investigate the effect of the imperfections on the vortex penetration.

III. THE EFFECT OF TIN-RICH STOICHIOMETRY ON T_c

The presence of tin-rich stoichiometry near grain boundaries has been established experimentally, but because these regions are so small, it is difficult to directly probe their superconducting properties. We therefore consider *ab initio* T_c values calculated using Eliashberg theory [25] and Density Functional Theory (DFT) [26]. Ref. [27] presents such results obtained using a Wannier-based k-point sampling approach[28]. For the experimentally measured stoichiometry range of the A15 phase, the predicted T_c values are similar to or modestly higher than experimental values, as described in Table 1. For experimentally inaccessible tin-rich stoichiometry, T_c values fall

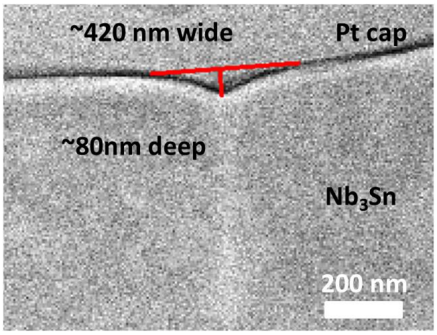

FIG. 5. HAADF-STEM image of the cross-section of the top surface of a Nb_3Sn GB.

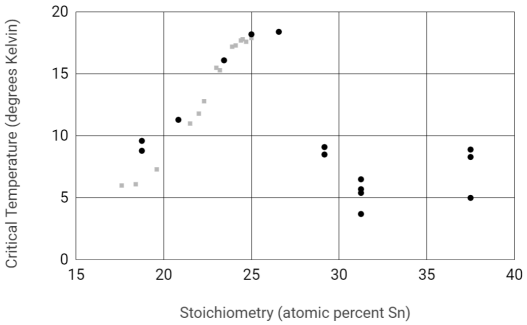

FIG. 6. Experimental T_c [29] (grey squares) and calculated T_c (black circles) for A15 Nb-Sn of different stoichiometries. For some stoichiometries, multiple possible defect configurations were considered. The calculated T_c reaches a minimum of about 5 Kelvin in the tin-rich regime.

to a minimum of about 5K at 31.25% Sn stoichiometry (Fig. 6). This is well within the range that has been observed around grain boundaries.

TABLE I. Calculated vs. Measured T_c

Composition	**Experimental T_c (K)**	**Calculated T_c (K)**
18.75% Sn	6	9.2†
20.83% Sn	9.5	11.3
23.44% Sn	16	16.1
25.00% Sn	18	18.2
31.25% Sn	n/a	5.3†

† Averaged over multiple configurations.

IV. TIME-DEPENDENT GINZBURG-LANDAU SIMULATIONS OF VORTEX NUCLEATION

A. Introduction to Methods

Time-dependent Ginzburg-Landau (TDGL) theory is sophisticated enough to capture vortex dynamics without becoming too algebraically complicated and computationally expensive. We solve the TDGL equations using a finite element method implemented in FEniCS[30, 31]. We follow the finite element formulation described by Gao et. al[9, 32]. Note that in this formulation length is measured in units of the penetration depth λ.

This formulation reduces the full three-dimensional problem into a two-dimensional problem by assuming symmetry along the z-axis. The magnetic field points along the z-axis, fixing variations in the order parameter and magnetic vector potential to the x-y plane.

We consider the film geometry seen in Figure 7. We take a rectangular cross-section lying in the x-y plane. We enforce periodic boundary conditions on the left and right side. On the top and bottom, we enforce Dirichlet boundary conditions for the magnetic field and Neumann boundary conditions for the order parameter.

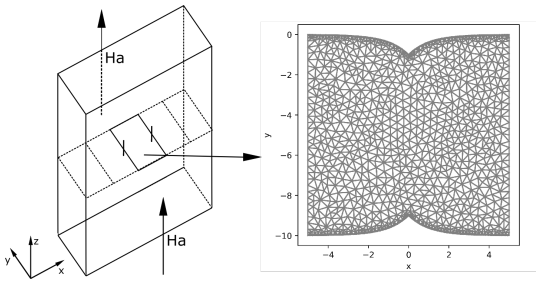

FIG. 7. The black square interior to the film geometry marks our domain of simulation. It lies perpendicular to the applied magnetic field H_a. We assume there are no variations in the direction of H_a so that we can simulate a 2D domain.

We model geometric defects by removing an exponential cut out from the top and bottom of the film. The region removed is given by $de^{-\frac{|x|}{w}}$ where d is the depth of the cut out and w determines the width.The depth and width are chosen to match experimentally observed geometries.

To capture Sn segregation we allow Tc to vary over the domain. This is done by varying the $\alpha \propto T/T_c - 1$ parameter as described in [9]. To mimic the distribution of material inhomogeneities shown in Figure 3, we introduce $\alpha' = (T/T_c - 1)/\alpha_{ref} \leq 1$ in the GB region $|x| \leq \xi/2$ and $\alpha_{ref} = -1$ elsewhere. The projection of this onto the mesh is shown in Figure 8.

The Ginzburg-Landau parameter for Nb_3Sn is $\kappa = \lambda/\xi \sim 26$, which is challenging to simulate because of the extreme separation in length scales that require a very refined mesh. However, the relevant physics for vortex nucleation are variations in material parameters on length scales comparable to the superconducting coherence length, ξ. Therefore, we have simulated a moderate type-II material ($\kappa = 4$) but scaled the width of the segregated region (i.e., depleted T_c) so that its dimensions relative to ξ are the same as that observed in Figure 3. Although these assumptions may affect quantitative details, we expect the qualitative results are the same for more extreme type-II materials.

B. Vortex Nucleation in Grain Boundaries

To simulate the nucleation of vortices into a grain boundary, we set the value of the magnetic field at the top and bottom boundary such that it is low enough that an array of vortices do not penetrate directly into the bulk, but large enough for vortices to enter into the grain boundary[9]. As we evolve in time (assuming a constant applied field), two different behaviors are observed depending on the magnitude of the applied field. In the first scenario, vortices enter into the grain boundary at the geometric divot. With increasing field, the spacing between vortices decreases until it reaches critical levels.

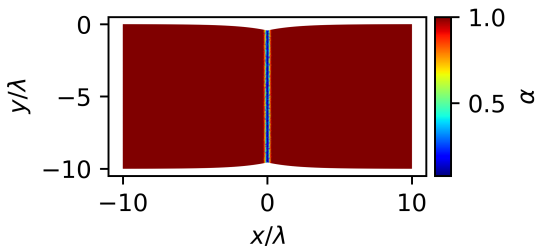

FIG. 8. Projection of $\alpha' = 1 - T/T_c$ onto a mesh, where $\alpha' = 0$ (i.e., $T \approx T_c$) in the region $|x|/\lambda \leq 0.125$ and $\alpha = 1$ elsewhere. The width of this region comes from experimental observations.

In the second scenario, vortices first fill the grain boundary, as in the first case, but then begin to penetrate into the grain from the boundary.

Once a vortex has penetrated into the grain boundary, it is pushed from the surface, allowing more vortices to come in after it. Once space is available, another vortex penetrates. This continues until the vortices have filled the grain boundary, i.e. an optimal spacing between the vortices inside grain boundary has been achieved. This is illustrated by the sequence in Figure 9. Note that vortices are manifest as regions in which the order parameter is reduced to near zero at their center and exponentially decay radially outward to unity.

If the applied magnetic field is sufficiently high, vortices will also begin to penetrate into the bulk once the grain boundary has been filled. See, for example, the bottom of Figure 9. The field at which vortices penetrate from the grain boundary into the grain is dependent on the distribution of $\alpha' = 1 - T/T_c$. The shallower the slope of α' the lower the applied field needs to be to nucleate vortices into the grain from the grain boundary. These results are summarized in the phase diagram in Figure 10. Comparing with results from section III, for a segregated region with $T_c \sim 5K$ in a cavity operating at $T = 4.2K$ ($T/T_c \sim 1$), we observe a non-trivial region of the phase diagram that admits flux trapped at the grain boundary.

The value of the applied field at which the vortices first leave the grain boundary and penetrate the bulk depends on the properties in the transition zone between the segregated and non-segregated region. If the transition form $\alpha' < 1$ (segregated region) to $\alpha' = 1$ (non-segregated region) is very sharp (as the blue solid curve in Figure 11), then vortices will be trapped in the grain boundary for larger fields. However, if the transition is more gradual (such as the orange dashed curve), then it is easier for vortices to escape the boundary and penetrate the bulk. Figures [8, 9, 10] were generated with a very sharp interface.

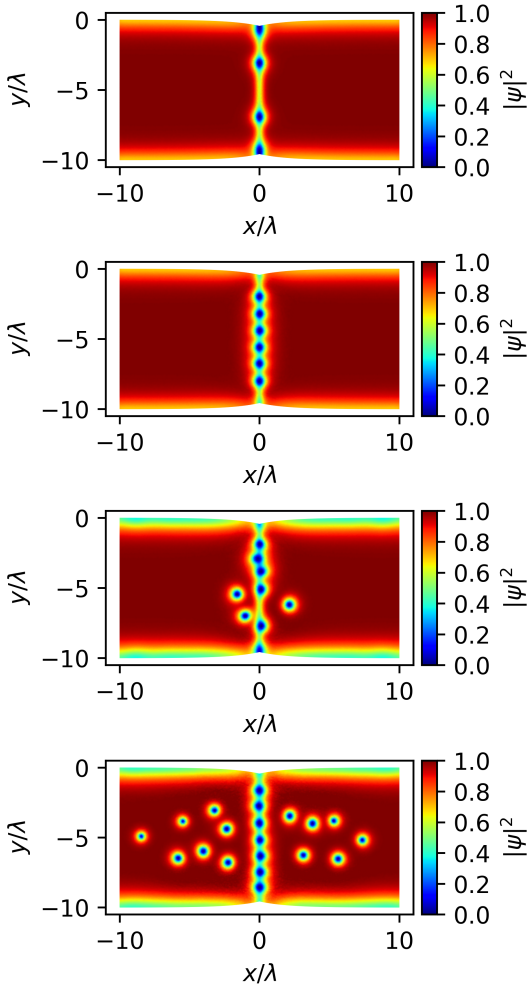

FIG. 9. Sequence of behaviors for increasingly large applied magnetic fields. An applied magnetic field is set as a boundary condition to the top and bottom of the film, with periodic boundary conditions on the right and left sides. At moderate applied magnetic fields, vortices penetrate only into the grain boundary from the geometric defect (top). At higher fields, a critical vortex spacing is reached (second pane) above which vortices begin to penetrate the bulk from the grain boundary (third pane). Finally, having entered the bulk, vortices disperse and fill the grain with an equilibrium distribution (bottom).

V. ESTIMATES OF VORTEX DISSIPATION AT GRAIN BOUNDARIES

Inhomogeneous properties of superconductors have high impact on the performance of SRF cavities, affecting figures of merit such as the residual resistance due

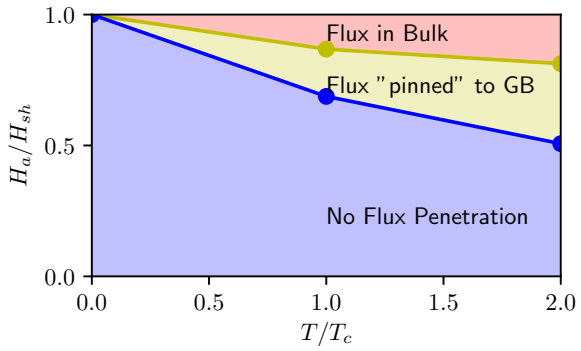

FIG. 10. Phase diagram of TDGL predictions for flux penetration in the presence of the grain boundary, interpolated from simulations at $\alpha' = -1, 0, 1$. At small applied fields, no flux penetrates (blues). At intermediate fields, flux penetrates but is constrained to the grain boundary (yellow). At sufficiently high fields, the flux penetrates from the grain boundary in to the bulk material (red).

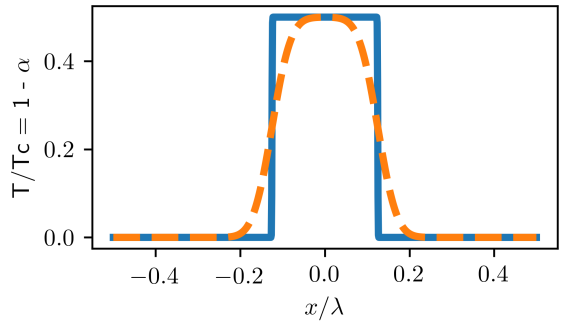

FIG. 11. Profiles of potential α' for the transition between the segregated and non-segregated regions. Sharp transitions (such as the blue solid curve) keep the vortices constrained to the boundary for larger applied fields. A more shallow transition (such as the orange dashed curve), however, allow vortices to escape into the grain more easily.

to trapped magnetic flux [33–35], and the superheating field [1, 2, 7, 36–38]. Grain boundaries well aligned with the surface magnetic field can become weak spots for the nucleation of superconducting vortices (see Fig. 12), and could be ultimately responsible for the quench of an SRF cavity. In this section, we discuss simple estimates for the power dissipation and heat diffusion due to nucleation of vortices at grain boundaries in Nb_3Sn cavities.

We start with an estimate for the power dissipated in an SRF cavity when a grain boundary is filled with n superconducting vortices. We assume of order $\mathcal{O}(n)$ vortex lines are annihilated once per cycle, their energy is lost, and the power dissipated per vortex line is simply the drop in the energy of the outside magnetic field times the

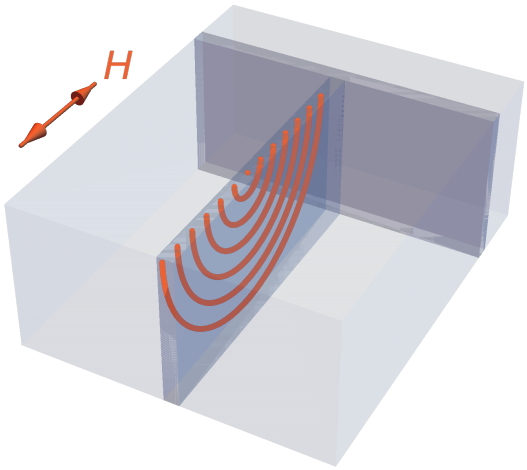

FIG. 12. Illustrating vortex nucleation (red lines) in a superconductor (light gray region) subject to a surface magnetic field H. Vortex entry starts at regions where superconductivity is weakest (dark gray regions, here representing grain boundaries).

RF frequency. Our estimate gives a rough estimate for the actual power dissipated by vortices at grain boundaries, if the field reaches high enough values for them to enter.

The drop in magnetic energy when a vortex line of length D nucleates into the superconductor is given by:

$$\Delta E = \left| \int \frac{1}{2\mu} \left(B - \frac{\Phi_0 D}{V} \right)^2 dV - \int \frac{B^2}{2\mu} dV \right| \approx \frac{B\Phi_0 D}{\mu}, \quad (1)$$

where V is the volume, μ is the permeability of free space, Φ_0 is the fluxoid quantum, and λ is the penetration depth. Note that ΔE is also approximately the work done by the external magnetic field to push a vortex into the bulk of the superconductor: $W \approx f_L \cdot D \cdot \lambda = (\Phi_0 B/(\mu\lambda))D\lambda = \Delta E$, where f_L is the Lorentz force per length. Thus, our calculation gives the vortex dissipation at grain boundaries assuming that the vortices do not leave the grain boundary as the external field drops and changes sign, as our simulations indicate, and as one would expect for vortices that enter a distance more than λ, past the surface nucleation barrier. The total energy drop for a grain boundary of linear size D with vortices spaced by λ (see Fig. 12) is $\Delta E_{GB} \approx \Delta E(D/\lambda) = B\Phi_0 D^2/(\mu\lambda)$, and the power dissipated per grain boundary is given by

$$P_{GB} \equiv f\Delta E_{GB} = \frac{B\Phi_0}{\mu}\frac{fD^2}{\lambda}, \quad (2)$$

where f is the cavity frequency. For a 1.3GHz Nb_3Sn

cavity with typical grain size of $D \approx 1\mu$m, we find $P_{GB} \approx 621$nW at $B = 60$mT.

Note that our estimate relies on the assumption that vortices quickly fill the grain boundary before being annihilated during the RF cycle. If the vortex line relaxes slowly, the RF field might vanish and change sign before vortices had time to fill the grain boundary, and our assumption would not be valid. We now show that that is not the case — vortices move at extremely high speeds in the typical environment of Nb_3Sn SRF cavities.

Consider the one-dimensional motion of a "train" of N vortices moving through a grain boundary towards the superconductor interior (see Fig. 13). Assuming overdamped dynamics, the equations of motion for each vortex line i of velocity v_i read:

$$\begin{aligned}
\eta v_1 &= f_L - f_{2,1}, \\
\eta v_2 &= f_{1,2} - f_{3,2}, \\
&\vdots \\
\eta v_{N-1} &= f_{N-2,N-1} - f_{N,N-1}, \\
\eta v_N &= f_{N-1,N},
\end{aligned}$$

where $f_L = \Phi_0 H_{rf}/\lambda$ is the Lorentz force per length at the surface, H_{rf} is the surface magnetic field, $\eta = {\Phi_o}^2/(2\pi\xi^2\rho_n)$ is the Bardeen-Stephen viscosity [39], ρ_n is the resistivity of the normal state and $f_{i,j}$ is the repulsion force from vortex i into vortex j. Thus,

$$\langle v \rangle \equiv \frac{1}{N}\sum_{i=1}^{N} v_i = \frac{f_L}{N\eta} = \frac{2\pi}{\mu\Phi_0}\frac{\rho_n\xi^2}{\lambda}\frac{B_{rf}}{N}. \tag{3}$$

For Nb_3Sn at $B_{rf} = 60$mT, we find $\langle v \rangle = 2.4\mu$m/ns and $\langle v \rangle = 24\mu$m/ns for ten vortices and one vortex, respectively. The average velocity of the vortex train is clearly high enough for vortices to quickly fill in the grain boundary during the RF cycle, but the numerical value should be taken with a grain of salt. The Bardeen-Stephen formula is not valid at these high speeds, which also exceed the pair-breaking limit of the superconducting condensate [40]. In recent work [41], Gurevich and Sheikhzada consider the dynamics of Abrikosov-Josephson vortices to model the dissipation by vortices at grain boundaries.

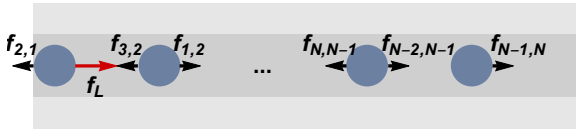

FIG. 13. Illustrating a "train" of N vortex lines (blue disks) moving through a grain boundary (dark gray) of a superconductor (light gray). The first vortex is subject to a surface Lorentz force from the RF field and each vortex is repelled by its nearest neighbors.

Grain boundary activation might be associated with the degradation of the quality factor Q of SRF cavities at high fields. We now use our estimates to calculate the number of active grain boundaries needed to deplete Q by a certain amount.

The quality factor is given by $Q = G{B_{rf}}^2/(2\mu^2 P)$, where P is the dissipated power per unit area and G is a geometry factor. We break up the total surface area s of the cavity into N blocks, so that $s = N s_{GB}$, where s_{GB} is the average area occupied by one grain boundary. Assume inactive and active blocks dissipate power P_1 and $P_1 + P_{GB}$, respectively, where by active block we mean a block with a grain boundary filled with vortices. For M active blocks,

$$\begin{aligned}
Q &= \frac{G{B_{rf}}^2}{2\mu^2(NP_1 + MP_{GB})/(Ns_{GB})} \\
&= \frac{G{B_{rf}}^2 s_{GB}}{2\mu^2(P_1 + xP_{GB})},
\end{aligned} \tag{4}$$

where $x \equiv M/N$ is the ratio of active grain boundaries. In the absence of active grain boundaries, we assume $Q = Q_1$ is constant (i.e. $P_1 \sim {B_{rf}}^2$), so that

$$P_1 = \frac{G{B_{rf}}^2 s_{GB}}{2\mu^2 Q_1}. \tag{5}$$

Plugging Eq. (5) into Eq. (4) and solving for x, we find

$$x = \frac{G s_{GB} {B_{rf}}^2}{2\mu^2 P_{GB}}\left(\frac{1}{Q} - \frac{1}{Q_1}\right). \tag{6}$$

Figure 14 shows a plot of the percentage of active grain boundaries ($100\,x$, blue curve) as a function of B_{rf} corresponding to the artificial Q-slope profile shown in the yellow curve (using Nb_3Sn parameters with $Q_1 = 10^{10}$, $s_{GB} = 0.5\mu$m^2 and $G = 278\Omega$). Note that about 0.03% of the surface grain boundaries need be filled with vortices for Q to drop from 10^{10} to 10^9 for Nb_3Sn at about 66mT.

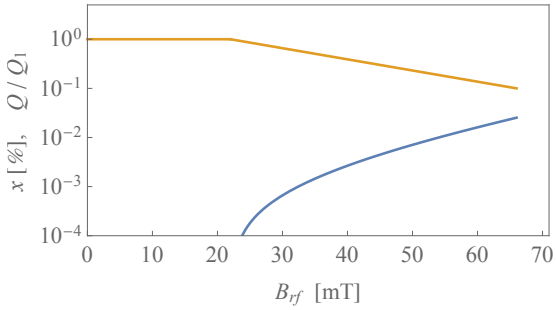

FIG. 14. Estimated percentage of active surface grain boundaries (blue curve) as a function of B_{rf}, corresponding to the quality factor profile displayed in the yellow curve for Nb_3Sn with $Q_1 = 10^{10}$.

We end this section with a simple model calculation of the steady-state thermal heating at a grain bound-

ary. Figure 15 illustrates our model for thermal diffusion near an active grain boundary. Light and dark gray regions represent cross sections of Nb and Nb_3Sn layers, respectively. The Nb surface is in contact with a low-temperature He bath. The Nb_3Sn surface is in contact with vacuum, and is subject to a parallel oscillating magnetic field. The grain boundary is represented by a blue rectangle of linear size D. Red arrows represent the direction for heat diffusion in our model. First, we assume one-dimensional heat diffusion away from the grain boundary up to a distance $r \approx D$. We expect the heat front to attain a semi-spherical shape for distances $r \gtrapprox D$. We then assume three-dimensional heat diffusion away from a half-sphere of radius D for distances $D \leq r \leq R_1$. For $r \leq R_1$ we consider the Nb_3Sn thermal conductivity $\kappa = \kappa_{\mathrm{Nb3Sn}}$. At last, we assume three-dimensional heat diffusion away from a half-sphere of radius R_1 for distances $R_1 \leq r \leq R_2$, with κ given by the Nb thermal conductivity κ_{Nb}. Note that our assumptions are stronger when $R_2 \gg R_1$ ($R_2/R_1 \sim 10^3$ for typical Nb_3Sn/Nb SRF cavities).

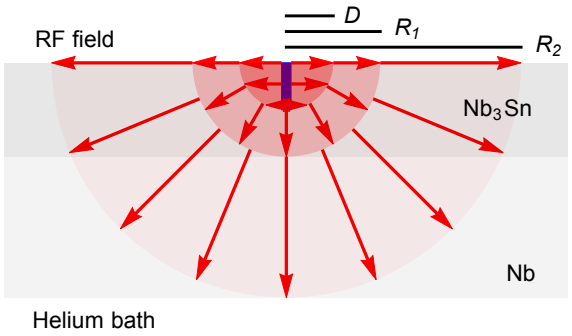

FIG. 15. Sketch of our model for heat diffusion near an active grain boundary (blue rectangle at the top center). The light and dark gray regions correspond to cross sections of Nb and Nb_3Sn. Red arrows represent the direction for heat diffusion. Heat fronts move along one dimension for distances smaller than the grain size D, and three dimensions otherwise.

The equilibrium temperature profile can then be cast from the stationary solutions of the heat equation in each region:

$$T(r) = \begin{cases} \zeta(r), & \text{for } 0 \leq r \leq D, \\ c/r + d, & \text{for } D \leq r \leq R_1, \\ e/r + f, & \text{for } R_1 \leq r \leq R_2, \end{cases} \tag{7}$$

where c, d, e and f are constants, and $\zeta(r)$ is the stationary solution of the one-dimensional heat equation (the Nb_3Sn thermal conductivity strongly varies with temperature in this region [42], which complicates the problem of finding an analytical solution for $\zeta(r)$) [43]. Note that we relax the definition of the coordinate r here, which should be interpreted as a lateral distance away from the grain boundary for $0 \leq r \leq D$, and a depth coordinate towards the Helium bath for distances $r > D$.

To calculate $\zeta(r)$, we use Fourier's law — $\dot{\mathcal{Q}} = -\kappa\, dT/dr$, where $\dot{\mathcal{Q}}$ is the heat flux. The stationary solution of the heat equation can be found from the solution of $d\dot{\mathcal{Q}}/dr = 0$, *i.e.*

$$-\kappa_{\mathrm{Nb3Sn}}(T)\, \frac{dT}{dr} = a, \tag{8}$$

where a is constant.

The thermal conductivity $\kappa_{\mathrm{Nb3Sn}}(T)$ in the superconducting layer has two important contributions: a phonon contribution and an electronic component (carried by superconducting quasiparticles). The low-temperature phonon thermal conductivity is strongly dependent on the morphology of the crystal [44]; in clean insulating crystals it is dominated by scattering off grain boundaries and sample boundaries, and varies as T^3. Scattering off impurities can cut off the contribution of high-frequency phonons, or even resonantly cut off certain frequency bands. All of these mechanisms lead to a thermal conductivity that monotonically increases with temperature, so we avoid the complexity by using a constant phonon thermal conductivity k_1, giving a lower bound for the conductivity and hence an upper limit to the heating. The electronic portion of the thermal conductivity k_2 in the normal metal at low temperatures is roughly independent of temperature, and is set by the electronic mean-free path. In the superconductor, it decreases exponentially as $\exp(-\Delta(0)/k_B T)$, as seen experimentally [42]. Using the BCS relation between the gap and the transition temperature, we therefore use

$$\kappa_{\mathrm{Nb3Sn}}(T) = k_1 + k_2 \exp\left(-1.76\, T_c/T\right). \tag{9}$$

We use the normal electron thermal conductivity $k_2 = 2 \times e^{1.76}$ W/m·K from [42]. Because the electronic contribution is negligible at the operating temperature of the cavity, we set $k_1 = 10^{-2}$W/m·K as the approximate total thermal conductivity of Nb_3Sn at 2K [42]. Both of these constants are dependent upon the preparation of the film, and also could vary from one region of the film to another as the growth conditions or the underlying Nb grain orientations vary.

Integration of Eq. (8) results in

$$\Pi\left(T\right) = -a\, r + b, \tag{10}$$

where b is constant, and

$$\begin{aligned} \Pi\left(T\right) =& k_1\, T + k_2\, T\, e^{-1.76 T_c/T} \\ &+ 1.76\, k_2\, T_c\, E_i\left(-1.76 \frac{T_c}{T}\right), \end{aligned} \tag{11}$$

with $E_i(x) \equiv \int_{-x}^{\infty} [e^{-t}/t] dt$ denoting the exponential integral function. $\zeta(r)$ is then the solution of Eq. (10) for T. Note that our simple model assumes that the quasiparticles and the phonons remain at the same effective temperature (the inelastic electronic mean free path is small), and that both remain diffusive (the elastic phonon and

electron mean free paths are small). Violating either of these assumptions would likely lower the transport of energy away from the grain boundary, making the heating more dangerous.

We focus our attention on grain-boundary activation and ignore other sources of power dissipation (which could be added later using the principle of superposition). Thus, we assume that the heat flux is the power dissipated per grain boundary (P_{GB}) per unit area. We use Fourier's law to determine the coefficients a, c and e in Eqs. (7) and (10). For $0 \leq r \leq D$, $\dot{\mathcal{Q}} = P_{GB}/D^2$, so that:

$$a = \frac{P_{GB}}{D^2}. \tag{12}$$

For $D \leq r \leq R_1$ ($R_1 \leq r \leq R_2$), $\dot{\mathcal{Q}} = P_{GB}/2\pi r^2$, $\kappa = \kappa_{\mathrm{Nb3Sn}}$ (κ_{Nb}) and $dT/dr = -c/r^2$ ($-e/r^2$), so that:

$$c = \frac{P_{GB}}{2\pi\kappa_{\mathrm{Nb3Sn}}}, \quad e = \frac{P_{GB}}{2\pi\kappa_{\mathrm{Nb}}}. \tag{13}$$

To find f, we use $T(R_2) = T_{\mathrm{He}}$, where T_{He} is the temperature of the Helium bath:

$$f = T_{\mathrm{He}} - \frac{P_{GB}}{2\pi\kappa_{\mathrm{Nb}}R_2}. \tag{14}$$

To find d and b, we use the continuity of $T(r)$ at $r = R_1$ and $r = D$, respectively (we ignore the Kapitza resistance at the interface between Nb_3Sn and Nb). Thus,

$$c/R_1 + d = e/R_1 + f \quad \Rightarrow \quad d = \frac{e-c}{R_1} + f, \tag{15}$$

and

$$b = aD + \Pi\left(\frac{c}{D} + d\right). \tag{16}$$

Figure 16 shows temperature profiles (Eq. (7)) near an active grain boundary for Nb_3Sn/Nb systems at $B = 60$mT. Note that the temperature of an active grain boundary increases to about 10K near the boundary surface for a Helium temperature of 2K. Although this increase in temperature is not large enough to drive Nb_3Sn into the normal state, it certainly has significant impact on the superconducting properties. Also, note that the temperature decays to nearly T_{He} as r approaches twice the grain size D, suggesting that heating due to grain-boundary activation is mostly localized.

A temperature rise of 10K at the grain boundary is over half of the critical temperature of the film, suggesting that larger grain boundaries or multiple nearby boundaries could raise the temperature high enough to quench the cavity. Cavities with tin-rich grain boundaries and more pristine grain boundaries show the same quench fields, suggesting that another mechanism controls the quench fields of existing Nb_3Sn cavities. If the excess dissipation in the cavities with tin-rich boundaries is due to vortex penetration (Fig. 14), one would expect

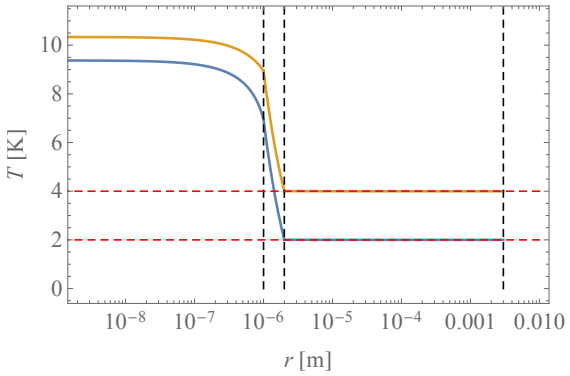

FIG. 16. Temperature as a function of distance from the grain boundary for the Nb_3Sn/Nb system at a bath of 2K (blue) and 4K (yellow). Vertical dashed lines correspond to $D = 1\mu$m, $R_1 = 2\mu$m and $R_2 = 3$mm, from left to right. Bottom and top red dashed lines correspond to $T_{\mathrm{He}} = 2$K and 4K, respectively. We have used temperature-dependent κ_{Nb3Sn} given by Eq. (9), $\kappa_{\mathrm{Nb}} = 10$W/m·K, and $P_{GB} = 621$nW at $B = 60$mT, according to our previous estimates.

rare events with large or multiple grain boundaries would happen, suggesting that our grain-boundary heating estimate is unduly pessimistic. Alternatively, it remains possible that the grain boundaries have high superheating fields, and the excess dissipation has another explanation. In any case, our estimates suggest that vortex entry at grain boundaries should be expected for tin-rich boundaries well below the superheating field for a perfect crystal, and that the subsequent heat release should be important both as a contribution to the overall dissipation and as a quench mechanism for the cavity.

VI. CONCLUSION

In this work we have presented an interdisciplinary, multi-scale study of vortex nucleation in Sn-segregated grain boundaries and its subsequent effect on SRF performance. Scanning transmission electron microscopy images and energy dispersive spectroscopy show Sn concentration as high as ∼35 at.% and widths ∼3nm in chemical composition in grain boundaries. We used density functional theory to estimate the effective critical temperature for the material in the segregation zone and find that the effective T_c can be reduced to as low as 5 K for Sn concentrations in excess of ∼30 at.%. Next, we used these calculations as inputs into time-dependent Ginzburg-Landau simulations. These simulations demonstrate that grain boundaries can act as nucleation sites for magnetic vortices. The grain boundaries then act as a kind of pinning sites for vortices after nucleation. The pinning is non-traditional, however, as vortices are free to move vertically along the grain boundary, but are constrained

from moving laterally into the bulk. We have seen that for a range of applied fields, vortices may nucleate at but remain constrained to the grain boundary. These vortices will nucleate and annihilate once per RF cycle, and we estimate the superconducting losses of this phenomenon at the scale of SRF cavities. We have shown that as long as vortices do not penetrate the bulk grain, losses are localized near the grain boundary and will not lead to a global quench. However, the annihilation process each cycle will lead to a reduction in the quality factor that increases with larger applied fields, consistent with the experimentally observed Q-slope.

SRF cavities are an important application area that require multi-disciplinary talents to address. This study has leveraged the skills of accelerator physicists, material scientists, and condensed matter theorists with expertise across a range of scales to explore a question fundamental to the advancement of next-generation SRF material, Nb_3Sn. This study has presented evidence that segregation zones in grain boundaries play an important role in cavity performance. Understanding the mechanism behind the Q-slope will motivate new manufacturing protocols and help constrain the design space of future cavities.

VII. ACKNOWLEDGEMENT

We would like to thank Matthias Liepe, Michelle Kelley, and Richard Hennig for helpful conversations. This research is supported by the United States Department of Energy, Offices of High Energy. Fermilab is operated by the Fermi Research Alliance LLC under Contract No. DE-AC02-07CH11359 with the United States Department of Energy. This work made use of the EPIC, Keck-II, and/or SPID facilities of Northwestern Universitys NUANCE Center, which received support from the Soft and Hybrid Nanotechnology Experimental (SHyNE) Resource (NSF ECCS-1542205); the MRSEC program (NSF DMR-1121262) at the Materials Research Center; the International Institute for Nanotechnology (IIN); the Keck Foundation; and the State of Illinois, through the IIN. This work was supported by the US National Science Foundation under Award OIA-1549132, the Center for Bright Beams.

[1] D. B. Liarte, S. Posen, M. K. Transtrum, G. Catelani, M. Liepe, and J. P. Sethna, Superconductor Science and Technology **30**, 033002 (2017).
[2] M. K. Transtrum, G. Catelani, and J. P. Sethna, Physical Review B **83**, 094505 (2011).
[3] S. J. Chapman, SIAM Journal on Applied Mathematics **55**, 1233 (1995).
[4] A. J. Dolgert, S. J. Di Bartolo, and A. T. Dorsey, Physical Review B **53**, 5650 (1996).
[5] L. Kramer, Physical Review **170**, 475 (1968).
[6] S. Posen, N. Valles, and M. Liepe, Physical review letters **115**, 047001 (2015).
[7] G. Catelani and J. P. Sethna, Physical Review B **78**, 224509 (2008).
[8] F. P.-J. Lin and A. Gurevich, Physical Review B **85**, 054513 (2012).
[9] A. R. Pack, J. Carlson, S. Wadsworth, and M. K. Transtrum, arXiv preprint arXiv:1911.02132 (2019).
[10] A. Y. Aladyshkin, A. Mel'Nikov, I. Shereshevsky, and I. Tokman, Physica C: Superconductivity **361**, 67 (2001).
[11] L. Burlachkov, M. Konczykowski, Y. Yeshurun, and F. Holtzberg, Journal of applied physics **70**, 5759 (1991).
[12] D. Y. Vodolazov, Physical Review B **62**, 8691 (2000).
[13] P. Soininen and N. Kopnin, Physical Review B **49**, 12087 (1994).
[14] S. Posen and D. L. Hall, Superconductor Science and Technology **30**, 033004 (2017).
[15] S. Posen and M. Liepe, Physical Review Special Topics-Accelerators and Beams **17**, 112001 (2014).
[16] S. Posen, J. Lee, O. Melnychuk, Y. Pischalnikov, D. Seidman, D. Sergatskov, and B. Tennis, in *19th Int. Conf. on RF Superconductivity (SRF'19), Dresden, Germany, 30 June-05 July 2019* (JACOW Publishing, Geneva, Switzerland, 2019) pp. 818–822.
[17] G. Müller, H. Piel, J. Pouryamout, P. Boccard, and P. Kneisel, in *Proceedings of the Workshop on Thin Film Coating Methods for Superconducting Accelerating Cavities* (2000).
[18] A. Gurevich, Superconductor Science and Technology **30**, 034004 (2017).
[19] D. L. Hall, *New Insights into the Limitations on the Efficiency and AchievableGradients in Nb 3 Sn SRF Cavities* (Cornell University, 2017).
[20] J. Lee, S. Posen, Z. Mao, Y. Trenikhina, K. He, D. L. Hall, M. Liepe, and D. N. Seidman, Superconductor Science and Technology **32**, 024001 (2018).
[21] Y. Trenikhina, S. Posen, A. Romanenko, M. Sardela, J.-M. Zuo, D. Hall, and M. Liepe, Superconductor Science and Technology **31**, 015004 (2017).
[22] C. Becker, S. Posen, N. Groll, R. Cook, C. M. Schlepütz, D. L. Hall, M. Liepe, M. Pellin, J. Zasadzinski, and T. Proslier, Applied Physics Letters **106**, 082602 (2015).
[23] J. Lee, Z. Mao, K. He, Z. H. Sung, T. Spina, S.-I. Baik, D. L. Hall, M. Liepe, D. N. Seidman, and S. Posen, Acta Materialia **188**, 155 (2020).
[24] S. J. Dillon, M. Tang, W. C. Carter, and M. P. Harmer, Acta Materialia **55**, 6208 (2007).
[25] W. L. McMillan, Physical Review **167**, 331 (1968).
[26] R. Sundararaman, K. Letchworth-Weaver, K. A. Schwarz, D. Gunceler, O. Y., and T. A. Arias, SoftwareX **6**, 278 (2017).
[27] N. S. Sitaraman, J. Carlson, A. R. Pack, R. D. Porter, M. U. Liepe, M. K. Transtrum, and T. A. Arias, arXiv preprint arXiv:1912.07576 (2019).
[28] N. Marzari and D. Vanderbilt, Physical Review B **56**, 12847 (1997).
[29] H. Devantay, J. L. Jorda, M. Decroux, J. Muller, and R. Flkiger, Materials Science **16**, 21452153 (1981).

[30] M. S. Alnæs, J. Blechta, J. Hake, A. Johansson, B. Kehlet, A. Logg, C. Richardson, J. Ring, M. E. Rognes, and G. N. Wells, Archive of Numerical Software **3** (2015), 10.11588/ans.2015.100.20553.

[31] A. Logg, K.-A. Mardal, and G. Wells, *Automated solution of differential equations by the finite element method: The FEniCS book*, Vol. 84 (Springer Science & Business Media, 2012).

[32] H. Gao and W. Sun, Journal of Computational Physics **294**, 329 (2015).

[33] A. Gurevich and G. Ciovati, Phys. Rev. B **87**, 054502 (2013).

[34] D. Hall, D. Liarte, M. Liepe, R. Porter, and J. Sethna, in *Proc. of International Conference on RF Superconductivity (SRF'17), Lanzhou, China, July 17-21, 2017*, International Conference on RF Superconductivity No. 18 (JACoW, Geneva, Switzerland, 2018) pp. 844–847, https://doi.org/10.18429/JACoW-SRF2017-THPB042.

[35] D. B. Liarte, D. Hall, P. N. Koufalis, A. Miyazaki, A. Senanian, M. Liepe, and J. P. Sethna, Phys. Rev. Applied **10**, 054057 (2018).

[36] L. Kramer, Phys. Rev. **170**, 475 (1968).

[37] D. B. Liarte, M. K. Transtrum, and J. P. Sethna, Phys. Rev. B **94**, 144504 (2016).

[38] V. Ngampruetikorn and J. A. Sauls, Phys. Rev. Research **1**, 012015 (2019).

[39] J. Bardeen and M. J. Stephen, Phys. Rev. **140**, A1197 (1965).

[40] L. Embon, Y. Anahory, Ž. L. Jelić, E. O. Lachman, Y. Myasoedov, M. E. Huber, G. P. Mikitik, A. V. Silhanek, M. V. Milošević, A. Gurevich, *et al.*, Nature communications **8**, 85 (2017).

[41] A. Sheikhzada and A. Gurevich, Phys. Rev. B **95**, 214507 (2017).

[42] G. D. Cody and R. W. Cohen, Rev. Mod. Phys. **36**, 121 (1964).

[43] Note that the temperature dependence of the thermal conductivity of Nb_3Sn should also change the stationary solution of the three-dimensional heat equation for $D \leq r \leq R_1$. Here we ignore this effect for the sake of mathematical simplicity, since our qualitative conclusions are not altered if we incorporate the temperature dependence of κ in this region.

[44] D. G. Cahill and R. O. Pohl, Annual Review of Physical Chemistry **39**, 93 (1988), https://doi.org/10.1146/annurev.pc.39.100188.000521.

Chapter 4

Material-Specific Ginzburg-Landau Simulations

4.1 Abstract

This chapter extends GL simulations of defects and vortex dynamics. We adapt our formulation to accommodate material-specific parameters. Next we simulate regions of depleted Sn near the surface of a superconducting film and show that as the defect gets deeper into the film it has less of an impact on H_{sh}. We call these "islands of deficient Sn". We simulate AC fields and observe an increase in H_{sh} with higher frequencies. We also observe vortex antivortex annihilation. Finally, we simulate the process of cooling an SRF cavity by simulating a temperature wave. We observe that this wave can push vortices.

4.2 Introduction

As discussed in chapter 2 working with the GL equations usually involves absorbing many constant parameters into the units of length and time. Allowing variations in these parameters leads to a

different process of nondimensionalization. Up to this point we've considered variations in geometry by adding surface roughness and change material by varying the critical temperature through the parameter $\alpha \propto 1 - \frac{T}{T_c(r)}$. These have been useful for a general qualitative understanding of how defects impact superconductor performance but a quantitative material-specific simulation requires spatial and temporal variations of the other parameters.

To do so we need to reconsider our formulation. The GL equations are derived by taking the first variation of the GL free energy and setting it to zero [46]. This requires an integration by parts to move spatial derivatives off the variations and onto the functions we are solving for. This process also defines the boundary conditions. If we introduce spatial dependence to parameters on terms with derivatives then the integration by parts will change the equations of motion and boundary conditions. For this reason we postpone adding spatial variations to the effective mass until chapter 5.

The next step is to discretize the equations. Previously we followed Gao's mixed finite element formulation [47]. The trick to this formulation is to not only solve for Δ and $\mathbf{A}$ but for $\sigma = \nabla \times \mathbf{A}$ and $\theta = \nabla \cdot \mathbf{A}$ by taking the curl and divergence of the equation for $\mathbf{A}$. Unfortunately adding spatial dependencies to terms of the form $f(r)\frac{\partial \mathbf{A}}{\partial t}$ means that when we take spatial derivatives of the equations we get $\nabla \cdot (f(r)\frac{\partial \mathbf{A}}{\partial t}) = \nabla f(r) \cdot \frac{\partial \mathbf{A}}{\partial t} + f(r)\frac{\partial \theta}{\partial t}$. Now, what is supposed to be just an equation for θ also contains time derivatives of $\mathbf{A}$. The details on how we work around this are given in appendix A.

In this new formulation we can vary the penetration depth λ_0, the critical magnetic field H_{c0}, the conductivity σ, the decay rate of the order parameter Γ, the temperature T, and the critical temperature T_c. Values for some of these parameters in bulk material are given in table 4.1. As we saw in chapter 3 these values may change in defects.

Notice σ and Γ are not included in this table. In principle these parameters can be calculated from DFT. For now we set $\sigma = 1$. As Γ sets the time scale, we use Kopnin's rough estimate

	H_c (T)	T_c (K)	λ_0 (nm)	ξ_0 (nm)
Nb	0.82 [50]	9.26 [51]	50 [52]	22 [53]
Nb_3Sn	30 [54]	18.3 [55]	111 [56]	4.2 [56]

Table 4.1 Table of values of the critical magnetic field H_c, critical temperature T_c, penetration depth λ_0, and coherence length ξ_0 for Nb and Nb_3Sn. Note that Nb_3Sn has both a larger critical magnetic field and a larger critical temperature. In theory Nb_3Sn cavities could out perform Nb cavities.

of $u = \frac{\tau_\Delta}{\tau_j} = 5.79$ in the dirty limit. Tinkham and Kopnin provide formulas for converting these parameters into α, τ_Δ, etc [48, 49].

4.3 Islands of Deficient Sn

Simulations in this section were run by Braedon Jones.

Islands of deficient Sn in the surface of SRF cavities have been observed experimentally [57]. One such defect is shown in the yellow circle in figure 4.1. From chapter 3 we know that variations of Sn concentration in the Nb_3Sn layer can lead to a reduction in T_c.

We want to know how the size, location, and variations in Sn concentration each impact the superheating field. To do so we will use the film geometry discussed in chapter 2. As a reminder, we enforce periodic boundary conditions on the left and right of the domain. We also enforce fixed applied fields and zero current leaking off the top and bottom of the domain. We model the decrease of T_c in this region through α. We define α as a 2D error function as follows,

$$\alpha = 1.0 - 0.5B\left(-erf\left(\gamma\left(\left(\frac{x-cx}{xR}\right)^2 + \left(\frac{y-cy}{yR}\right)^2 - 1\right)\right) + 1\right) \tag{4.1}$$

where B is the lowest value of α, γ determines the slope of the transition between regions, cy and cx indicate the center of the island and xR and yR are the heights and widths of the island.

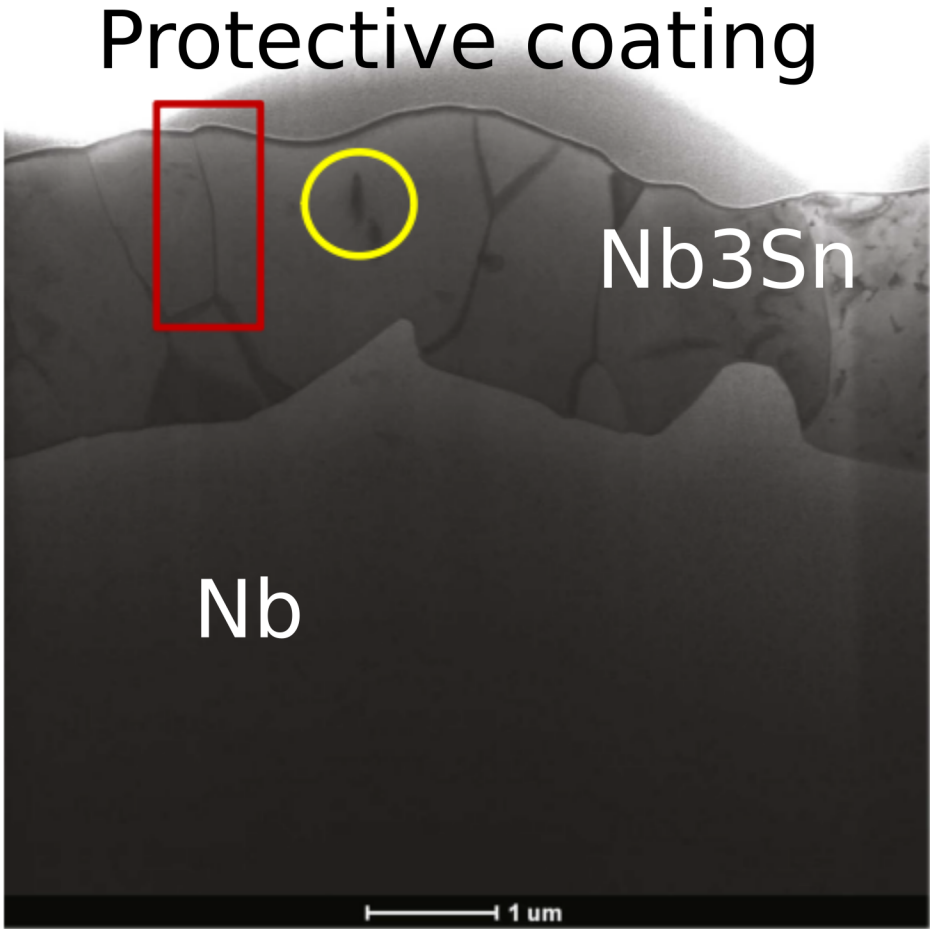

Figure 4.1 Experimental image of the surface of a Nb_3Sn cavity. Nb_3Sn cavities are made by depositing Sn onto a Nb cavity and heating the surface to allow diffusion of Sn into the bulk Nb. This produces a layer of Nb_3Sn. The yellow circle shows an island defect. Our collaborators hypothesize these are islands of deficient Sn. The red box outlines a grain boundary. We simulated grain boundaries in a previous chapter. In this chapter we simulate the islands of depleted Sn. Image used with permission with added indicators for clarity [57].

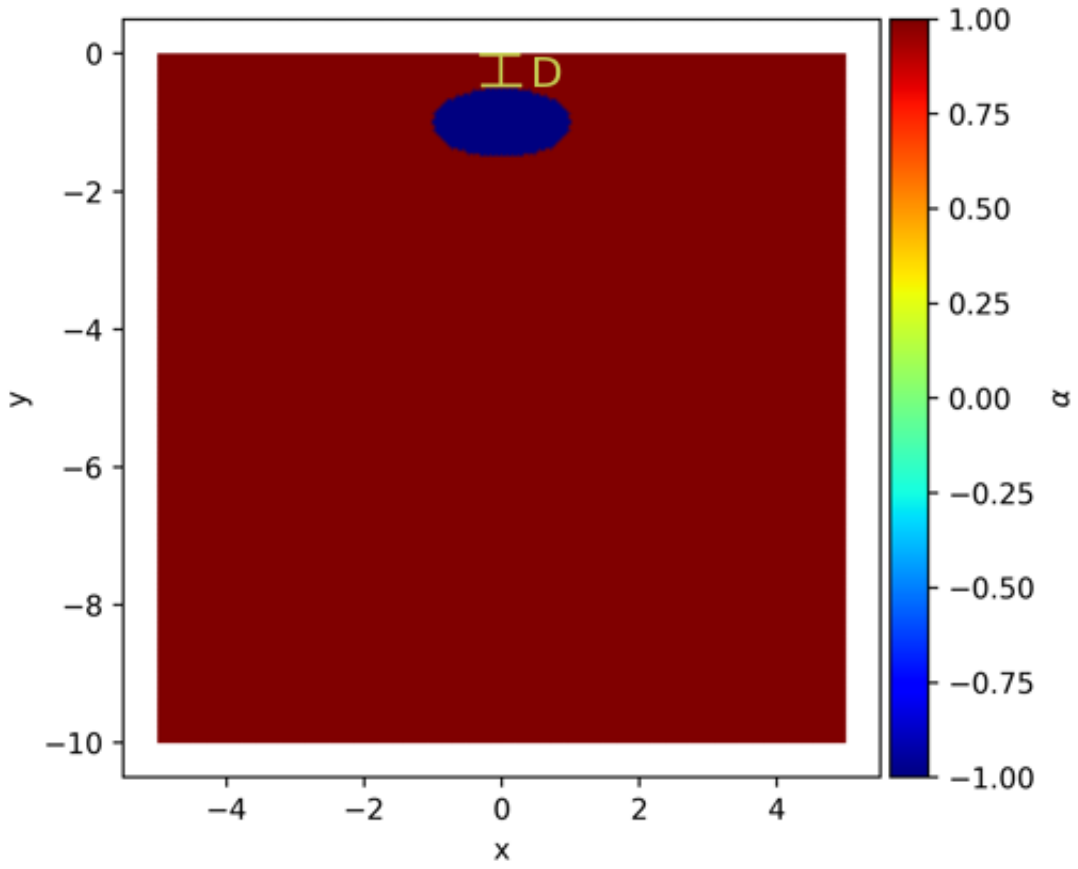

Figure 4.2 Figure showing α. The reduction in T_c due to an island of depleted Sn is modeled as a reduction in α, a parameter in the Ginzburg-Landau equations. We adjust the size, depth, position, and slope of α to explore what kinds of islands are the most detrimental. In this case the slope is so high that α behaves as a step function. D indicates the distance of the top of the defect to the top of the domain. We apply a magnetic field on the top and bottom of the domain and assume periodic boundary conditions on the left and right sides of the domain.

We can adjust the position, shape, slope, and depth of α to see which parameters have the greatest impact on H_{sh}. Figure 4.2 shows an example of α with very steep slope (essentially a step function). Unless otherwise stated $\kappa = 4$, $u = 1$, $yR = 1$, $xR = 2$, the minimum of alpha reaches 0.5, and has a very steep slope essentially behaving as a step function. Our evaluation of the superheating

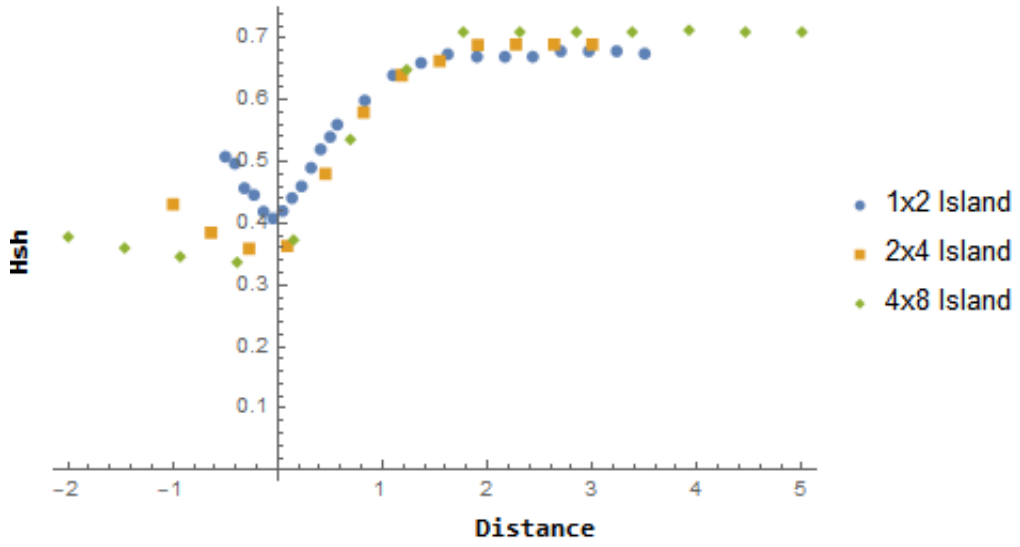

Figure 4.3 Plot of H_{sh} vs. the distance of the top of the island of deficient Sn from the top of the superconducting film with varying island size. For all sizes the impact of the island drops off when the island is 2λ below the surface. Larger islands have a broader range of values that reduce H_{sh}.

field is identical to the process in chapter 2.

We explore how islands of varying size, depth, and slope impact H_{sh} as we move the island from outside the film to its interior. Our measure of "distance" is how far the top of the island is from the top of the film. This is marked as D in figure 4.2. A negative distance means the top of the island is above the film's top surface. In the figures of this section we observe that the greatest reduction in H_{sh} occurs as the island lies halfway into the film. As the island gets deeper into the film the reduction in H_{sh} shrinks until at about 2λ the island no longer has a significant impact.

In figure 4.3 we vary the size of the island. The larger the island the more H_{sh} is reduced. There is also a larger range of distances with which H_{sh} is reduced.

In figure 4.4 we vary the depth of α. This is equivalent to removing more Sn, causing an increase of T_c. We observe that the lower α becomes the greater the reduction in H_{sh}.

In figure 4.5 we vary the slope with which α varies. This simulates how quickly the material transitions from Nb_3Sn to Nb. We observe that steep slopes reduce H_{sh} the most.

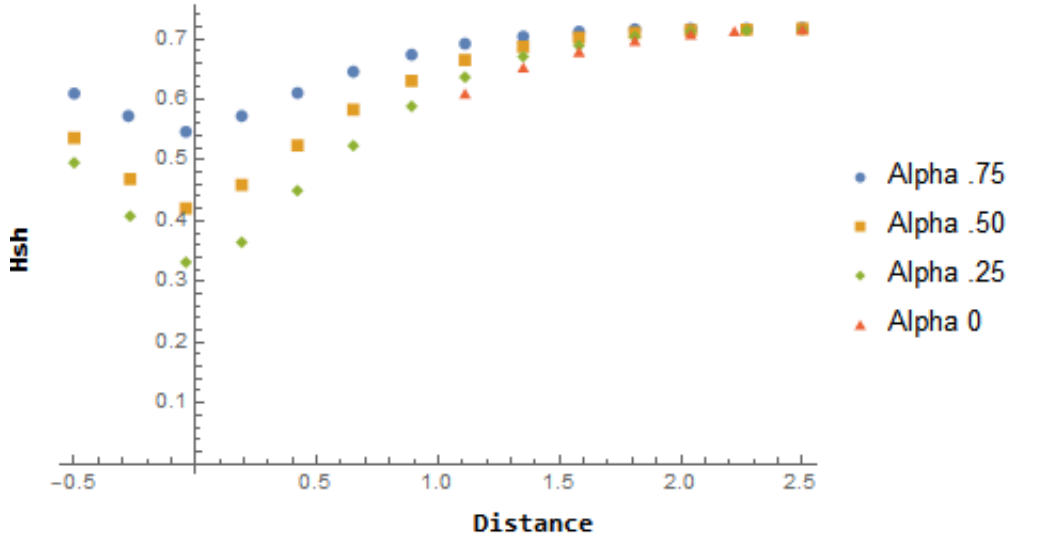

Figure 4.4 Plot of H_{sh} vs. the distance of the top of the island of deficient Sn from the top of the superconducting film with varying reductions of Tc. Islands with lower alpha represent greater reductions in T_c due to deviations from pure Nb_3Sn. The greater reduction in alpha leads to a greater reduction in H_{sh}.

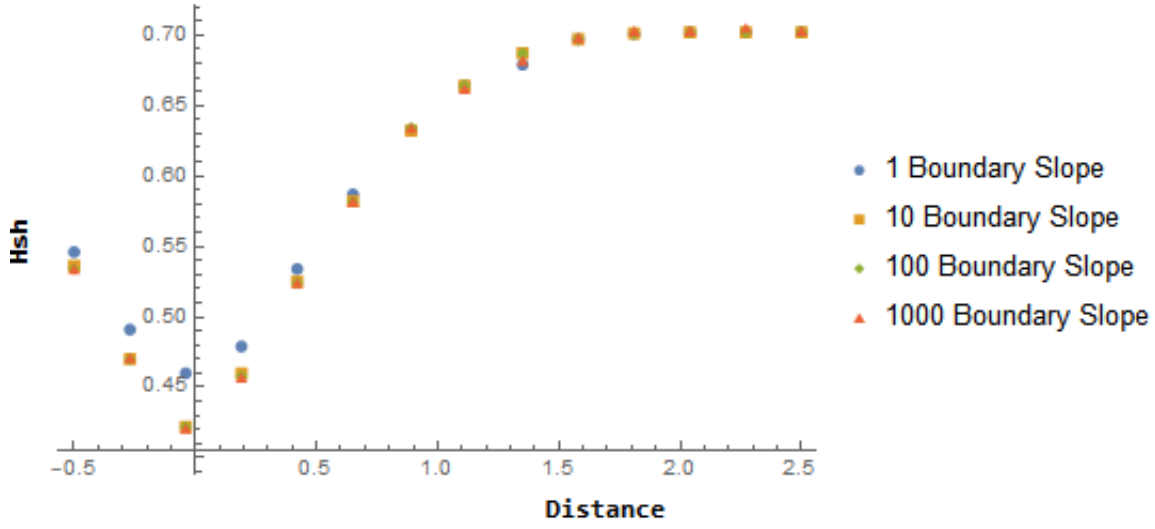

Figure 4.5 Plot of H_{sh} vs. the distance of the top of the island of deficient Sn from the top of the superconducting film with varying reductions of island slope. Islands with a quick change from Nb3Sn to depleted Sn have a greater reduction on H_{sh}. This effect is not as pronounced as varying the reduction in T_c.

4.4 AC Fields

Simulations in this section were run by Cole Abbot.

There are two proposed ways to improve SRF cavities, raising H_{sh} [44] or increasing the AC current's frequency [39]. The second proposal is based on the finite time it takes vortices to form. Theoretically at high frequencies there would not be enough time for a vortex to penetrate.

Another concern that has arisen is the possibility of vortex antivortex annihilation. Vortices nucleating into grain boundaries could become pinned by defects. When the magnetic field swaps sign a new set of vortices with opposite magnetic field could enter and annihilate the pinned vortices. This could be a mechanism for cavity heating. (See chapter 4)

Both of these concerns can be analyzed using AC fields in our simulations. To do so we use the film geometry. We apply an AC magnetic field on the top and bottom of the film. Care is taken to insure the numerical time step is much smaller than the period of oscillation.

Our bifurcation algorithm can not calculate H_{sh} for oscillating fields, but we can observe when the order parameter drops to zero on the surface. Varying the frequency and strength of the applied magnetic field we let our simulations run for several periods to determine if the order parameter gets close to zero. If so we infer that we are above H_{sh}.

There are a wide variety of vortex behaviors depending on the magnitude of the applied magnetic field and the frequency with which it is applied. For small magnetic fields the order parameter drops only near the surface. For medium magnetic fields and high frequencies vortices enter but are quickly pulled out with the change of magnetic field. For medium magnetic fields and low frequencies vortices enter and move deep into the film. When the magnetic field crosses zero some vortices exit the material. Then antivortices penetrate and annihilate with the vortices that remain. In figure 4.6 we plot the magnetic field during vortex antivortex annihilation. In the top right of the image we can see a region of positive magnetic field right next to a region of negative magnetic field. These two vortices are just about to come together and annihilate. For very large magnetic

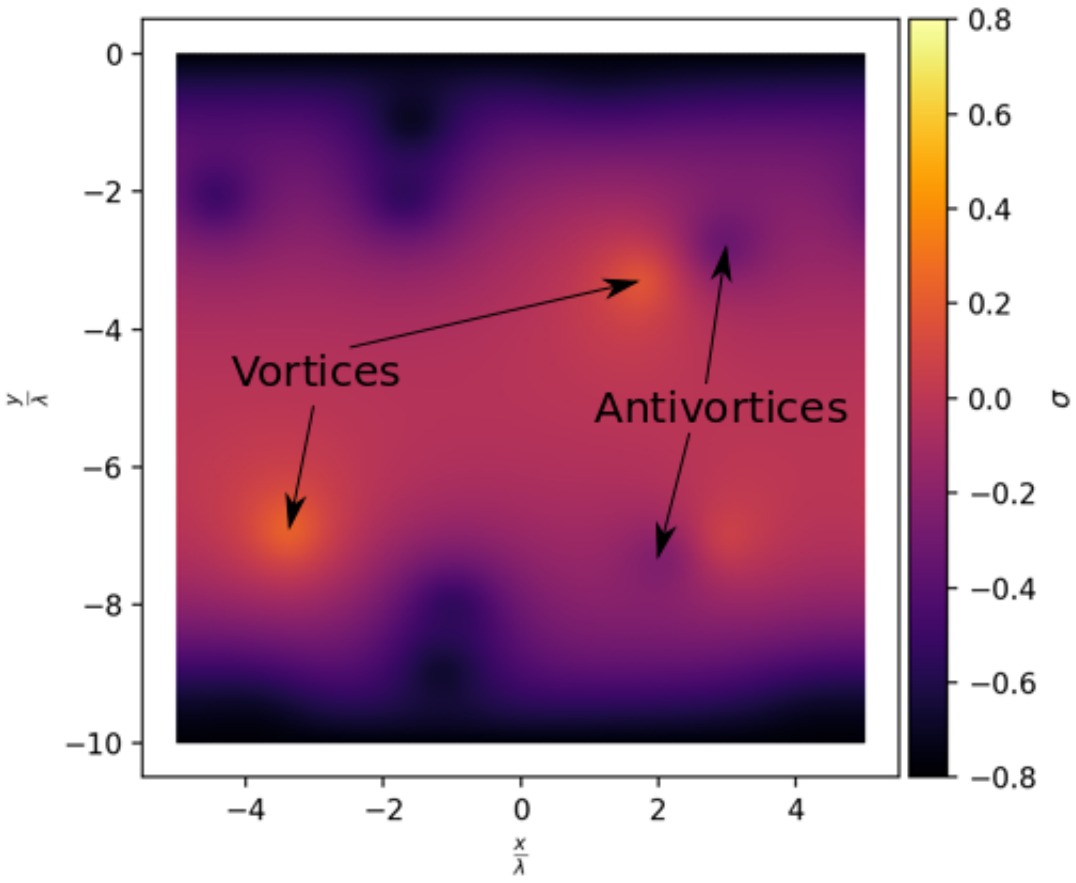

Figure 4.6 Plot of the magnetic field inside a film during vortex antivortex annihilation on a square domain. We apply a sinusoidal magnetic field on the top and bottom, and periodic boundary conditions on the left and right. For sufficiently large magnetic fields vortices form. When the magnetic field switches signs the vortices that form have opposite orientation. The yellow spots are vortices and the purple spots are antivortices. On the top right we can see a vortex and antivortex pair about to annihilate each other. This interaction may produce extra heat.

fields the surface partially quenches twice over each period.

To answer the question of whether or not frequency has an impact on H_{sh}, we ran many simulations varying the magnitude of the applied magnetic field and the frequency. In figure 4.7 the white dots indicate the order parameter did not drop to zero, meaning we are below H_{sh}. The blue

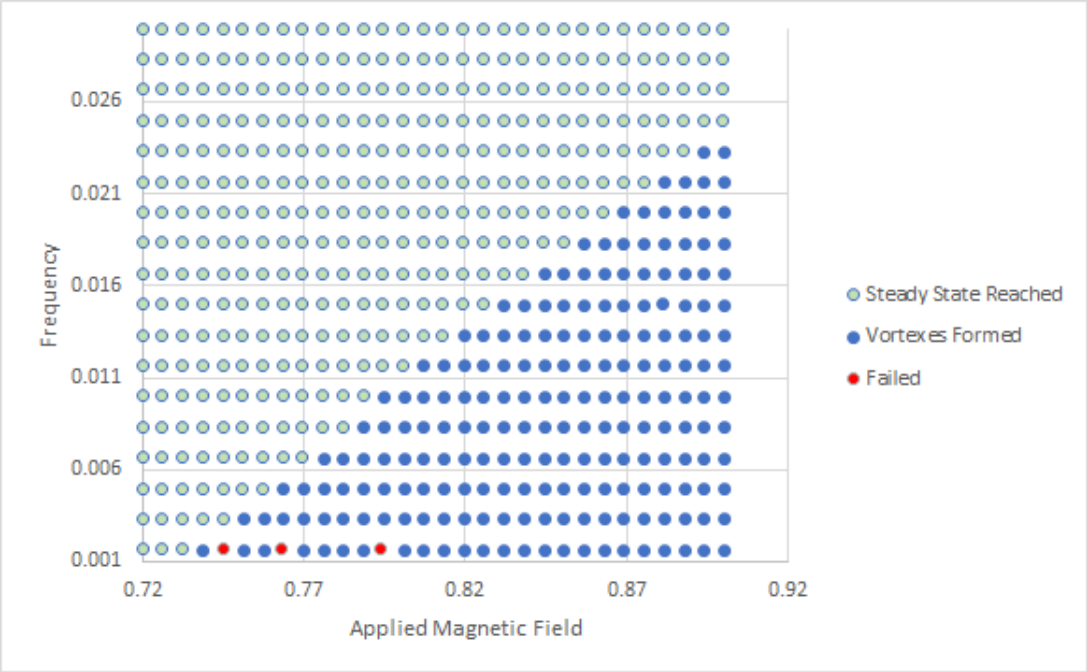

Figure 4.7 A comparison of whether or not the order parameter reaches zero for a given applied field and frequency. Theoretically if the time it takes for the applied field to oscillate is much shorter than the time for a vortex to nucleate than raising the frequency of the applied field could prevent vortex nucleation. White dots indicate that for a given applied field and frequency the order parameter never reaches zero, indicating vortices never form. Blue dots indicate the order parameter does reach zero, meaning vortices formed or there is quenching. The red dots indicate simulations that failed to run correctly. As the frequency increases the applied magnetic field must increase before the order parameter reaches zero.

dots indicate the opposite. We can see that as the frequency increases the required magnetic field for the order parameter to drop to zero also increases. Red dots indicate simulations that did not correctly run. As a reminder H_{sh} has units of $\sqrt{2}H_c$.

4.5 Temperature Waves

Simulations in this section were run by Aiden Harbick.

Before cooling, SRF cavities contain magnetic flux from outside sources such as the earth's

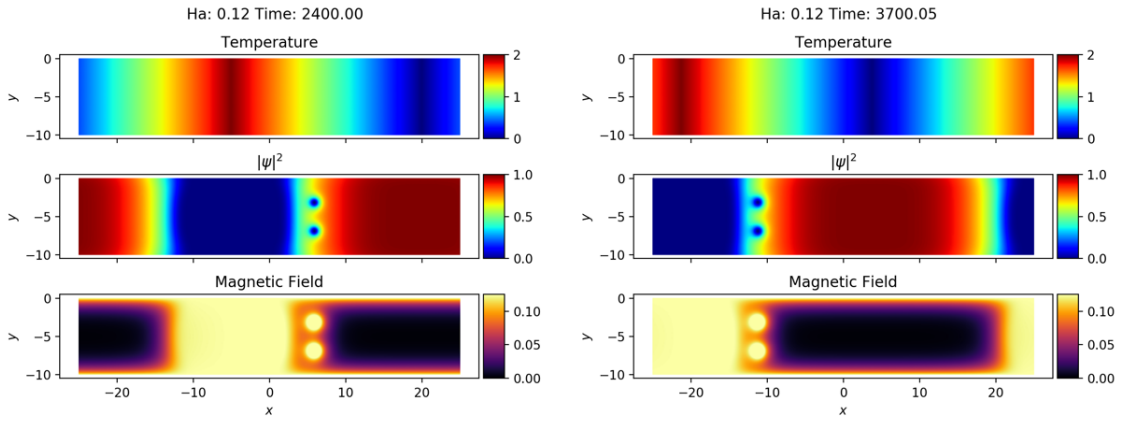

Figure 4.8 Plot of the temperature profile, order parameter, and magnetic field in a superconducting film as the temperature profile moves left to right. We enforce a fixed magnetic field on the top and bottom and periodic boundary condition on the left and right. The temperature profile is designed so that it is large in the middle and drops to zero towards the left and right edge. The region where the temperature is high is nonsuperconducting with zero order parameter and large magnetic field. Vortices form where the temperature is not too high but not too low. As the temperature profile moves left to right, vortices to the right of the temperature peak are pushed along. This simulates how vortices could be expelled from SRF cavities during cooling.

magnetic field. After cooling, the Meissner effect pushes out most of the magnetic flux. Variations in the cooling process can change how much flux remains trapped [58].

With the new capability to vary temperature over time we explore how temperature waves influence the movement of magnetic vortices. We use the film geometry. Our simulations start in a purely superconducting state. We then switch on a spatially periodic temperature gradient and a magnetic field. Once the system has reached a steady state, we move the temperature gradient from right to left. We also introduce defects and observe when vortices get pinned despite the moving temperature wave.

In figure 4.8 we see a temperature wave moving to the left. Where the temperature is high the order parameter is zero and there is a large magnetic field. Where temperature is low the order parameter approaches one and the magnetic field is expelled. As the temperature wave moves left to right two vortices are pushed along with it.

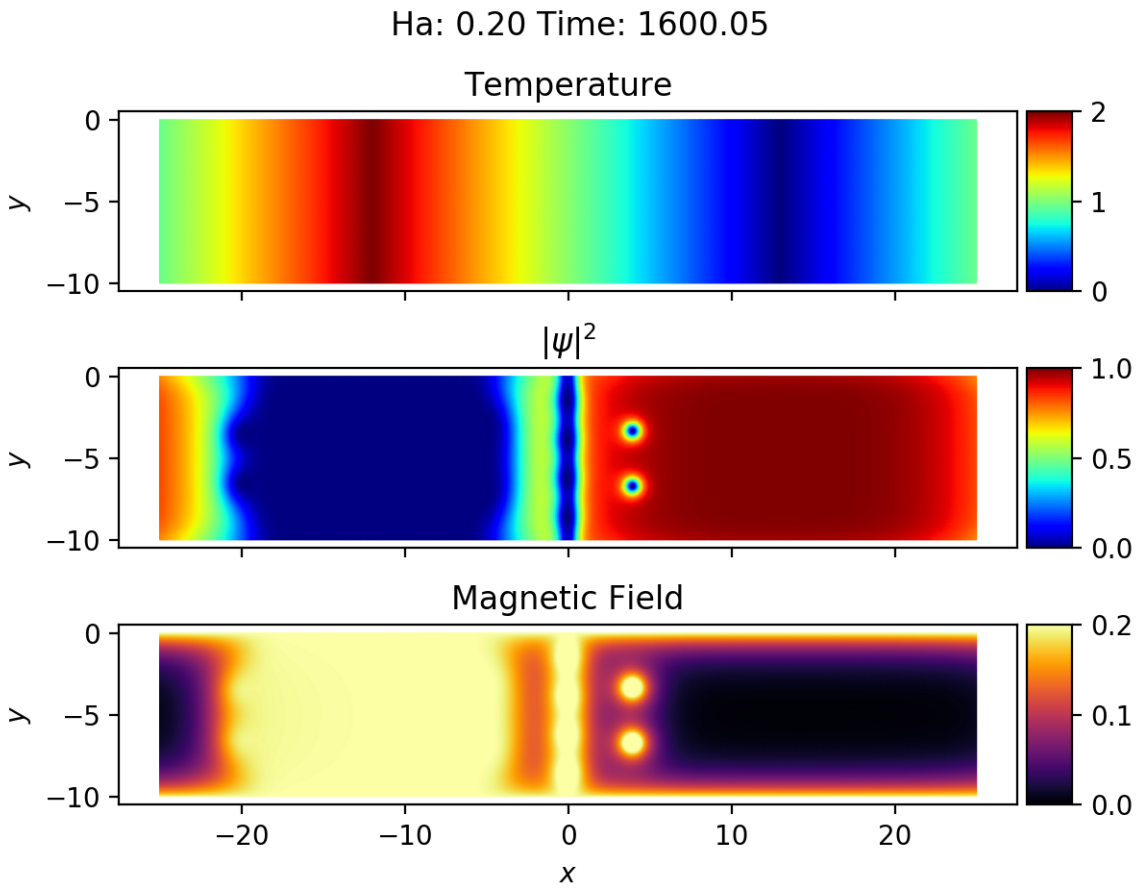

Figure 4.9 Plot showing how a vertical grain boundary at $x = 0$ prevents vortices from moving with the temperature wave. This is due to the vortices inside the grain boundary repelling the vortices inside the wave.

We simulate how defects affect the movement of vortices during cooling. We add a grain boundary right in the path of the heat wave. In figure 4.9 we see two vortices on the right of the grain boundary. They are unable to follow the temperature wave as vortices in the grain boundary repel them.

4.6 Conclusion

Generalizing our method to include material-specific parameters enables us to simulate a wide variety of phenomena of interest to the CBB. Our simulations of islands of deficient Sn showed they are only detrimental if close to the surface. The AC simulations demonstrate that the frequency of the applied AC magnetic fields changes H_{sh}. Finally we've shown how vortices can get trapped by grain boundaries during the process of cooling.

Working with undergraduate students we were able to produce many more simulations than we could have between Mark and I. We expect at least one publication from these results. We hope this software will continue as a powerful tool for enable undergraduate students in performing valuable research.

Chapter 5

Evaluating H_{sh} Directly From Free Energies

5.1 Motivation

As mentioned in chapter 1, the equations of motion and stability for GL and Eilenberger theory are computed as first and second variations of a free energy. There are two reasons to evaluate these variations computationally. The first is that varying parameters on terms with spatial derivatives usually requires a rederivation of the first variation. We avoid this by computationally evaluating the extrema.

The second reason is to abstract away complicated details in Eilenberger theory. GL theory assumes that the system has temperatures close to T_c. This is a major limitation as many applications, including SRF cavities, operate at low temperatures far from T_c. To obtain qualitatively correct values for H_{sh} at low temperatures we must use Eilenberger theory.

Eilenberger theory also has the ability to include information about the Fermi surface. With high-throughput screening and density functional calculations one could find new superconducting materials with large H_{sh}.

5.2 Introduction

For GL theory we define the free energy $\Omega(\mathbf{A},\Delta)$ to be a functional of the magnetic vector potential $\mathbf{A}$ and the complex order parameter Δ. In Eilenberger theory the free energy depends on $\mathbf{A}$, Δ, and several Green's functions f, $\bar{f}$, and g. We write the first variation as $\delta\Omega$ and the second variation as $\delta^2\Omega$.

For GL theory the variations are fairly straightforward [12, 15, 46]. Eilenberger theory is much more complicated with dependencies on the Fermi surface, Matsubara frequencies, and Green's functions [8, 36, 38]. We abstract away the details of the first and second variations by evaluating them computationally . Some ways to do this include using a symbolic solver, taking numerical derivatives using finite differences, or automatic differentiation. The challenge of symbolic solvers is that it produces very messy formulas. Transcribing these formulas often introduces human error. The drawback to numerical derivatives is their limited accuracy. Every nested derivative introduces more numerical error. Automatic differentiation avoids the messiness of symbolic solvers and the inaccuracies of numerical derivatives. For this reason we use automatic differentiation whenever we can.

The power of automatic differentiation comes from dual numbers. Dual numbers have the form $a+b\varepsilon$ where a and b are real numbers and ε has the property $\varepsilon^2=0$. Consider the function $f(x)$. Replace x with a dual number to produce $f(x+\varepsilon)=f(x)+2\varepsilon f'(x)$. For example, $x^2\to(x+\varepsilon)^2=x^2+\varepsilon x$. Any terms with coefficients ε contribute to the first derivative with respect to x. The details in how to implement this on a computer can be found elsewhere. (See [59].)

We have written our code in Julia and unfortunately some basic libraries are not compatible with dual numbers. For example, the tools we use for inverting matrices and calculating eigenvalues are incompatible. When we need to take derivatives of functions that contain these processes we use finite difference methods. Nonetheless, automatic differentiation is a vital tool for maintaining accuracy and speed.

An added benefit to using computational methods to evaluate variations in GL theory is the ability to include spatial dependence in parameters on terms with spatial derivatives. We are specifically interested in the effective mass. The effective mass is related to the mean free path [63]. Changing the mean free path in the surface of an SRF cavity may be a way to raise H_{sh} [64]. In chapter 4 we added spatial dependence to all the material parameters in GL theory *except* the effective mass. This was due to the added complication of the effective mass altering boundary conditions and the equations of motion. This is automatically taken care of when we evaluate the variations computationally.

This chapter is organized as follows. In section 5.3 we describe the slab geometry and boundary conditions of the superconductor. We also discuss the general steps for evaluating the equations of motion and stability using automatic differentiation. In section 5.4 we describe how this is done in GL theory. In section 5.5 we show that we can match previous calculations of H_{sh} and k_c in GL theory. We also show how we can easily include the effective mass and discuss implications for new SRF cavity materials. In section 5.6 we apply our method to Eilenberger theory. We describe how the Eilenberger equations relate $\mathbf{A}$ and Δ to the Green's functions. We linearize the Eilenberger equations as an approximate solution for small applied fields. We explain how solving the Eilenberger equations leads to a simplification of the free energy. Finally, we describe the sensitivity equations and how to use them to evaluate the second variation. In section 5.7 we present our results for Eilenberger theory. In section 5.8 we conclude the chapter.

5.3 General Problem Set Up

Though the specific details of GL and Eilenberger theory differ the overall process of solving for the first and second variations is very similar. This section describes the steps that both methods share as an outline for the sections that follow. In this process we define a geometry and boundary

conditions, discretize the functions of interest, and describe how to take variations with respect to the degrees of freedom. This allows us to evaluate the equations of motion and the stability of the system.

We consider a superconducting slab. Half of space is filled with a superconducting material and the other half is vacuum. We apply a magnetic field along the surface of the superconductor and assume there are not any variations along the direction the magnetic field points. By symmetry the order parameter and magnetic vector potential only vary with the depth into the superconductor [15]. For the Meissner state deep in the superconductor $\mathbf{A} \to 0$ and $\Delta \to \Delta_0$ (to be defined later). Though the exact details of the boundary conditions (BCs) at the superconductor/vacuum interface may vary depending on the theory of interest, they typically involve assuming a fixed applied field $\nabla \times \mathbf{A} \propto H_a$ and zero current leaking into vacuum. The second assumption often leads to $\hat{n} \cdot \nabla \Delta = 0$ at the interface [46]. In Eilenberger theory there are more boundary conditions defining how the Green's functions behave.

As we need to be able to enforce Dirchlet and Neumann BCs we choose to discretize $\mathbf{A}$ and Δ using piecewise cubic Hermite interpolating polynomials (PCHIPs) [60]. Notationally we write this as $A(x) \to \sum_i A_i \phi_i(x)$, $\Delta(x) \to \sum_i \Delta_i \phi_i(x)$ where ϕ_i are the basis functions and A_i, Δ_i are the degrees of freedom (DOFs). (In the future we will assume repeated indices are summed.) The domain is divided into segments. The endpoints of each segment are locations where we solve for the DOFs (function values and their derivatives). The basis functions interpolate between endpoints. The advantage of PCHIPs is they maintain continuity up to the second derivative of the function being interpolated. We apply BCs by directly forcing the respective DOFs to fixed values. For ease of notation we will define $\psi(x) = \psi_i \phi_i(x)$ to represent either A or Δ. This notation holds for all of the following sections. In Eilenberger theory we represent the Green's functions as $\eta(x) = \eta_i \phi_i(x)$.

For many terms in the free energy we can evaluate the spatial integration beforehand as follows

$$\int \psi(x)^2 dx = \psi_i \int \phi_i(x) \phi_j(x) dx \psi_j = \psi_i M_{ij} \psi_j. \tag{5.1}$$

Precompiling these matrices greatly speeds up calculations. Our discretized free energy is now a function of the DOFs, $\Omega(\psi_i)$.

The next step is to solve for the equations of motion. We want to find for what DOFs $\delta\Omega(\psi_i) = d\psi_i \frac{d\Omega}{d\psi_i} = 0$. We do this using dual numbers [61] by replacing each ψ_i with $\psi_i + \varepsilon\delta\psi_i$ where $\varepsilon^2 = 0$. Expanding Ω we get,

$$\Omega(\psi_i + \varepsilon\delta\psi_i) = \Omega(\psi_i) + \varepsilon\delta\psi_i \frac{d\Omega(\psi_i)}{d\psi_i}. \tag{5.2}$$

All terms that are first order in ε contribute to the first variation. The second variation can be taken by setting $\psi_i \to \psi_i + \varepsilon\delta\psi_i + \varepsilon'\delta\psi_i'$ and keeping terms of order $\varepsilon\varepsilon'$. In the future I will assume εs are implicitly included with each $\delta\psi_i$.

Setting the first variation to zero for general $\delta\psi_i$ is equivalent to finding for what values of ψ_i the quantity $\frac{d\Omega(\psi_i)}{d\psi_i} = 0$. This is a multidimensional root finding problem. We use a Levenberg-Marquardt algorithm to solve for what ψ_i we get $\frac{d\Omega(\psi_i)}{d\psi_i} = 0$ [62].

Having solved the first variation we now want to know if our solution is stable. We evaluate the stability of our system by considering the second variation,

$$\delta^2\Omega(\psi_i) = \delta\psi_i \frac{\delta^2\Omega}{\delta\psi_i\delta\psi_j}\delta\psi_j. \tag{5.3}$$

This is the Hessian. Note that in the first variation we never actually evaluate what $\delta\psi$ are. We know that $\delta\psi$ are small but we don't know what sort of spatial dependence they have. The exact form of $\frac{\delta^2\Omega}{\delta\psi_i\delta\psi_j}$ depends on assumptions we make about $\delta\psi$. In general $\delta\psi$ depends on spatial directions other than depth into the superconductor [15]. By expanding $\delta\psi$ as a Fourier series, the smallest eigenvalue changes with the wavenumber k. The system may be stable for some values of k but not others.

We can think of the second variation as a matrix equation. The stability is determined by the minimum eigenvalue of $\frac{\delta^2\Omega}{\delta\psi_i\delta\psi_j}$. If this eigenvalue is positive then the system is stable. If it is negative then the system is unstable. The eigenvectors corresponding to the negative eigenvalues

are the combination of DOFs that lead to the system's transition to another state (vortex state, nonsuperconducting state). Varying k one can then find the smallest applied field where the minimum eigenvalue first crosses zero. This occurs at H_{sh} and the critical wavenumber k_c.

A rough sketch of the process is described below.

1. Define $\Omega(\psi_i)|_{k=0} = \Omega_0$
2. Use dual numbers to evaluate $\delta\Omega_0$.
3. Have solver adjust DOFs to find $\delta\Omega_0 = 0$.
4. Use this as input into $\Omega(\psi_i)|_{k\neq 0} = \Omega_k$.
5. Use dual numbers to evaluate $\delta^2\Omega_k$.
6. Evaluate minimum eigenvalue of $\delta^2\Omega_k$.
7. Adjust H_a and k until H_a is smallest value that has an eigenvalue slightly above zero.

5.4 Ginzburg-Landau Problem set up

With the general problem set up we next consider how this works for GL theory. Assume the vacuum/superconductor interface occurs at the $x = 0$ plane and the magnetic field points in the $\hat{z}$ direction. The nondimensionalized GL free energy is defined as

$$\Omega[\Delta, \mathbf{A}] = \int_{x>0} d^3r\left(\xi^2(\nabla\Delta)^2 + \frac{1}{2}(1-\Delta^2)^2 + \Delta^2\mathbf{A}^2 + (\mathbf{H_a} - \lambda\nabla\times\mathbf{A})^2\right), \tag{5.4}$$

where Δ is the order parameter, $\mathbf{A}$ is the magnetic vector potential, $\mathbf{H_a}$ is the applied magnetic field, ξ is the coherence length, and λ is the penetration depth [12]. We have chosen a gauge such that the order parameter is real. Both Δ and $\mathbf{A}$ depend only on x [15]. Assuming $\mathbf{H_a} = H_a\hat{z}$ we can reduce $\mathbf{A} = A_y(x)\hat{y}$.

We discretize our functions using PCHIPs on a domain from $x = 0$ to $x = L$. The free energy becomes,

$$\Omega(\Delta_i, A_{yi}) = \xi^2 \Delta_i \Delta_j D_{2ij} + \frac{1}{2}(L - 2 * \Delta_i \Delta_j M_{2ij} + \Delta_i \Delta_j \Delta_k \Delta_l M_{4ijkl}) \tag{5.5}$$

$$+ \Delta_i \Delta_j A_{yk} A_{yl} M_{4ijkl} + H_a^2 L - 2\lambda H_a A_{yi} D_i + \lambda^2 A_{yi} A_{yj} D_{2ij} \tag{5.6}$$

where

$$M_{2ij} = \int_{x>0} d^3 r \phi_i(x) \phi_j(x) \tag{5.7}$$

$$M_{4ijkl} = \int_{x>0} d^3 r \phi_i(x) \phi_j(x) \phi_k(x) \phi_l(x) \tag{5.8}$$

$$D_i = \int_{x>0} d^3 r \frac{d\phi_i(x)}{dx} \tag{5.9}$$

$$D_{2ij} = \int_{x>0} d^3 r \frac{d\phi_i(x)}{dx} \frac{d\phi_j(x)}{dx}. \tag{5.10}$$

$$\tag{5.11}$$

The second variation involves an operator discretized as a matrix acting on $\delta\psi$ [12]. By symmetry $\delta\psi$ doesn't depend on z [15]. The y dependence of $\delta\psi$ can be written as a Fourier expansion where $\delta\psi = \delta\psi_c(x)\cos(ky) + \delta\psi_s(x)\sin(ky)$. In particular $\delta\Delta = \delta\Delta_c(x)\cos(ky) + \delta\Delta_s(x)\sin(ky)$ and $\delta\mathbf{A} = \hat{y}(\delta A_{yc}(x)\cos(ky) + \delta A_{ys}(x)\sin(ky)) + \hat{z}(\delta A_{zc}(x)\cos(ky) + \delta A_{zs}(x)\sin(ky))$. Reinserting $\psi \to \psi + \delta\psi$ into the free energy these terms decouple into two identical groups. This means we only solve for $\delta\Delta_c(x), \delta A_{yc}, \delta A_{zs}$ as $\delta\Delta_c(x) = \delta\Delta_s(x)$ etc. When integrating over y we evaluate the average value of the free energy over 1 period, $\int_0^{\frac{2\pi}{k}} dy f(ky) \frac{k}{2\pi}$. Having Ω_k the next step is to use our algorithm to solve the first variation and evaluate the stability using the second variation.

5.5 Ginzburg-Landau Results

5.5.1 Matching

Our primary objective in using automatic differentiation with GL theory is to show how well our calculations match previous work. Though our methodologies differ, the geometry, boundary conditions, and fundamental theory are identical to a different article [12]. By reproducing calculations of H_{sh} and k_c evaluated previously, we show our method is accurate. In figure 5.1 we compare the estimated values of H_{sh} from our new method (red stars) to the previous values (blue line). Note that we match very well for a range of values of κ.

Similarly in figure 5.2 our values for k_c line up well with previous calculations. We hypothesize the deviation at higher values of κ is due to the need to refine grid spacing for larger κ.

5.5.2 Spatially Varying Effective Mass

Our secondary objective in using automatic differentiation is to explore how spatially varying mass influences H_{sh}. As mentioned in chapter 4, generalizing parameters on terms with spatial derivatives can lead to changes in the equations of motion and boundary conditions. One benefit of the methods in this chapter is the ability to solve the equations of motion without working out the details of the first variation. We can add spatial variations to any parameters without altering the algorithm. This allows us to include a spatially varying effective mass.

We nondimensionalize the GL free energy so that the parameter $m(r)$ represents deviations away from the bulk value of the effective mass. We define $m(r)$ to be some value m_0 on the surface and have $m(r)$ linearly approach one at some x_0 as shown in figure 5.3. In figure 5.4 we calculate the ratio of H_{sh} with varying effective mass to H_{sh} with an effective mass of 1. As the ratio of the new effective mass over the old effective mass increases H_{sh} increases. This suggests that if accelerator scientists could recreate this effective mass profile then theoretically they could reach

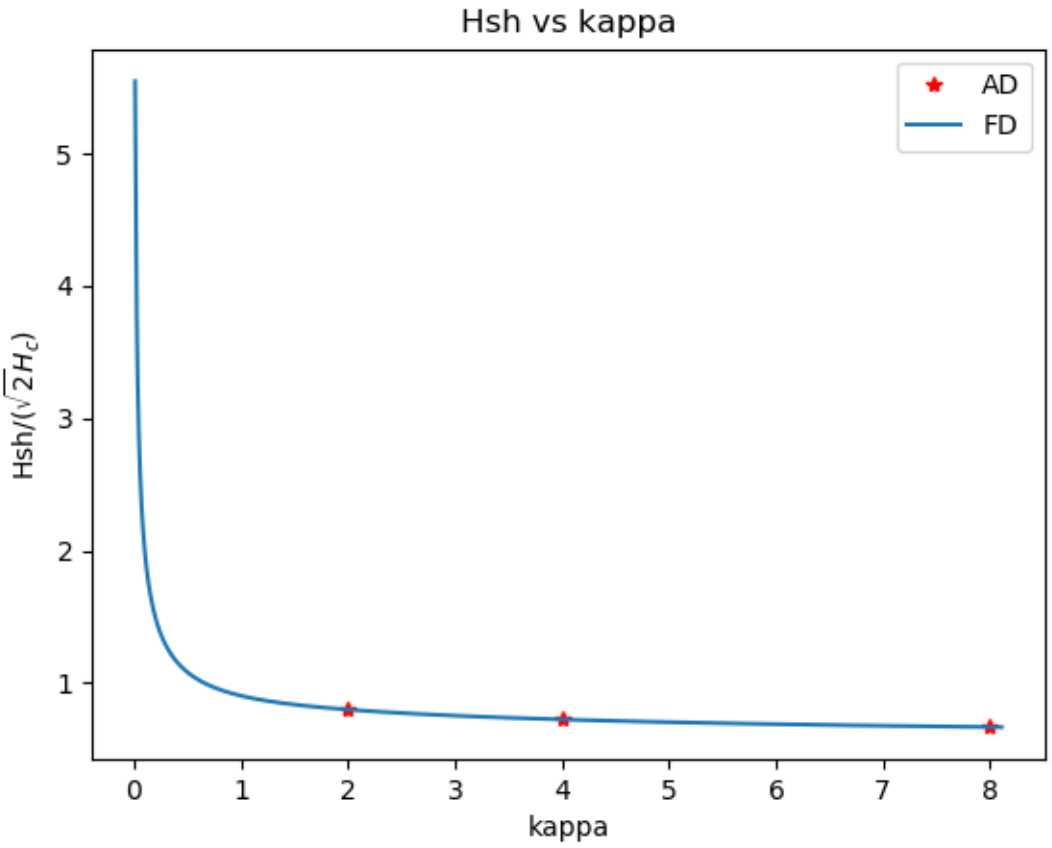

Figure 5.1 Comparison of calculated values of H_{sh} directly solving the equations of motion and stability conditions (blue line) vs. values evaluated using automatic differentiation (red stars). The new results match the old results very nicely. We only compared a few values before moving on to Eilenberger theory.

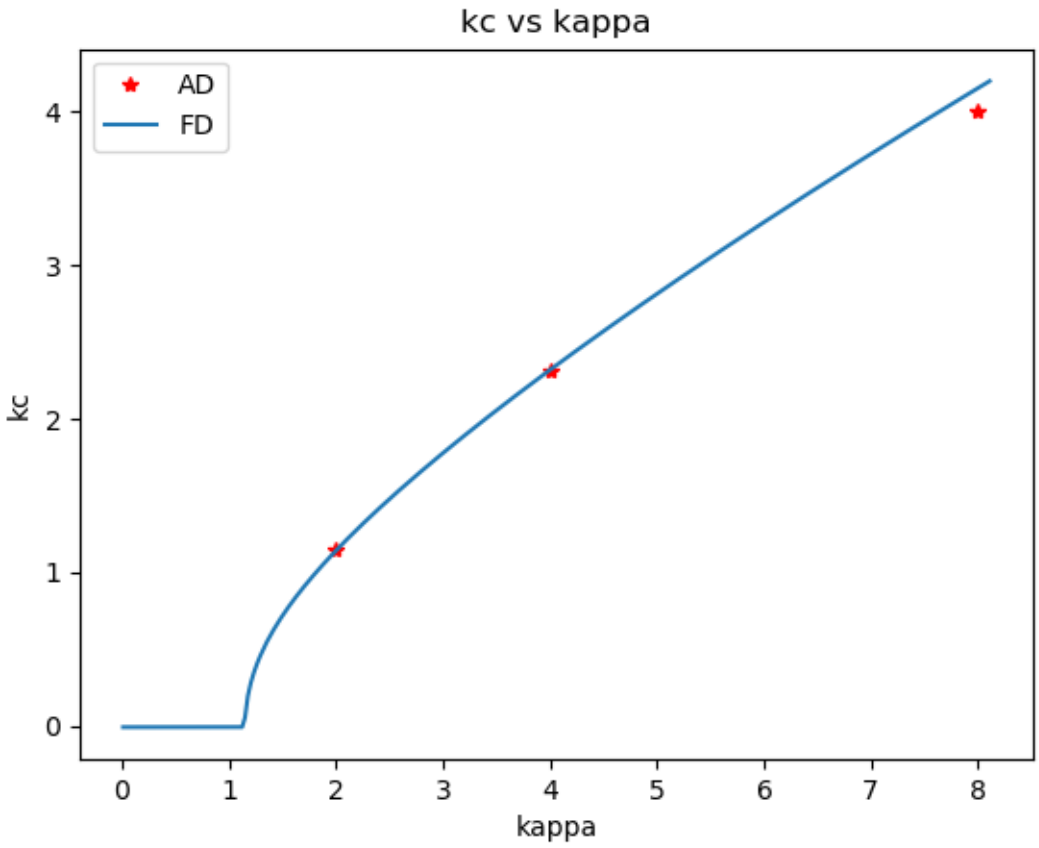

Figure 5.2 Comparison of previously calculated values of k_c (blue line) vs. values evaluated using automatic differentiation (red stars). The new results don't match the old as well as H_{sh} possibly due to the need for finer grid spacing for larger κ.

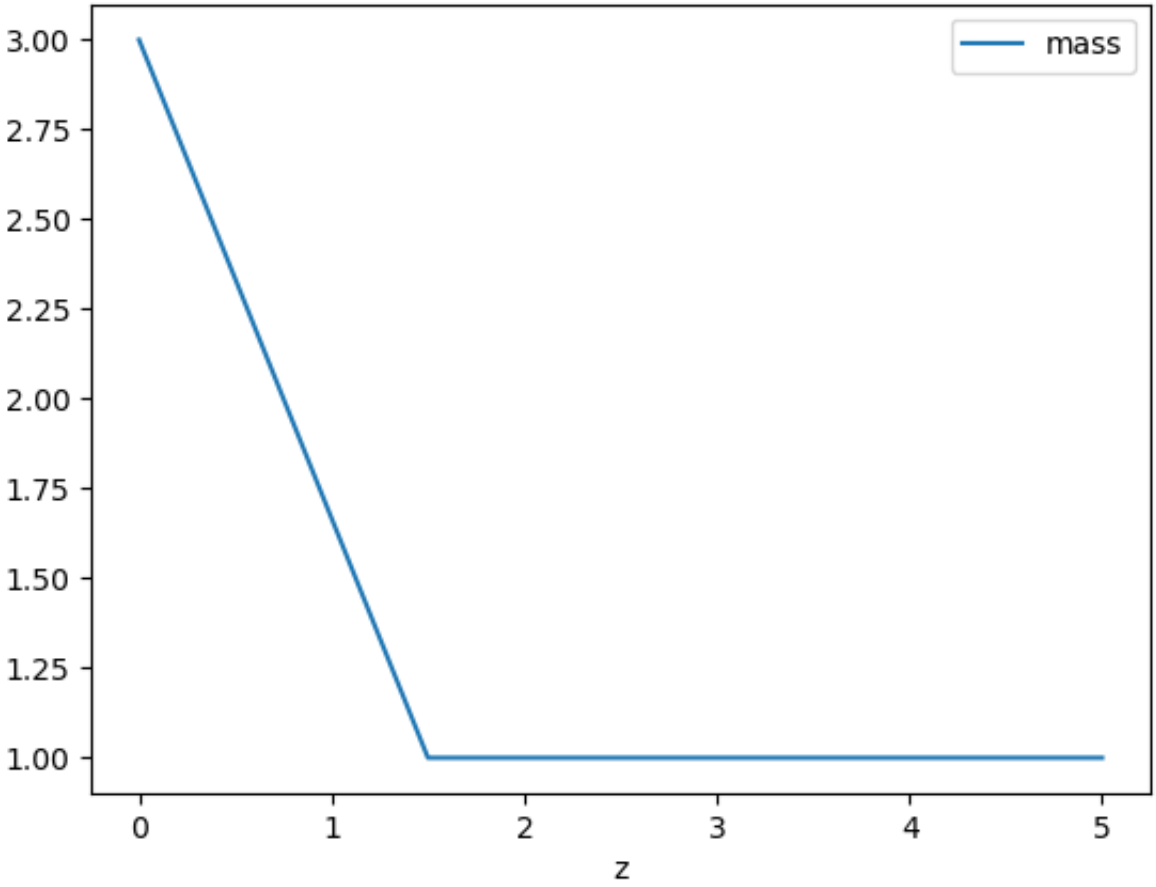

Figure 5.3 Plot of the ratio of the new effective mass over the effective mass for the bulk material. We simulate a superconductor/vacuum interface at $z = 0$. Theoretically the surface of a superconductor could be doped with impurities to raise the effective mass. Deep inside the superconductor the ratio of the effective masses approach one.

higher magnetic fields.

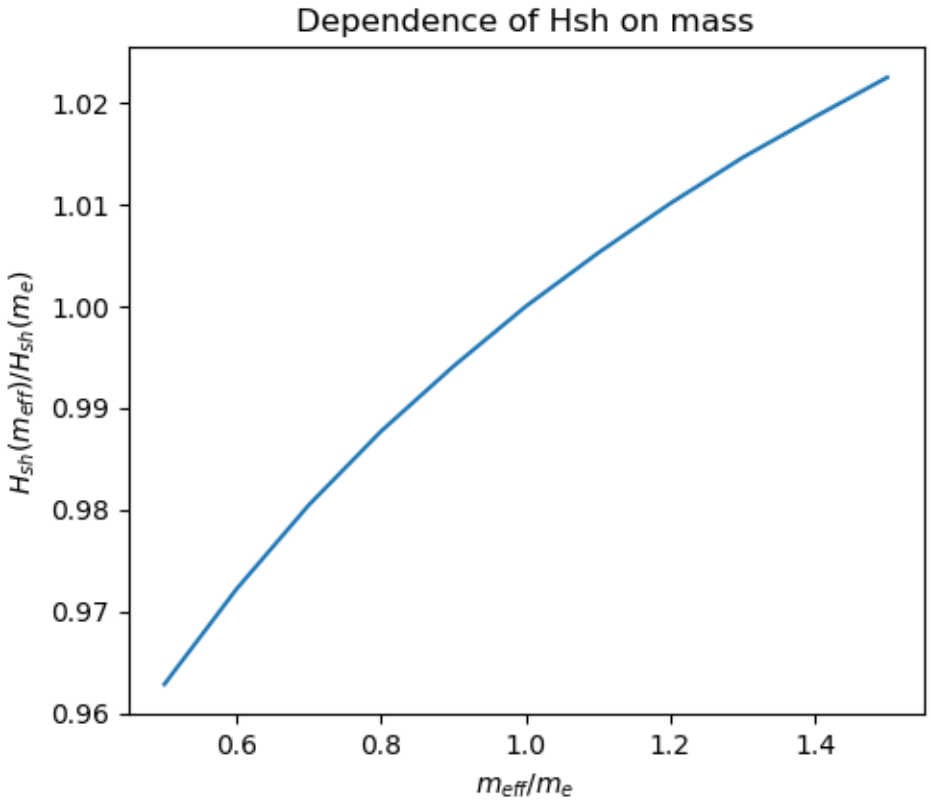

Figure 5.4 Plot of H_{sh} dependence on varying effective mass. m_e is the base mass value and m_{eff} is the new effective mass. The ratio $\frac{H_{sh}(m_{\text{eff}})}{H_{sh}(m_e)}$ increases as m_{eff} increases. This suggests that a doped surface layer that increases the effective mass could be used to raise H_{sh}.

5.6 Eilenberger Problem set up

5.6.1 Free Energy

The Eilenberger free energy is fairly complicated [36]. Written out it is,

$$\Omega = \nu \int d^3r \left\{ \frac{\kappa_0^2}{3}[\mathbf{H}-\mathbf{H}_a]^2 + |\Delta|^2 \log\left(\frac{T}{T_c}\right) \right. \tag{5.12}$$

$$+ \int (dn) \left[\frac{|\Delta|^2}{\omega_n} - \Delta^\dagger f - \bar{f}\Delta - 2\omega_n(g-1) \right. \tag{5.13}$$

$$\left. \left. -g\mathbf{n}\left(\nabla \log \frac{f}{\bar{f}} - 2i\mathbf{A}\right)\right]\right\}. \tag{5.14}$$

We have the order parameter Δ, magnetic vector potential $\mathbf{A}$, applied magnetic field $\mathbf{H_a}$ and interior field $\mathbf{H} = \nabla \times \mathbf{A}$. Unlike Ginzburg-Landau theory we can now include dependence on the temperature T. Several physical constants include the critical temperature T_c, the density of states at the Fermi energy ν, and the analogous Ginzburg-Landau parameter at zero temperature κ_0. We have a dependence on several Green's functions f, $\bar{f}$ and g. These are functions of Δ and $\mathbf{A}$. The way they relate to each other is determined by the first variation. The quantities $\omega_n = 2\pi T(n+\frac{1}{2})$ are the Matsubara frequencies. The outer integral is evaluated for all space and the second integral is shorthand for $\int (dn) = 2\pi T \sum_n \int \rho(n) d\mathbf{n}$ where n goes from 0 to ∞ and $d\mathbf{n} = sin(\theta) d\theta d\phi$. We will assume $\rho(n) = \frac{1}{4\pi}$. We could generalize this to include a dependence on the Fermi surface but this is outside of the current scope. We will also set ν to 1 for convenience.

5.6.2 Geometry

Once again we consider slab geometry. This time we define the slab/vacuum interface to be at the $z = 0$ plane. We assume all quantities depend only on z (except the perturbations $\delta\psi$). The applied field lies in the $\hat{x}$ direction. We assume the magnetic vector potential has the form $A_y(z)\hat{y}$ such that $\nabla \times \mathbf{A} = -A_y' = H_a$ at $z = 0$. Assuming the material is a clean superconductor we can also assume spectral boundary conditions on the Green's functions. This means that

$f(\omega, \mathbf{n}, z=0) = f(\omega, \mathbf{m}, z=0)$ where $\mathbf{m} = \mathbf{n} - 2(\mathbf{n}\cdot\hat{\mathbf{z}})\hat{\mathbf{z}}$. (In other words $m_x = n_x$, $m_y = n_y$, and $m_z = -n_z$.)

5.6.3 First Variation

The first and second variations of Eilenberger theory are a little different from GL theory. The correct extrema of the Eilenberger free energy are not found by taking variations with respect to Δ, $\mathbf{A}$ and the Green's functions simultaneously [8]. Instead, following Eilenberger, we take variations with respect to Δ and $\mathbf{A}$ and set this to zero to derive the self consistent equations. Similarly, we take variations with respect to the Green's functions and set this to zero to derive the Eilenberger equations.

Because of this it is easier to split these functions into two groups. Let ψ be either Δ or $\mathbf{A}$ and let η be any of the Green's functions. Assuming $\frac{\delta\Omega}{\delta\psi} = 0$ and $\frac{\delta\Omega}{\delta\eta} = 0$ we get,

$$\delta\Omega = \delta\psi\frac{\delta\Omega}{\delta\psi} + \delta\eta\frac{\delta\Omega}{\delta\eta} \tag{5.15}$$

$$= \delta\psi 0 + \delta\eta 0 = 0. \tag{5.16}$$

To fit this into our algorithm we directly solve $\frac{\delta\Omega}{\delta\eta} = 0$ for fixed ψ, treating η as a function of ψ. When we discretize the problem we solve for the degrees of freedom ψ_i and η_i.

Solving the Eilenberger equations reduces the number of terms needed in the free energy to solve for ψ. To see why, we split the free energy Ω into 3 parts, $\Omega_1(\psi), \Omega_2(\psi,\eta)$, and $\Omega_3(\eta)$. Let $\Omega' = \Omega_1 + \Omega_2$ and $\Omega'' = \Omega_2 + \Omega_3$. We first solve $\frac{\delta\Omega''}{\delta\eta} = 0$ using the Eilenberger equations. Next we need to solve for $\frac{\delta\Omega'}{\delta\psi} = 0$ using automatic differentiation. As Ω' has no dependence on Ω_3 we can ignore those terms when evaluating the free energy.

This greatly reduces the computational work required to evaluate the free energy. It is impossible to evaluate $\nabla\log(\frac{f}{\bar{f}})$ with precompiled matrices. Thankfully these terms don't contribute to Ω' and so we can ignore them.

When taking the first variation we first calculate η_i from ψ_i. We don't evaluate η_i with $\psi_i + \delta\psi_i$ because those terms get eliminated in the Eilenberger equations. After evaluating η_i we evaluate the free energy terms with $\psi_i + \delta\psi_i$. We numerically solve for when the first variation with respect to ψ_i is zero.

The Eilenberger equations are described in the next section. As a reference we include the self consistent equations below. We never directly solve them except when considering boundary conditions. The self consistent equation for the order parameter and magnetic vector potential are,

$$\Delta \log \frac{T}{T_c} + 2\pi T \sum_n \left[\frac{\Delta}{\omega} - \int d\mathbf{n}\rho(\mathbf{n}) f_n\right] = 0 \tag{5.17}$$

$$\nabla \times \mathbf{H} + \frac{i2\pi T}{\kappa_0^2} \sum_n \int 3g\mathbf{n} \cdot d\mathbf{n} = 0. \tag{5.18}$$

5.6.4 Eilenberger equations

The origin and need to solve the Eilenberger equations is described in the previous section. Here we explain how we solve them. In this section we need to differentiate between $\mathbf{A}$ and Δ as well as between the Green's functions so we drop the ψ and η notation temporarily. We treat the Green's functions as functions of $\mathbf{A}$ and Δ. In general the Eilenberger equations are

$$\{\omega + \mathbf{n} \cdot [\nabla - i\mathbf{A}(\mathbf{r})]\} f(\omega, \mathbf{n}, \mathbf{r}) = \Delta(\mathbf{r}) g(\omega, \mathbf{n}, \mathbf{r}) \tag{5.19}$$

$$\{\omega - \mathbf{n} \cdot [\nabla + i\mathbf{A}(\mathbf{r})]\} \bar{f}(\omega, \mathbf{n}, \mathbf{r}) = \Delta^\dagger(\mathbf{r}) g(\omega, \mathbf{n}, \mathbf{r}) \tag{5.20}$$

$$g^2 + f\bar{f} = 1 \tag{5.21}$$

but for our geometry it reduces to

$$\omega_n f_n + n_z \frac{\partial}{\partial z} f_n - iA_y n_y f_n = \Delta g_n \tag{5.22}$$

$$\omega_n \bar{f}_n - n_z \frac{\partial}{\partial z} \bar{f}_n - iA_y n_y \bar{f}_n = \Delta g_n \tag{5.23}$$

$$2n_z \frac{\partial}{\partial z} g_n = \Delta f_n - \Delta \bar{f}_n \tag{5.24}$$

where we have taken the gradient of the last equation and assumed Δ is real. The subscript n indicates we are considering the n^{th} Matsubara frequency.

Next we need to consider boundary conditions. Spectral boundary conditions at $z = 0$ mean the solutions to these equations are equivalent to the equations made by replacing n_z with $-n_z$ as follows,

$$\omega_n f_n - n_z \frac{\partial}{\partial z} f_n - iA_y n_y f_n = \Delta g_n \tag{5.25}$$

$$\omega_n \bar{f}_n + n_z \frac{\partial}{\partial z} \bar{f}_n - iA_y n_y \bar{f}_n = \Delta g_n \tag{5.26}$$

$$2n_z \frac{\partial}{\partial z} g_n = -\Delta f_n + \Delta \bar{f}_n. \tag{5.27}$$

Note that these new equations could also be made by swapping $f_n \leftrightarrow \bar{f}_n$. This means that at $z = 0$ $f_n = \bar{f}_n$.

To enforce these boundary conditions it's easier to consider $S = f_n + \bar{f}_n$ and $D = f_n - \bar{f}_n$. Taking the sum and difference of the first two Eilenberger equations produces new equations for S and D as follows,

$$\omega S + n_z \frac{\partial}{\partial z} D - iA_y n_y S = 2\Delta g_n \tag{5.28}$$

$$\omega D + n_z \frac{\partial}{\partial z} S - iA_y n_y D = 0 \tag{5.29}$$

$$2n_z \frac{\partial}{\partial z} g_n = \Delta D. \tag{5.30}$$

Enforcing spectral boundary conditions is simply $D(0) = 0$.

The other set of boundary conditions to consider are what happens deep inside the superconductor. Deep inside we assume a purely superconducting state. There are no physical variations here so

we can assume η is smooth and $\mathbf{A} \to 0$. The Eilenberger equations greatly simplify as,

$$\omega f_n = \Delta g_n \tag{5.31}$$

$$\omega \bar{f}_n = \Delta^{\dagger} g_n = \Delta g_n \tag{5.32}$$

$$\implies f_n = \bar{f}_n \tag{5.33}$$

$$g_n^2 + f_n^2 = 1 \tag{5.34}$$

$$\implies g_n = \sqrt{1 - f_n^2} \tag{5.35}$$

$$\implies \omega f_n = \Delta \sqrt{1 - f_n^2} \tag{5.36}$$

$$\implies f_n = \frac{\Delta}{\sqrt{\omega^2 + \Delta^2}}. \tag{5.37}$$

To find Δ we have to consider the self consistent equation, We assume everything is smooth such that $\rho(n) = \frac{1}{4\pi}$ the $\mathbf{n}$ dependence drops and we get

$$\Delta \log \frac{T}{T_c} + 2\pi T \sum_n \left[\frac{\Delta}{\omega} - f_n \right] = 0 \tag{5.38}$$

$$\implies \Delta \log \frac{T}{T_c} + 2\pi T \sum_n \left[\frac{\Delta}{\omega} - \frac{\Delta}{\sqrt{\omega^2 + \Delta^2}} \right] = 0 \tag{5.39}$$

$$\implies \log \frac{T}{T_c} + 2\pi T \sum_n \left[\frac{1}{\omega} - \frac{1}{\sqrt{\omega^2 + \Delta^2}} \right] = 0. \tag{5.40}$$

This is a transcendental equation that tells us how to calculate Δ deep within the superconductor Once Δ is found the other quantities deep in the superconductor are given as,

$$f_n = \frac{\Delta}{\sqrt{\omega^2 + \Delta^2}} \tag{5.41}$$

$$g_n = \frac{\omega}{\sqrt{\omega^2 + \Delta^2}} \tag{5.42}$$

This converts to

$$S = \frac{2\Delta}{\sqrt{\omega^2 + \Delta^2}} \tag{5.43}$$

$$D = 0 \tag{5.44}$$

$$g_n = \frac{\omega}{\sqrt{\omega^2 + \Delta^2}} \tag{5.45}$$

Similar to the GL case we discretize this by assuming $\psi = \psi_i \phi_i(z)$, $\eta_i \phi_i(z)$ where $\phi_i(z)$ are PCHIPs. We project the Eilenberger equations onto the $\phi_i(z)$ basis. This turns the Eilenberger equations into a matrix equation.

$$\begin{pmatrix} n_z DM_{ij} & \omega M_{ij} - i n_y A M_{ij} & 0 \\ \omega M_{ij} - i n_y A_{ij} & n_z DM_{ij} & -2\Delta M_{ij} \\ 0 & -\Delta M_{ij} & 2 n_z DM_{ij} \end{pmatrix} \cdot \begin{pmatrix} S_j \\ D_j \\ g_j \end{pmatrix} = \mathbf{0}$$

where

$$M_{ij} = \int_{z>0} d^3 r \phi_i(z) \phi_j(z) \tag{5.46}$$

$$DM_{ij} = \int_{z>0} d^3 r \phi_i(z) \frac{d\phi_j(z)}{dz} \tag{5.47}$$

$$A_{ij} = \int_{z>0} d^3 r \phi_i(z) \phi_j(z) \phi_k(z) A_{yk} \tag{5.48}$$

$$\Delta M_{ij} = \int_{z>0} d^3 r \phi_i(z) \phi_j(z) \phi_k(z) \Delta_k. \tag{5.49}$$

We enforce boundary conditions by removing DOFs that we know from the left hand side of this equation and subtracting them on the right hand side. Given $\mathbf{A}$ and Δ we solve this matrix equation to find f, $\bar{f}$, g. This is required before we can take the computational variations with respect to $\mathbf{A}$ and Δ. (See subsection 5.6.3).

5.6.5 Integrating Over the Fermi Sphere

The previous subsection showed how to calculate η for a given Matsubara frequency and a single point on the Fermi surface. (Once again η is a substitute for f, $\bar{f}$, and g). The free energy depends on an infinite sum of Matsubara frequencies and the entire Fermi surface. The sum over Matsubara frequencies can be truncated for large n. The next step is to discretize the integral over the Fermi surface.

Consider the integral $\int \eta(\theta,\phi)\sin(\theta)d\theta d\phi$. We discretize this integration following ref. [65]. The author breaks the integral up into a sum,

$$\int \eta(\theta,\phi)\sin(\theta)d\theta d\phi = \frac{\pi}{m}\sum_{j=1}^{2m}\sum_{i=1}^{m} w_i \eta(\theta_i,\phi_j) \tag{5.50}$$

where θ_i are chosen such that $\cos(\theta_i)$ are the points and w_i are the weights of a Gauss-Legendre quadrature. In general this sum considers the entire Fermi sphere.

Thankfully our system exhibits lots of symmetries that reduce the integration over the whole Fermi sphere to a single octant. We've already seen that $n_z \leftrightarrow -n_z$ is equivalent to $f_n \leftrightarrow \bar{f}_n$ leading to $f_n(n_z) = \bar{f}_n(-n_z)$. One can also show that $n_y \leftrightarrow -n_y$ is equivalent to $\eta \leftrightarrow \eta^*$ where the star indicates the complex conjugate. There is no dependence on n_x so $n_x \leftrightarrow -n_x$ means $\eta(n_x) = \eta(-n_x)$. Table 5.1 shows how η gets mapped between octants and also shows convenient combinations of Green's functions that often lead to cancellations in the free energy.

5.6.6 Linearized Equations

We check the accuracy of our evaluated η by considering the linearized Eilenberger equations. This holds if we consider a very small applied field. Assume all quantities in the purely superconducting state are perturbed by a small amount, $\Delta \to \Delta_0 + \delta\Delta(z)$, $\mathbf{A} \to \delta\mathbf{A}$, $f \to f_0 + \delta f(z)$, etc. Any products of δ quantities can be ignored as too small. This simplifies the Eilenberger equations and

$\theta\backslash\phi$	$0-\frac{\pi}{2}$	$\frac{\pi}{2}-\pi$	$\pi-\frac{3\pi}{2}$	$\frac{3\pi}{2}-2\pi$
$0-\frac{\pi}{2}$	$n_z, n_y, f, \bar{f}, g$ $-\Delta f - \Delta\bar{f}$ $-gn_z\frac{\nabla f}{f} + gn_z\frac{\nabla\bar{f}}{\bar{f}}$ $2ign_yA_y$	$n_z, n_y, f, \bar{f}, g$ $-\Delta f - \Delta\bar{f}$ $-gn_z\frac{\nabla f}{f} + gn_z\frac{\nabla\bar{f}}{\bar{f}}$ $2ign_yA_y$	$n_z, -n_y, f^*, \bar{f}^*, g^*$ $-\Delta f^* - \Delta\bar{f}^*$ $-g^*n_z\frac{\nabla f^*}{f^*} + g^*n_z\frac{\nabla\bar{f}^*}{\bar{f}^*}$ $-2ig^*n_yA_y$	$n_z, -n_y, f^*, \bar{f}^*, g^*$ $-\Delta f^* - \Delta\bar{f}^*$ $-g^*n_z\frac{\nabla f^*}{f^*} + g^*n_z\frac{\nabla\bar{f}^*}{\bar{f}^*}$ $-2ig^*n_yA_y$
$\frac{\pi}{2}-\pi$	$-n_z, n_y, \bar{f}, f, g$ $-\Delta\bar{f} - \Delta f$ $gn_z\frac{\nabla\bar{f}}{\bar{f}} - gn_z\frac{\nabla f}{f}$ $2ign_yA_y$	$-n_z, n_y, \bar{f}, f, g$ $-\Delta\bar{f} - \Delta f$ $gn_z\frac{\nabla\bar{f}}{\bar{f}} - gn_z\frac{\nabla f}{f}$ $2ign_yA_y$	$-n_z, -n_y, \bar{f}^*, f^*, g^*$ $-\Delta\bar{f}^* - \Delta f^*$ $g^*n_z\frac{\nabla\bar{f}^*}{\bar{f}^*} - g^*n_z\frac{\nabla f^*}{f^*}$ $-2ig^*n_yA_y$	$-n_z, -n_y, \bar{f}^*, f^*, g^*$ $-\Delta\bar{f}^* - \Delta f^*$ $g^*n_z\frac{\nabla\bar{f}^*}{\bar{f}^*} - g^*n_z\frac{\nabla f^*}{f^*}$ $-2ig^*n_yA_y$

Table 5.1 Table showing how the Eilenberger Green's functions get mapped over the octants of the Fermi surface. These Green's functions are found by solving the Eilenberger equations. Assuming a slab geometry and a clean superconductor the Eilenberger equations exhibit many symmetries. These symmetries allow us to reduce the number of octants we integrate over by up to a factor of 8.

self consistent equations as shown below,

$$\omega f_0 + \omega\delta f + n_z\nabla\delta f - in_y\delta A f_0 = \delta\Delta g_0 + \Delta_0\delta g + \Delta_0 g_0 \tag{5.51}$$

$$\implies \omega\delta f + n_z\nabla\delta f - in_y\delta A f_0 = \delta\Delta g_0 + \Delta_0\delta g \tag{5.52}$$

$$\omega\bar{f}_0 + \omega\delta\bar{f} - n_z\nabla\delta\bar{f} - in_y\delta A\bar{f}_0 = \delta\Delta g_0 + \Delta_0\delta g + \Delta_0 g_0 \tag{5.53}$$

$$\implies \omega\delta\bar{f} - n_z\nabla\delta\bar{f} - in_y\delta A\bar{f}_0 = \delta\Delta g_0 + \Delta_0\delta g \tag{5.54}$$

$$2nz\nabla\delta g = \Delta_0(f_0 + \delta f - \bar{f}_0 - \delta\bar{f}) + \delta\Delta(f_0 - \bar{f}_0) \tag{5.55}$$

$$\implies 2nz\nabla\delta g = \Delta_0(\delta f - \delta\bar{f}) \tag{5.56}$$

$$\delta\Delta\log(\frac{T}{T_c}) + 2\pi T\sum_n(\frac{\delta\Delta}{\omega} - \int dn\frac{1}{4\pi}\delta f) = 0 \tag{5.57}$$

$$-\frac{\kappa_0^2}{3}\delta A'' + 2\pi T\sum_n\int\frac{dn}{4\pi}n_y i\delta g = 0. \tag{5.58}$$

Let's make a further simplifying assumption. Assume we apply a very small magnetic field and assume the magnetic potential vector has the form $A_y = A_0\exp(-z/\lambda)$ where $A_0 = H_a\lambda$. Assume that Δ remains a constant, $\delta\Delta = 0$. Assume that the Green's functions have the form $f = f_{r0} + f_{r1}\exp(-z/\lambda) + if_{i1}\exp(-z/\lambda)$ where f_{r1} and f_{i1} are small numbers such that terms with the product of themselves or A_0 can be ignored. Assume similar arguments for $\bar{f}$ and g. Note that f_{r0} is the value of f as $z\to\infty$. So $f_{r0} = \bar{f}_{r0} = \frac{\Delta}{\omega_n^2+\Delta^2}$, and similarly $g_{r0} = \frac{\omega_n}{\omega_n^2+\Delta^2}$. This means that $\omega_n f_{r0} - \Delta g_{r0} = 0$.

Substituting this into the Eilenberger equations we get six equations for the real and imaginary

parts of η,

$$\omega f_{r1} - n_z f_{r1}/\lambda = \Delta g_{r1} \tag{5.59}$$

$$\omega f_{i1} - n_z f_{i1}/\lambda - n_y A_0 f_{r0} = \Delta g_{i1} \tag{5.60}$$

$$\omega \bar{f}_{r1} + n_z \bar{f}_{r1}/\lambda = \Delta g_{r1} \tag{5.61}$$

$$\omega \bar{f}_{i1} + n_z \bar{f}_{i1}/\lambda - n_y A_0 \bar{f}_{r0} = \Delta g_{i1} \tag{5.62}$$

$$-2n_z g_{r1}/\lambda = \Delta(f_{r1} - \bar{f}_{r1}) \tag{5.63}$$

$$-2n_z g_{i1}/\lambda = \Delta(f_{i1} - \bar{f}_{i1}). \tag{5.64}$$

Solving the six linearized Eilenberger equations we find,

$$f_{r1} = 0 \tag{5.65}$$

$$f_{i1} = \frac{H_a n_y \Delta \lambda^2 (n_z + \lambda\omega)}{\sqrt{\Delta^2+\omega^2}(-n_z^2 + \lambda^2(\Delta^2+\omega^2))} \tag{5.66}$$

$$\bar{f}_{r1} = 0.0 \tag{5.67}$$

$$\bar{f}_{i1} = \frac{H_a n_y \Delta \lambda^2 (-n_z + \lambda\omega)}{\sqrt{\Delta^2+\omega^2}(-n_z^2 + \lambda^2(\Delta^2+\omega^2))} \tag{5.68}$$

$$g_{r1} = 0 \tag{5.69}$$

$$g_{i1} = -\frac{H_a n_y \Delta^2 \lambda^3}{\sqrt{\Delta^2+\omega^2}(-n_z^2 + \lambda^2(\Delta^2+\omega^2))} \tag{5.70}$$

There are two unknowns left, λ and Δ. Both can be found using the self consistent equations. We saw how this worked previously with Δ. For λ we need to consider the self consistent equation for $\mathbf{A}$. Plugging in our simplified $\mathbf{A}$ and g we get,

$$-\frac{\kappa 0}{3}\frac{H_a}{\lambda} - \frac{4\pi T}{m}\sum_{n,i,j} n_{y,i,j} g_{i1,n,i,j} = 0. \tag{5.71}$$

where we have included notation indicating a sum over Matsubara frequencies and angles. We can plug in g_{i1} and solve the transcendental equation to find λ. With λ and δ we have all we need to evaluate our linearized η.

5.6.7 Second variation

Up till now we've described the steps necessary to evaluate the first variation. Now we explain how to solve the second variation. The second variation depends on ψ, η, $\delta\psi$, and $\delta\eta$. We treat $\delta\eta$ as functions of ψ, η, and $\delta\psi$. The equations used to calculated $\delta\eta$ are derived by replacing $\psi \to \psi + \delta\psi$ and $\eta + \delta\eta$ in the Eilenberger equations as given below,

$$(\omega + \mathbf{n}\cdot(\nabla - i\hat{\mathbf{y}}A_y))\,\delta f - \Delta\delta g = if\mathbf{n}\cdot\delta\mathbf{A} + g\delta\Delta \tag{5.72}$$

$$(\omega - \mathbf{n}\cdot(\nabla + i\hat{\mathbf{y}}A_y))\,\delta \bar{f} - \Delta\delta g = i\bar{f}\mathbf{n}\cdot\delta\mathbf{A} + g\delta\Delta \tag{5.73}$$

$$2\mathbf{n}\cdot\nabla\delta g - \Delta\delta f + \Delta\delta\bar{f} = f\delta\Delta - \bar{f}\delta\Delta. \tag{5.74}$$

These are the sensitivity equations and can be solved in a manner similar to the Eilenberger equations. Note that the terms in the right hand side make it so that in general the sensitivities do not share the same symmetries on the Fermi surface as the Eilenberger equations.

Solving the sensitivity equations reduces the terms needed in the free energy to solve for the Hessian. We saw before that solving the Eilenberger equations is the same as setting $\frac{\delta\Omega''}{\delta\eta} = 0$ Similarly solving the sensitivity equations is setting $\delta\frac{\delta\Omega''}{\delta\eta} = \delta\psi\frac{\delta^2\Omega''}{\delta\eta\delta\psi} + \delta\eta\frac{\delta^2\Omega''}{\delta\eta^2} = 0$. If we expand out the whole second variation we get,

$$\delta^2\Omega = \delta^2\Omega' + \delta^2\Omega'' \tag{5.75}$$

$$= \delta^2\Omega' + 0 \tag{5.76}$$

$$= \delta\psi^2\frac{\delta^2\Omega_1}{\delta\psi^2} + \delta\psi\delta\eta\frac{\delta^2\Omega_2}{\delta\eta\delta\psi}. \tag{5.77}$$

(By inspection of Ω it's clear that variations of Ω_2 are zero except for $\delta\psi\delta\eta$.)

Similar to the GL case the form of $\delta\psi$ and $\delta\eta$ can be treated as a Fourier series expansion with y dependence. We define $\delta\Delta = \delta\Delta_c(z)\cos(ky) + \delta\Delta_s(z)\sin(ky)$ and $\delta\mathbf{A} = \hat{y}(\delta A_{yc}(z)\cos(ky) + \delta A_{ys}(z)\sin(ky)) + \hat{z}(\delta A_{zc}(z)\cos(ky) + \delta A_{zs}(z)\sin(ky))$. Similarly $\delta\eta = \delta\eta_c(z)\cos(ky)$ $+\delta\eta_s(z)\sin(ky)$ This time A_{yc}, A_{zs}, and Δ_c may not decouple from A_{ys}, A_{zc}, and Δ_s due to interactions

with $\delta\eta_c$ and $\delta\eta_s$. The details for evaluating the Hessian are very similar to what we do for GL theory.

5.7 Eilenberger Results

5.7.1 Convergence of Constants

One challenge of Eilenberger theory is figuring out if for a given temperature the solutions are evaluated at the correct number of Matsubara frequencies and points on the Fermi surface. We described in section 5.6.4 how to evaluate the value of $\Delta(z)$ deep inside the superconductor from an infinite sum of Matsubara frequencies. We call this ΔT. In practice we must truncate this sum for an approximate value of ΔT. This means ΔT is a function of the number of Matsubara frequencies used, $N\omega$. We define the error of ΔT to be $|\Delta T(N\omega) - \Delta T(N\omega - 1)|$. In figure 5.5 we show how this error drops as the number of Matsubara frequencies increases. This calculation is done at $t = \frac{T}{T_c} = 0.95$.

The number of Matsubara frequencies required to reach a given accuracy depends on temperature. Figure 5.6 shows the number of Matsubara frequencies needed to achieve an error under 10^{-8}. Note that $N\omega$ increases very quickly at low temperatures.

We discussed how to evaluate the penetration depth λ in section 5.6.6. This quantity depends on $N\omega$, the temperature, and κ_0. For our formulation length is measured in ξ_0, the coherence length at zero temperature. For this reason if κ_0 varies, only λ and λ_0 vary. For now we assume $\kappa_0 = 1$. The penetration depth also depends on m, the number of points used in each octant to evaluate the integral over the Fermi surface. We call the approximated penetration depth λT. Similar to ΔT, using many Matsubara frequencies reduces the error. Increasing m also changes the value of λT in a way that converges at large m. To see this we increase $N\omega$ until λT stops varying by 10^{-8}. We then increase m until λT once again stops varying significantly. In figure 5.7 we see how raising m

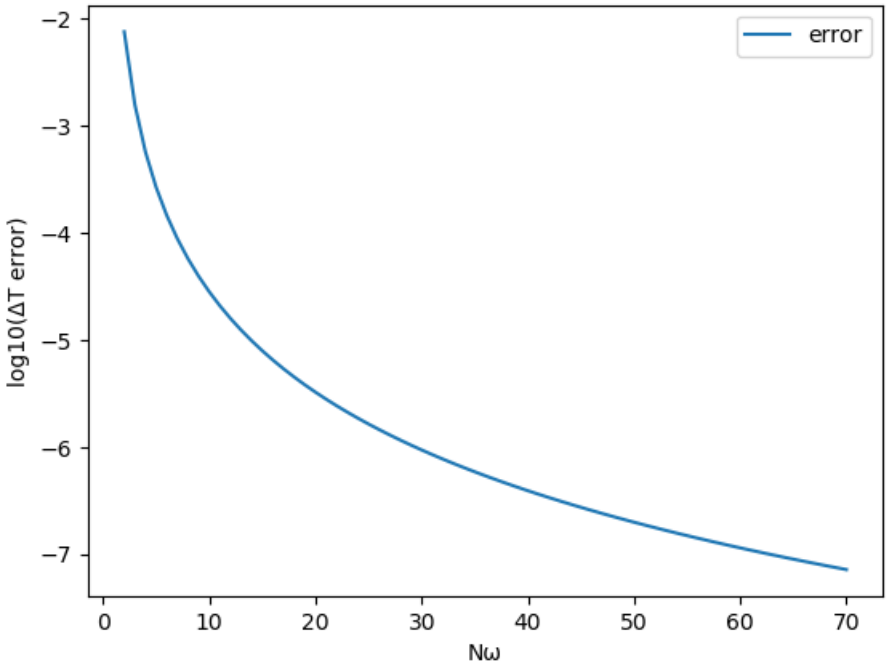

Figure 5.5 Plot of the log10 error of ΔT as the number of Matsubara frequencies used to evaluate it increases. ΔT is the value of the order parameter deep inside the superconductor. In theory this requires summing over all Matsubara frequencies. Truncating the sum introduces error which we define as $|\Delta T(N\omega) - \Delta T(N\omega - 1)|$. We see that as the number of Matsubara frequencies increases the error decreases.

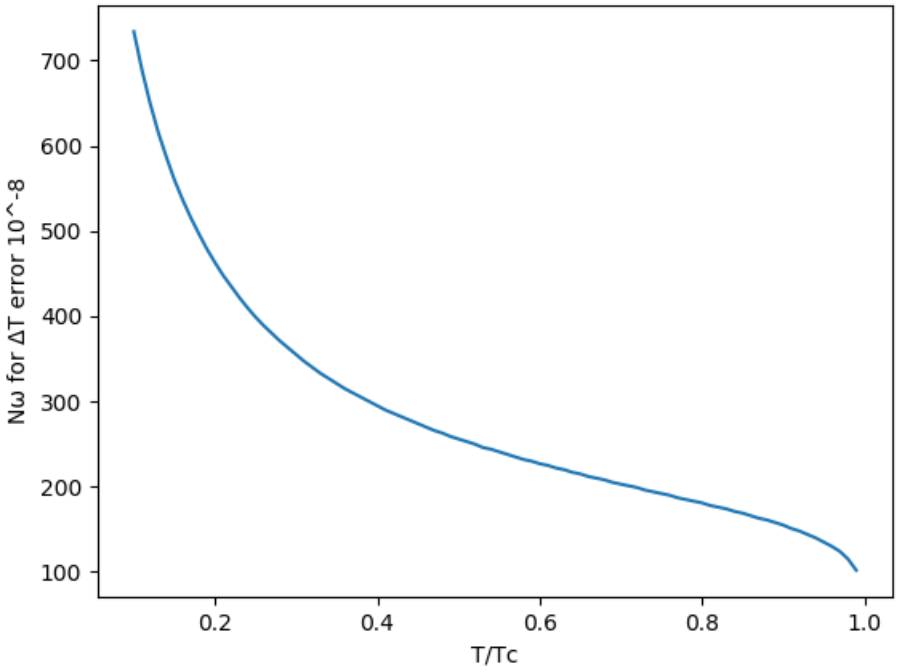

Figure 5.6 Plot showing the number of Matsubara frequencies required to reduce the error of ΔT below 10^{-8} as temperature varies. Note the sharp increase of $N\omega$ for small $\frac{T}{T_c}$.

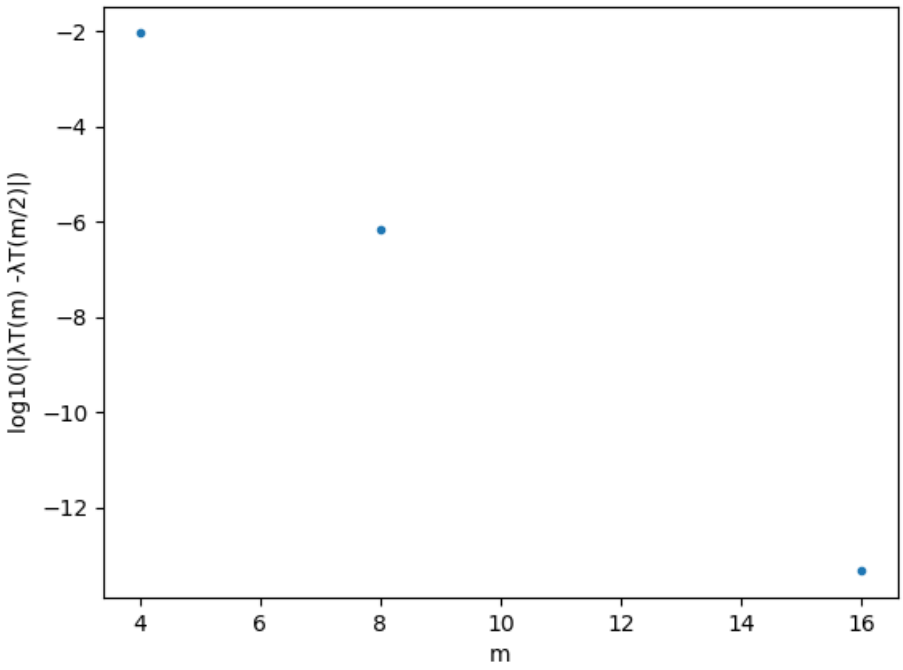

Figure 5.7 Define m as the number of points used to integrate the Fermi surface. We plot the decrease in error of the penetration depth λT as m increases. This is calculated at $t = \frac{T}{T_c} = 0.1$.

reduces the error. Note that we double m due to the way we take advantage of symmetries when integrating over the Fermi surface. This calculation was done at $t = 0.1$.

The calculation of ΔT was done previously by another author [38]. Our methods are identical for ΔT, but our approach to evaluating λT differs. The previous work uses the definition $\lambda = -\frac{A_y(0)}{A_y'(0)}$. The values of $A_y(0)$ were found by directly solving the Eilenberger equations and self consistent equations at low magnetic fields. In figure 5.8 we compare our new calculations with the old. We have the same qualitative behavior of λT. It increases with temperature and approaches one at $t = 0$. We set $m = 16$ and varied $N\omega$ to ensure our values were converged with errors below 10^{-9}. Other quantities like the critical magnetic field, coherence length, and κ for general temperatures can be calculated from ΔT and λT [38].

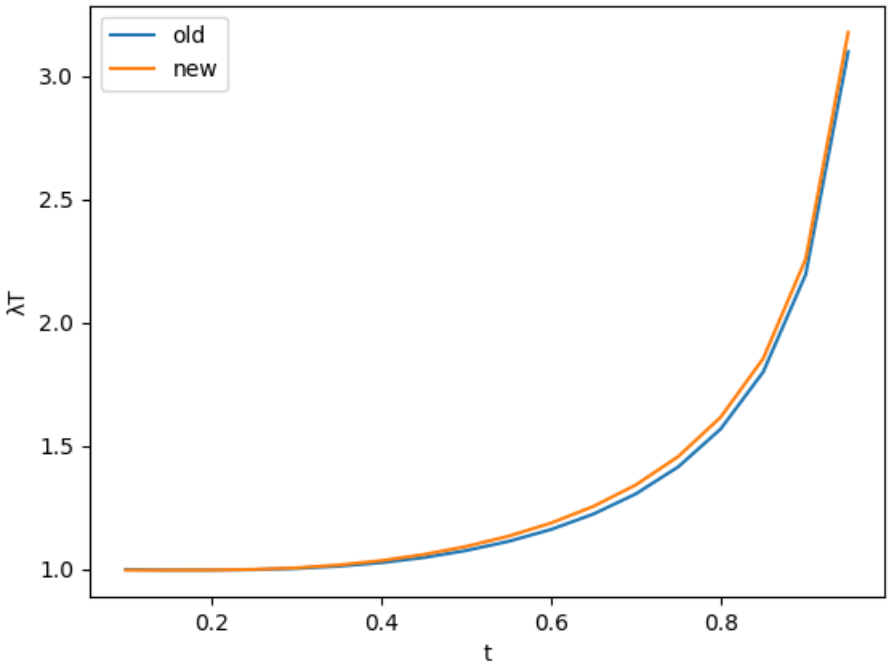

Figure 5.8 Comparison of estimated values of the penetration depth λT with our approach solving the linearized Eilenberger equations and a former approach defining $\lambda = -\frac{A(0)}{A_y'(0)}$ [38]. The qualitative behavior between the old and new results are the same. As $t \to 0$, $\lambda \to 1$ and as t gets larger so does λ. We set $m = 16$ and varied $N\omega$ to ensure our values were converged. We also have $\kappa_0 = 1$ with length measured in ξ_0.

5.7.2 Solutions of Variations

Though we've shown that $N\omega$ and m play a large role in determining convergence of our solutions, it is convenient to start with small $N\omega$ and m and worry about running large scale simulations once we've convinced ourselves everything is working. In the following results we assume $T = 0.95T_c$, $N\omega = 1$, and $m = 2$ unless otherwise stated.

First we confirm our calculations of the Green's functions match our linearized formulation. In figure 5.9 we plot the imaginary parts η for $H_a = 10^{-5}$. We do not plot the real parts as they are close to zero as expected. We can see that the estimated values follow our full calculation of η nicely. The deviations between the functions appear to be concentrated where we can't enforce boundary conditions for the linearized estimates.

At larger applied fields the real parts of η become nontrivial. In figure 5.10 we see the real parts of g and in figure 5.11 we see the real parts of f and $\bar{f}$. In figure 5.12 we see the imaginary parts of η are larger applied fields. Notice that $f = \bar{f}$ at $z = 0$ showing we are enforcing spectral boundary conditions.

Next we look at solutions of the first variations. In figure 5.13 we see Δ. Note how it drops off only at the surface. In figure 5.14 we see A_y. Deep in the superconductor $A_y = 0$ as expected.

Finally we give an example of how our estimates of H_{sh} compare to GL theory. GL theory is valid for temperatures close to T_c. Near T_c the penetration depth and coherence length diverge in Eilenberger theory. We must extrapolate the value of $\kappa(T)$ and H_{sh} in Eilenberger theory as $T \to T_c$ or $t = 1$. In figure 5.15 we show how we extrapolate our values of H_{sh} to $t = 1$. The absolute difference between the GL value and the EI value is 0.0140.

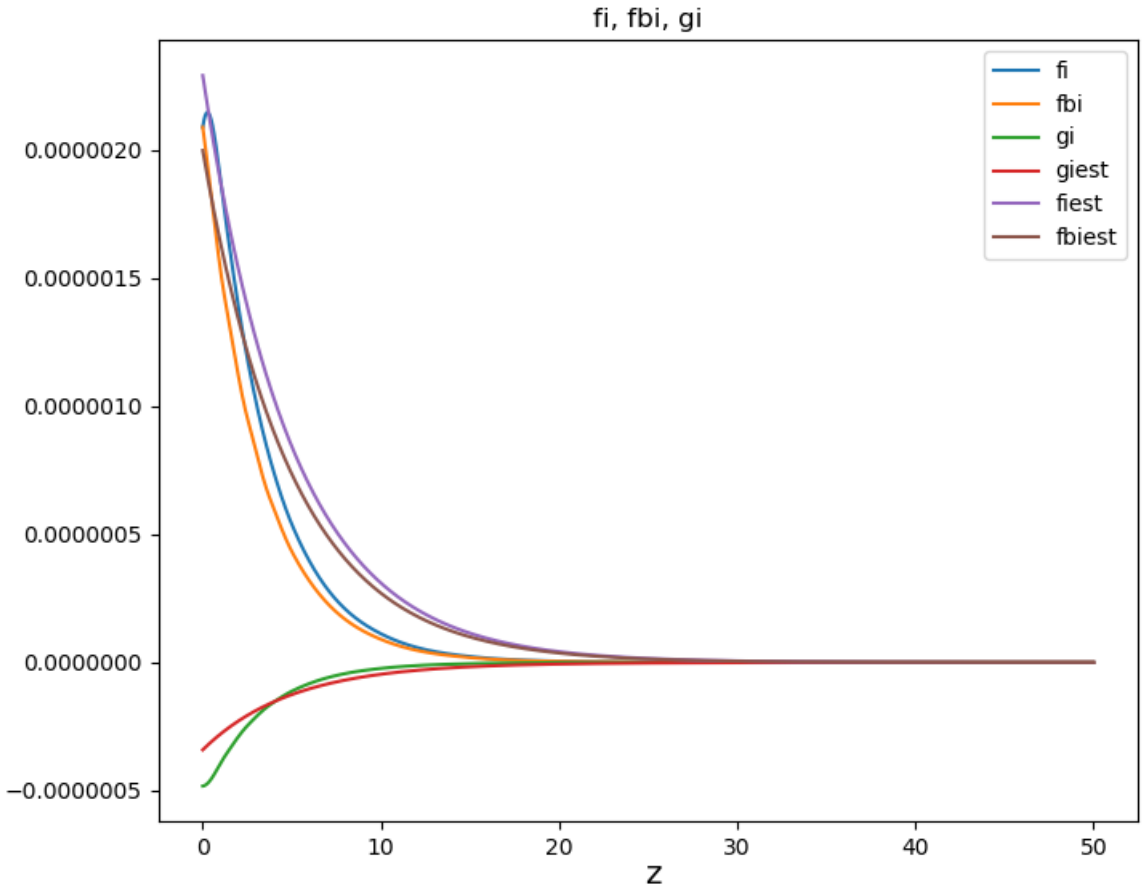

Figure 5.9 Plot of the imaginary parts of the Eilenberger Green's functions along with the estimated values found using the linearized Eilenberger equations for $H_a = 10^{-5}$. There is not a lot of literature with which to compare our evaluations of the Green's functions. For this reason it is beneficial to check that our results match approximate solutions at low applied fields. The full solutions match the approximated linearized solution very well except at $z = 0$. This is because we do not enforce spectral boundary conditions in the linear approximation. The real parts of the Green's functions are close to zero and so we do not plot them.

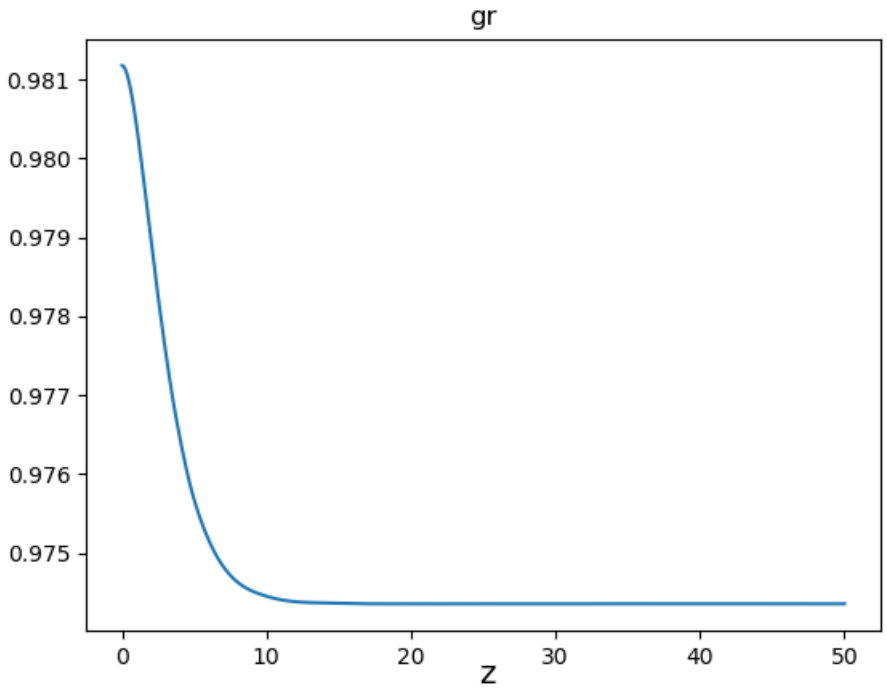

Figure 5.10 Plot of the real part of g. As expected deep inside the superconductor g approaches a constant value. Near the surface the magnetic field pulls g away from that constant value.

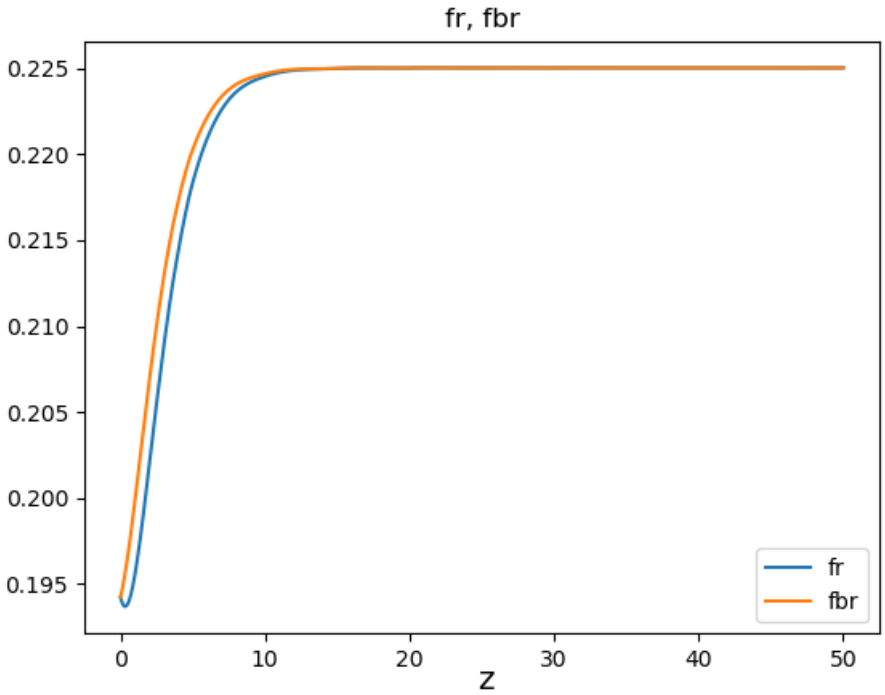

Figure 5.11 Plot of the real part of f and $\bar{f}$. Similar to g, these functions approach a constant value deep inside the superconductor. Note that at $z = 0$ we find that $f = \bar{f}$, indicating spectral boundary conditions are correctly being enforced.

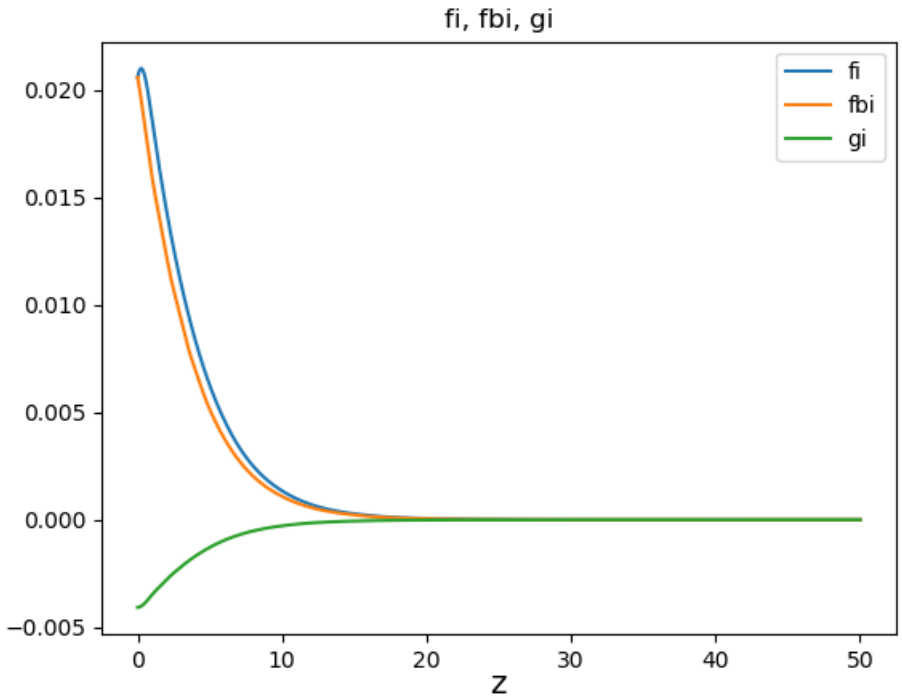

Figure 5.12 Plot of the imaginary part of all the Green's functions. These functions approach zero deep inside the superconductor at zero. We also observe that spectral boundary conditions are met for f and $\bar{f}$.

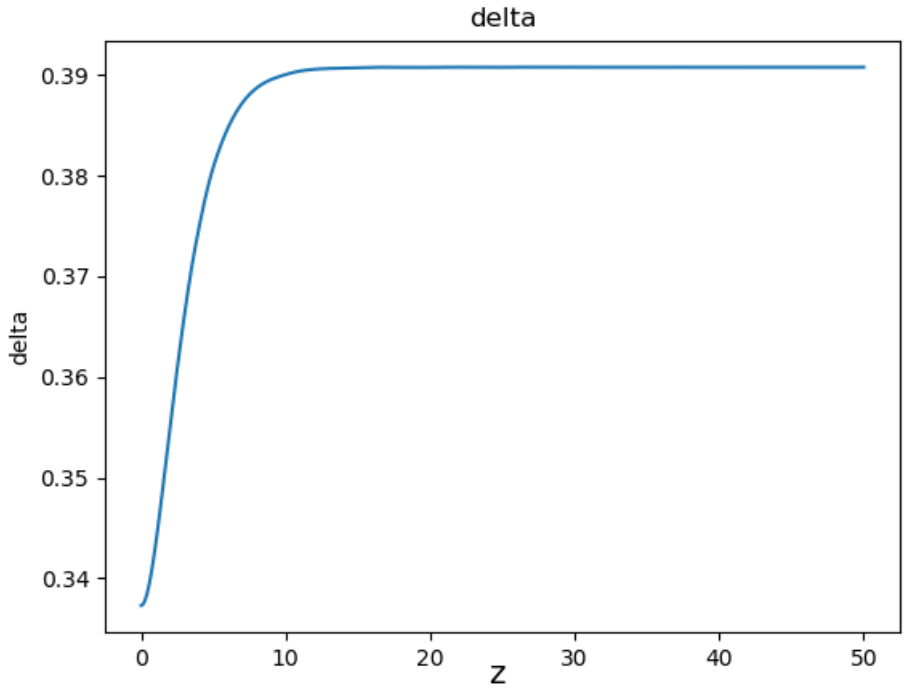

Figure 5.13 Plot of the order parameter. The order parameter drops near the surface indicating a reduction in superconducting electrons. Deep inside the order parameter approaches a constant value, ΔT.

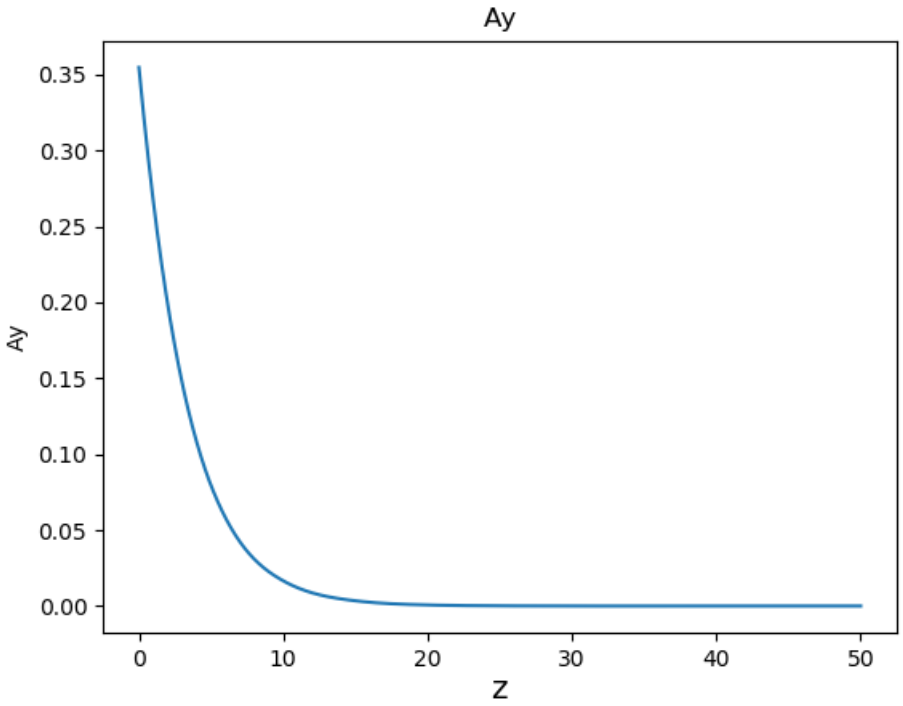

Figure 5.14 Plot of the magnetic vector potential. Near the surface the magnetic vector potential is large due to the influence of the magnetic field. We see the Meissner effect as the magnetic vector potential drops to zero deep inside the superconductor.

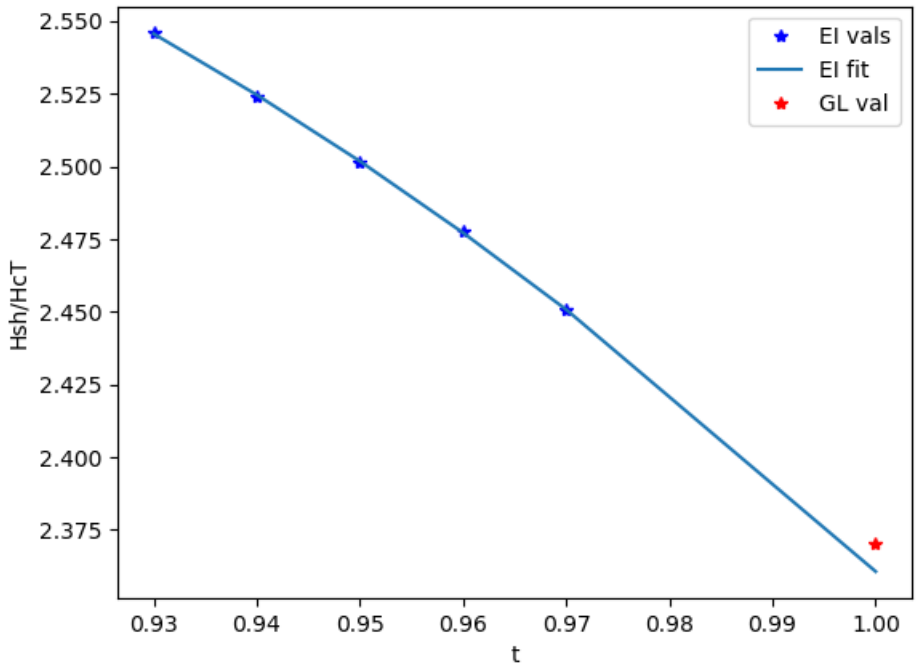

Figure 5.15 Plot of our fit of H_{sh} as $t = \frac{T}{T_c} = 1$. Both the penetration depth and coherence length diverge at $t = 1$ requiring us to extrapolate both $\kappa(T)$ and $H_{sh}(T)$. In this fit we miss the true value by 0.0140.

5.8 Conclusion

It is clear that the Eilenberger equations are much more complicated than the TDGL equations. Using precompiled matrices, taking advantage of symmetries, and parallelizing the code is necessary to reduce the time to evaluate the first and second variations. We've also seen how many terms in the free energy can be ignored after the Eilenberger equations and sensitivity equations are solved for.

We tested convergence for the order parameter and penetration depth. To reach an accuracy of 10^{-8} requires hundreds of Matsubara frequencies and 16 points on each octant of the Fermi surface. This makes creating qualitatively accurate calculations a daunting task.

To verify if our evaluation of the Green's functions is correct we compared our solutions to the linearized Eilenberger equations at low applied fields. We saw that the estimates closely matched the actual Green's functions except where we could not enforce boundary conditions. We also observed that our calculations of Δ and $\mathbf{A}$ match physical behaviors in superconductors.

We've shown that we are successfully able to evaluate the Eilenberger Green's functions and have compared them to the solutions for the linearized Eilenberger equations. We have also successfully evaluated the order parameter and magnetic vector potential and seen that they match physical expectations.

Finally we showed where our current calculations of H_{sh} in Eilenberger theory compares to GL theory. The next step would be a long task of running simulations at lower temperatures. This is tedious and with a little work could be formulated as an undergraduate student project.

Chapter 6

Conclusion

In this dissertation I presented a formulation of the time-dependent Ginzburg-Landau equations that flexibly captures a diverse set of inhomogeneities. Some defects we explored are surface roughness, grain boundaries, and islands of Sn deficiency. Using bifurcation theory, we calculated H_{sh} with all of these defects, and also captured the underlying mode that causes the transition from the Meissner state to the vortex state. We showed how this provides insight to a large community of scientists seeking to develop new SRF cavities made from Nb_3Sn. Besides defects, we simulated the performance of superconducting films in AC magnetic fields. We also showed cooling can lead to expulsion of trapped magnetic flux.

We provided an alternative method for evaluating the equations of motion and stability of Ginzburg-Landau and Eilenberger theory. By using automatic differentiation we automated the process of evaluating the first and second variation of the free energies. We first applied this to GL theory and showed that we could match previous calculations of H_{sh} and k_c. We also showed how adding spatial dependence to the effective mass changes H_{sh}. We repeated the process for Eilenberger theory. Much of our efforts in Eilenberger theory centered on creating efficient, simple procedures to minimize the risk of human error and speed up numerical calculations. We've done so by recognizing we can drop some terms of the free energy after solving the sensitivity

equations and Eilenbeger equations. We also exploited symmetries of the Eilenberger equations, and used preintegration matrices. By linearizing the Eilenberger equations we showed that our full calculations of the Green's functions are accurate. We have calculated the order parameter and magnetic vector potential. Finally, we've shown that we can roughly extrapolate the values of H_{sh} in Eilenberger theory to the values in GL theory.

6.1 Limitations

One limitation to GL theory is that it is not quantitatively valid at temperatures far from T_c. Despite this fact, we still observe correct qualitative behavior. We can still run simulations and acquire a rough idea of how defects, AC fields, and temperature waves impact superconductivity.

Both Eilenberger theory and GL theory fail to capture strong coupling between phonons and electrons. This requires more complicated theories like Eliashberg theory.

6.2 Possible Extensions

Advances in SRF materials and technology will continuously motivate new simulations. Some simulations that could be run in the future are,

1. Varying temperature gradients to observe when they are first capable of moving vortices off pinning sites.

2. Creating a phase diagram of all the different AC magnetic field behaviors.

3. Directly implementing the effective mass into the GL formulation.

4. Simulating Josephson junctions.

The obvious extension of Eilenberger theory is to evaluate H_{sh} and k_c at a wide range of temperatures. This would require calculations with lots of Matsubara frequencies. Another extension is to consider generalized Fermi surfaces evaluated from density functional theory. As the foundation for this work has been set, we consider this ready to hand off as another project.

Nb_3Sn is a strongly coupled superconductor. Using Eliashberg theory, one could include strong coupling effects. This would require a reformulation similar to what we've done with Eilenberger theory in this thesis.

6.3 In Summary

Computational methods allow us to explore physics in superconductors that is difficult to measure and hard to study with pen and paper. As our collaborators imaged new defects we've adjusted our simulations to match them. Working together as a team we've produced not only data, but an underlying theory to explain it.

By recruiting undergraduate students, this work will continue to live past my time at BYU. Some students have already taken the code I wrote beyond what I initially had envisioned. The code for both the work on GL theory and Eilenberger theory is now kept and maintained on a GitLab repository managed by my advisor. I hope that as the Center for Bright Beams continues to find new questions that this work can be adapted to find new answers.

Appendix A

Nondimensionalization of TDGL

The following derivation was taken from Aiden Harbick's 2019 Summer Report. Used with permission.

A.1 Nondimensionalizing the Ginzburg-Landau Equations

A.1.1 Initial Equations and Useful Values

We will first nondimensionalize the time independent Ginzburg-Landau equations, listed below (it should be noted that this section of the appendix is closely related to work done in [46] and [49]):

$$\frac{1}{2m_s}\left(-i\hbar\nabla - \frac{e_s}{c}\mathbf{A}\right)^2\psi + \alpha\psi + \beta|\psi|^2\psi = 0 \text{ in the domain} \tag{A.1}$$

$$\nabla\times\nabla\times\mathbf{A} - \frac{2\pi i e_s\hbar}{m_s c}(\psi^*\nabla\psi - \psi\nabla\psi^*) - \frac{4\pi e_s^2}{m_s c^2}|\psi|^2\mathbf{A} = 0 \text{ in the domain} \tag{A.2}$$

$$\left(i\hbar\nabla\psi + \frac{e_s}{c}\mathbf{A}\psi\right)\cdot n = 0 \text{ on the boundary} \tag{A.3}$$

$$(\nabla\times\mathbf{A})\times n = \mathbf{H}\times n \text{ on the boundary} \tag{A.4}$$

To nondimensionalize these equations, we first start by getting a few useful constants from these equations. The coherence length, ξ, can be found by looking at equation A.1, and letting $\mathbf{A} = 0$

(and thus ψ will be real):

$$\nabla^2\psi + \frac{1}{\xi^2}\left(\psi + \frac{\beta}{\alpha}\psi^3\right) = 0 \tag{A.5}$$

Where $\xi^2 = \frac{-\hbar^2}{2m_s\alpha}$. The coherence length is the length scale for the variance of ψ.

The penetration depth, λ, can be found by looking at equation A.2 and considering the material to be perfectly superconducting, i.e. $\psi = \psi_0 = \left(\frac{-\alpha}{\beta}\right)^{\frac{1}{2}}$, this makes the second term in the equation go to 0 and we get:

$$\nabla \times \nabla \times \mathbf{A} + \frac{1}{\lambda^2}\mathbf{A} = 0 \tag{A.6}$$

Where $\lambda^2 = \frac{m_s c^2}{4\pi e_s^2 |\psi_0|^2} = \frac{-\beta m_s c^2}{4\pi e_s^2 \alpha}$. The penetration depth is a length scale for how deep magnetic field is able to penetrate into a superconducting material.

We now have the well known Ginzburg-Landau parameter, $\kappa = \frac{\lambda}{\xi} = \sqrt{\frac{\beta}{2\pi}}\frac{m_s c}{e_s \hbar}$. The material's critical field, $H_c = \frac{4\pi\alpha^2}{\beta}$ also becomes a useful constant later.

A.1.2 Nondimensionalization

To nondimensionalize the GL equations, we make a number of coordinate transformations: $x = \lambda x'$ (and therefore $\nabla = \frac{1}{\lambda}\nabla'$), $\mathbf{A} = \sqrt{2}H_c\lambda\mathbf{A}'$, and $\psi = \sqrt{\frac{-\alpha}{\beta}}\psi'$. Doing this to equation A.1:

$$\frac{1}{2m_s}\left(\frac{-i\hbar}{\lambda}\nabla' - \frac{\sqrt{2}H_c\lambda e_s}{c}\mathbf{A}'\right)^2 \sqrt{\frac{-\alpha}{\beta}}\psi' + \alpha\sqrt{\frac{-\alpha}{\beta}}\psi' + \beta\sqrt{\frac{-\alpha}{\beta}}^3 |\psi'|^2\psi' = 0 \tag{A.7}$$

Dropping the primes and dividing by $\alpha\sqrt{\frac{-\alpha}{\beta}}$ gives:

$$\frac{1}{2m_s\alpha}\left(\frac{-i\hbar}{\lambda}\nabla - \frac{\sqrt{2}H_c\lambda e_s}{c}\mathbf{A}\right)^2 \psi + \psi - |\psi|^2\psi = 0 \tag{A.8}$$

If we bring the $\frac{1}{2m_s\alpha}$ into the parentheses of the first term (square rooting it of course), and expand out the λs and Hc, you will see that the term in front of $\mathbf{A}$ goes to 1, and the term in front of the ∇

goes to $\frac{-i}{\kappa}$, so the final equation is:

$$\left(\frac{-i}{\kappa}\nabla - \mathbf{A}\right)^2 \psi + \psi - |\psi|^2\psi = 0 \tag{A.9}$$

If we make the same transformations for equation A.2, we get the following:

$$\frac{\sqrt{2}H_c}{\lambda}\nabla\times\nabla\times\mathbf{A}' + \frac{2\pi i e_s\hbar\alpha}{m_s c\lambda\beta}\left(\psi\prime^*\nabla'\psi' - \psi'\nabla'\psi\prime^*\right) + \frac{4\pi e_s^2\alpha}{m_s c^2\beta}|\psi'|^2\sqrt{2}H_c\lambda\mathbf{A}' = 0 \tag{A.10}$$

Once again dropping the primes and then multiplying by $\frac{\lambda}{\sqrt{2}H_c}$ gives:

$$\nabla\times\nabla\times\mathbf{A} + \frac{2\pi i e_s\hbar\alpha}{m_s c\sqrt{2}H_c\beta}(\psi^*\nabla\psi - \psi\nabla\psi^*) + \frac{4\pi e_s^2\alpha\lambda^2}{m_s c^2\beta}|\psi|^2\mathbf{A} = 0 \tag{A.11}$$

Expanding H_c and λ again makes the coefficients in front of the second term reduce to $\frac{i}{2\kappa}$, and the terms in front of $|\psi|^2\mathbf{A}$ reduce to 1:

$$\nabla\times\nabla\times\mathbf{A} + \frac{i}{2\kappa}(\psi^*\nabla\psi - \psi\nabla\psi^*) + |\psi|^2\mathbf{A} = 0 \tag{A.12}$$

For the first boundary condition, it follows the same process as for the first term in equation A.9, and doing the transformations for the last boundary equation, there will be $\sqrt{2}Hc$ in front of both terms, which cancel, so the final nondimensionalized equations are:

$$\left(\frac{-i}{\kappa}\nabla - \mathbf{A}\right)^2 \psi + \psi - |\psi|^2\psi = 0 \tag{A.13}$$

$$\nabla\times\nabla\times\mathbf{A} + \frac{i}{2\kappa}(\psi^*\nabla\psi - \psi\nabla\psi^*) + |\psi|^2\mathbf{A} = 0 \tag{A.14}$$

$$\left(\frac{i}{\kappa}\nabla\psi + \mathbf{A}\psi\right)\cdot n = 0 \tag{A.15}$$

$$(\nabla\times\mathbf{A})\times n = \mathbf{H}\times n \tag{A.16}$$

A.1.3 α and β Spacial Dependence

Now we want to let α and β vary with space, this can represent different materials, or material defects. To do this, we make the transformations $\alpha = \alpha_0 a(\mathbf{r})$ and $\beta = \beta_0 b(\mathbf{r})$, where α_0 and β_0 are

constant reference values with the same units as α and β, and a and b are dimensionless functions of position. Returning to our definitions of ξ and λ, we see that setting $\mathbf{A} = 0$ in equation A.1 and collecting terms gives:

$$\nabla^2\psi + \frac{1}{\xi_0^2}\left(a\psi + \frac{\beta_0}{\alpha_0}b\psi^3\right) = 0 \tag{A.17}$$

Where $\xi_0^2 = \frac{-\hbar^2}{2m_s\alpha_0}$. To find the other length scale we once again let the material be perfectly superconducting, but this time in terms of the reference α and β; $\psi = \psi_0 = \left(\frac{-\alpha_0}{\beta_0}\right)^{\frac{1}{2}}$, this makes equation A.2 go to:

$$\nabla \times \nabla \times \mathbf{A} + \frac{1}{\lambda_0^2}\mathbf{A} = 0 \tag{A.18}$$

Where $\lambda_0^2 = \frac{m_s c^2}{4\pi e_s^2|\psi_0|^2} = \frac{-\beta_0 m_s c^2}{4\pi e_s^2 \alpha_0}$. Similarly, H_c becomes $H_{c0} = \frac{4\pi\alpha_0^2}{\beta_0}$, and $\kappa_0 = \frac{\lambda_0}{\xi_0} = \sqrt{\frac{\beta_0}{2\pi}}\frac{m_s c}{e_s\hbar}$. We then do the same process as we did before, but replacing any λ, ξ, κ, or H_c with λ_0, ξ_0, κ_0, or H_{c0}. This will result in almost the same equations, but with an a and a b in front of the ψ and $|\psi|^2\psi$ terms:

$$\left(\frac{-i}{\kappa_0}\nabla - \mathbf{A}\right)^2\psi + a\psi - b|\psi|^2\psi = 0 \tag{A.19}$$

$$\nabla \times \nabla \times \mathbf{A} + \frac{i}{2\kappa_0}\left(\psi^*\nabla\psi - \psi\nabla\psi^*\right) + |\psi|^2\mathbf{A} = 0 \tag{A.20}$$

$$\left(\frac{i}{\kappa_0}\nabla\psi + \mathbf{A}\psi\right)\cdot n = 0 \tag{A.21}$$

$$(\nabla \times \mathbf{A}) \times n = \mathbf{H} \times n \tag{A.22}$$

A.1.4 Time Dependent Ginzburg-Landau Equations

The Time Dependent Ginzburg-Landau equations are as follows:

$$\frac{1}{2m_s}\left(-i\hbar\nabla - \frac{e_s}{c}\mathbf{A}\right)^2\psi + \alpha\psi + \beta|\psi|^2\psi + \Gamma\left(\frac{\partial\psi}{\partial t} + \frac{ie_s\phi}{\hbar}\psi\right) = 0 \text{ in the domain} \tag{A.23}$$

$$\nabla \times \nabla \times \mathbf{A} - \frac{2\pi i e_s\hbar}{m_s c}\left(\psi^*\nabla\psi - \psi\nabla\psi^*\right) - \frac{4\pi e_s^2}{m_s c^2}|\psi|^2\mathbf{A} + \frac{4\pi\sigma_n}{c}\left(\frac{1}{c}\frac{\partial\mathbf{A}}{\partial t} + \nabla\phi\right) = 0 \text{ in the domain} \tag{A.24}$$

$$\left(i\hbar\nabla\psi + \frac{e_s}{c}\mathbf{A}\psi\right)\cdot n = 0 \text{ on the boundary} \tag{A.25}$$

$$(\nabla\times\mathbf{A})\times n = \mathbf{H}\times n \text{ on the boundary} \tag{A.26}$$

$$-\left(\nabla\phi + \frac{\partial\mathbf{A}}{\partial t}\right)\cdot n = 0 \text{ on the boundary} \tag{A.27}$$

We will start with α and β constant in time and space. To nondimensionalize these equations, we first use the same definitions for λ, ξ, κ, and H_c as we defined in section A.1.1. We also make the same change of variables as in section A.1.2 in addition to letting $t = \tau_\Delta t'$ and $\phi = \phi_0\phi'$; For equation A.23, this gives us:

$$\frac{1}{2m_s}\left(\frac{-i\hbar}{\lambda}\nabla' - \frac{\sqrt{2}H_c\lambda e_s}{c}\mathbf{A}'\right)^2\sqrt{\frac{-\alpha}{\beta}}\psi' + \alpha\sqrt{\frac{-\alpha}{\beta}}\psi' + \beta\sqrt{\frac{-\alpha}{\beta}}^3|\psi'|^2\psi' + \Gamma\sqrt{\frac{-\alpha}{\beta}}\left(\frac{1}{\tau_\Delta}\frac{\partial\psi'}{\partial t'} + \frac{ie_s\phi_0\phi'}{\hbar}\psi'\right) = 0 \tag{A.28}$$

Dropping the primes and dividing by $\alpha\sqrt{\frac{-\alpha}{\beta}}$ gives:

$$\frac{1}{2m_s\alpha}\left(\frac{-i\hbar}{\lambda}\nabla - \frac{\sqrt{2}H_c\lambda e_s}{c}\mathbf{A}\right)^2\psi + \psi - |\psi|^2\psi + \frac{\Gamma}{|\alpha|}\left(\frac{1}{\tau_\Delta}\frac{\partial\psi}{\partial t} + \frac{ie_s\phi_0\phi}{\hbar}\psi\right) = 0 \tag{A.29}$$

The first three terms reduce down to the same terms as in equation A.9. We then let $\tau_\Delta = \frac{\Gamma}{|\alpha|}$ and $\phi_0 = \frac{\hbar}{e_s\tau_\Delta}$ to get the final equation:

$$\left(\frac{-i}{\kappa}\nabla - \mathbf{A}\right)^2\psi + \psi - |\psi|^2\psi + \frac{\partial\psi}{\partial t} + i\phi\psi = 0 \tag{A.30}$$

Making the same coordinate transformations for equation A.24:

$$\frac{\sqrt{2}H_c}{\lambda}\nabla\times\nabla\times\mathbf{A}' + \frac{2\pi ie_s\hbar\alpha}{m_sc\lambda\beta}\left(\psi\prime^*\nabla'\psi' - \psi'\nabla'\psi\prime^*\right) + \frac{4\pi e_s^2\alpha}{m_sc^2\beta}|\psi'|^2\sqrt{2}H_c\lambda\mathbf{A}' + \frac{4\pi\sigma_n}{c}\left(\frac{\sqrt{2}H_c\lambda}{c\tau_\Delta}\frac{\partial\mathbf{A}'}{\partial t'} + \frac{\phi_0}{\lambda}\nabla'\phi'\right) = 0 \tag{A.31}$$

Dropping the primes and then multiplying by $\frac{\lambda}{\sqrt{2}H_c}$ gives:

$$\nabla\times\nabla\times\mathbf{A}+\frac{2\pi i e_s\hbar\alpha}{m_s c\sqrt{2}H_c\beta}(\psi^*\nabla\psi-\psi\nabla\psi^*)+\frac{4\pi e_s^2\alpha\lambda^2}{m_s c^2\beta}|\psi|^2\mathbf{A}+\frac{4\pi\sigma_n}{c}\left(\frac{\lambda^2}{c\tau_\Delta}\frac{\partial\mathbf{A}}{\partial t}+\frac{\phi_0}{\sqrt{2}H_c}\nabla\phi\right)=0 \tag{A.32}$$

Once again the first 3 terms go the same as A.12. We then define $\tau_j=\frac{\sigma_n\beta m_s}{e_s^2|\alpha|}$, which gives:

$$\nabla\times\nabla\times\mathbf{A}+\frac{i}{2\kappa}(\psi^*\nabla\psi-\psi\nabla\psi^*)+|\psi|^2\mathbf{A}+\frac{\tau_j}{\tau_\Delta}\frac{\partial\mathbf{A}}{\partial t}+\frac{4\pi\sigma_n\phi_0}{\sqrt{2}H_c c}\nabla\phi=0 \tag{A.33}$$

If we define $u=\frac{\tau_\Delta}{\tau_j}$, then the coefficients in front of the time derivative go to $\frac{1}{u}$, and it turns out that if we substitute in the value for ϕ_0 we found earlier, the coefficients in front of the $\nabla\phi$ go to $\frac{1}{u\kappa}$:

$$\nabla\times\nabla\times\mathbf{A}+\frac{i}{2\kappa}(\psi^*\nabla\psi-\psi\nabla\psi^*)+|\psi|^2\mathbf{A}+\frac{1}{u}\left(\frac{\partial\mathbf{A}}{\partial t}+\frac{1}{\kappa}\nabla\phi\right)=0 \tag{A.34}$$

So the final equations are:

$$\left(\frac{-i}{\kappa}\nabla-\mathbf{A}\right)^2\psi+\psi-|\psi|^2\psi+\frac{\partial\psi}{\partial t}+i\phi\psi=0 \tag{A.35}$$

$$\nabla\times\nabla\times\mathbf{A}+\frac{i}{2\kappa}(\psi^*\nabla\psi-\psi\nabla\psi^*)+|\psi|^2\mathbf{A}+\frac{1}{u}\left(\frac{\partial\mathbf{A}}{\partial t}+\frac{1}{\kappa}\nabla\phi\right)=0 \tag{A.36}$$

$$\left(\frac{i}{\kappa}\nabla\psi+\mathbf{A}\psi\right)\cdot n=0 \tag{A.37}$$

$$(\nabla\times\mathbf{A})\times n=\mathbf{H}\times n \tag{A.38}$$

$$-\left(\nabla\phi+\frac{\partial\mathbf{A}}{\partial t}\right)\cdot n=0 \tag{A.39}$$

A.1.5 α and β vary with time and space

If we now let $\alpha=\alpha_0 a(\mathbf{r},t)$ and $\beta=\beta_0 b(\mathbf{r},t)$, we can do the same thing as we did in section A.1.3, and let $\xi_0^2=\frac{-\hbar^2}{2m_s\alpha_0}$, $\lambda_0^2=\frac{m_s c^2}{4\pi e_s^2|\psi_0|^2}=\frac{-\beta_0 m_s c^2}{4\pi e_s^2\alpha_0}$, $H_{c0}=\frac{4\pi\alpha_0^2}{\beta_0}$, and $\kappa_0=\frac{\lambda_0}{\xi_0}=\sqrt{\frac{\beta_0}{2\pi}}\frac{m_s c}{e_s\hbar}$. Additionally we also let $\tau_{\Delta0}=\frac{\Gamma}{|\alpha_0|}$, $\tau_{j0}=\frac{\sigma_n\beta_0 m_s}{e_s^2|\alpha_0|}$, $u_0=\frac{\tau_{\Delta0}}{\tau_{j0}}$, and $\phi_0=\frac{\hbar}{e_s\tau_{\Delta0}}$. We can then follow the same steps as

above with these new values and we get:

$$\left(\frac{-i}{\kappa_0}\nabla - \mathbf{A}\right)^2 \psi + a\psi - b|\psi|^2\psi + \frac{\partial \psi}{\partial t} + i\phi\psi = 0 \tag{A.40}$$

$$\nabla \times \nabla \times \mathbf{A} + \frac{i}{2\kappa_0}(\psi^*\nabla\psi - \psi\nabla\psi^*) + |\psi|^2\mathbf{A} + \frac{1}{u_0}\left(\frac{\partial \mathbf{A}}{\partial t} + \frac{1}{\kappa_0}\nabla\phi\right) = 0 \tag{A.41}$$

$$\left(\frac{i}{\kappa_0}\nabla\psi + \mathbf{A}\psi\right)\cdot n = 0 \tag{A.42}$$

$$(\nabla \times \mathbf{A}) \times n = \mathbf{H} \times n \tag{A.43}$$

$$-\left(\nabla\phi + \frac{\partial \mathbf{A}}{\partial t}\right)\cdot n = 0 \tag{A.44}$$

To get these equations to the forms used in the rest of this report, we simply let $\phi = \kappa_0\theta$, and then drop the subscripts on u and κ.

A.2 Material Specific Formulation Derivation

A.2.1 Equations for Spatially Varying Material Coefficients

Below is the formulation from [47]:

$$\gamma\left(\frac{\partial \psi}{\partial t} - i\kappa_0\theta\psi\right) + \left(\frac{i}{\kappa_0}\nabla + \mathbf{A}\right)^2\psi - a\psi + b|\psi|^2\psi = 0 \tag{A.45}$$

$$\frac{1}{u_0}\left(\frac{\partial \mathbf{A}}{\partial t} - \nabla\theta\right) + \nabla \times \sigma + \frac{i}{2\kappa_0}(\psi^*\nabla\psi - \psi\nabla\psi^*) + |\psi|^2\mathbf{A} = \nabla \times H \tag{A.46}$$

$$\frac{1}{u_0}\frac{\partial \sigma}{\partial t} - \nabla^2\sigma + \frac{i}{2\kappa_0}\nabla \times (\psi^*\nabla\psi - \psi\nabla\psi^*) + |\psi|^2\sigma - \mathbf{A}\cdot\nabla \times |\psi|^2 = -\nabla^2 H \tag{A.47}$$

$$\frac{1}{u_0}\left(\frac{\partial \theta}{\partial t} - \nabla^2\theta\right) + \frac{i}{2\kappa_0}\nabla\cdot(\psi^*\nabla\psi - \psi\nabla\psi^*) + |\psi|^2\theta + \mathbf{A}\cdot\nabla|\psi|^2 = 0 \tag{A.48}$$

Where $\nabla \times \mathbf{A} = \sigma$ and $\nabla \cdot \mathbf{A} = \theta$, and equations A.47 and A.48 are found by taking the curl and divergence of equation A.46. If we want to let the electrical conductivity vary with space, we insert a dimensionless constant that we will call s to represent it into equation A.46 (normally we just

nondimensionalize the conductivity out, but if we want to let it vary in space/time we use this term):

$$\frac{s}{u_0}\left(\frac{\partial \mathbf{A}}{\partial t}-\nabla\theta\right)+\nabla\times\sigma+\frac{i}{2\kappa_0}\left(\psi^*\nabla\psi-\psi\nabla\psi^*\right)+|\psi|^2\mathbf{A}=\nabla\times H \tag{A.49}$$

The complication here is that since s varies with space, taking equation A.49's curl and divergence would result in multiple time derivative terms, which would create problems with solving it via Finite Element. To fix this, we will bring s into the time derivative and now let $\nabla\times s\mathbf{A}=\Sigma$ and $\nabla\cdot s\mathbf{A}=\Theta$, and therefore $\nabla\times\mathbf{A}=\frac{1}{s}\left(\Sigma-\nabla s\times\mathbf{A}\right)$ and $\nabla\cdot\mathbf{A}=\frac{1}{s}\left(\Theta-\mathbf{A}\cdot\nabla s\right)$. With these transformations, equations A.45 and A.46 become:

$$\gamma\left(\frac{\partial\psi}{\partial t}-i\frac{\kappa_0}{s}\left(\Theta-\mathbf{A}\cdot\nabla s\right)\psi\right)+\left(\frac{i}{\kappa_0}\nabla+\mathbf{A}\right)^2\psi-a\psi+b|\psi|^2\psi=0 \tag{A.50}$$

$$\frac{s}{u_0}\left(\frac{\partial\mathbf{A}}{\partial t}-\nabla\left(\frac{1}{s}\left(\Theta-\mathbf{A}\cdot\nabla s\right)\right)\right)+\nabla\times\left(\frac{1}{s}\left(\Sigma-\nabla s\times\mathbf{A}\right)\right)+\frac{i}{2\kappa_0}\left(\psi^*\nabla\psi-\psi\nabla\psi^*\right)+|\psi|^2\mathbf{A}=\nabla\times H \tag{A.51}$$

Taking the curl of Equation A.51 gives:

$$\frac{1}{u_0}\left(\frac{\partial\Sigma}{\partial t}-\nabla s\times\nabla\left(\frac{1}{s}\left(\Theta-\mathbf{A}\cdot\nabla s\right)\right)\right)-\nabla^2\left(\frac{1}{s}\left(\Sigma-\nabla s\times\mathbf{A}\right)\right)+\frac{i}{2\kappa_0}\nabla\times\left(\psi^*\nabla\psi-\psi\nabla\psi^*\right)+|\psi|^2\frac{1}{s}(\Sigma-\nabla s\times\mathbf{A})-\mathbf{A}\cdot\nabla\times|\psi|^2=-\nabla^2 H \tag{A.52}$$

This equation could be further expanded if doing so improves finite element speed or stability, but we will leave it in this form for right now, in order to be able to solve this, we will have to define ∇s by hand as well as s, since numerical methods do not deal well with higher than first order derivative terms. It should also be noted that this term is no longer decoupled, as there is a Θ term in it. Taking

the divergence of Equation A.51:

$$\frac{1}{u_0}\left(\frac{\partial\Theta}{\partial t}-s\nabla^2\left(\frac{1}{s}\left(\Theta-\mathbf{A}\cdot\nabla s\right)\right)-\nabla\left(\frac{1}{s}\left(\Theta-\mathbf{A}\cdot\nabla s\right)\right)\cdot\nabla s\right)+\frac{i}{2\kappa_0}\nabla\cdot\left(\psi^*\nabla\psi-\psi\nabla\psi^*\right)$$
$$+|\psi|^2\frac{1}{s}(\Theta-\mathbf{A}\cdot\nabla s)+\mathbf{A}\cdot\nabla|\psi|^2=0 \tag{A.53}$$

So equations A.50, A.51, A.52, and A.53 are the new equations we can now solve to simulate multiple specific materials or specific material properties, as long as we provide both s and ∇s.

A.2.2 Adding Time Dependence to Conductivity

It seems likely that the conductivity varies with temperature, and therefore varies with time, so it would be useful to also add time dependence to s. To do this while maintaining the positional dependence, we simply have to add an extra term into our equations to be able to still move the s into the time derivative, as $s\frac{\partial\mathbf{A}}{\partial t}=\frac{\partial s\mathbf{A}}{\partial t}-\mathbf{A}\frac{\partial s}{\partial t}$. Much like we have to provide ∇s for the position dependence, we will also have to provide $\frac{\partial s}{\partial t}$. The curl of $\mathbf{A}\frac{\partial s}{\partial t}$ is $\frac{\partial s}{\partial t}\frac{1}{s}(\Sigma-\nabla s\times\mathbf{A})+\nabla\frac{\partial s}{\partial t}\times\mathbf{A}$ and the divergence of $\mathbf{A}\frac{\partial s}{\partial t}$ is $\frac{\partial s}{\partial t}\frac{1}{s}(\Theta-\mathbf{A}\cdot\nabla s)+\mathbf{A}\cdot\nabla\frac{\partial s}{\partial t}$. Thus the final equations become:

$$\gamma\left(\frac{\partial\psi}{\partial t}-i\frac{\kappa_0}{s}\left(\Theta-\mathbf{A}\cdot\nabla s\right)\psi\right)+\left(\frac{i}{\kappa_0}\nabla+\mathbf{A}\right)^2\psi-a\psi+b|\psi|^2\psi=0 \tag{A.54}$$

$$\frac{1}{u_0}\left(\frac{\partial s\mathbf{A}}{\partial t}-\mathbf{A}\frac{\partial s}{\partial t}-s\nabla\left(\frac{1}{s}\left(\Theta-\mathbf{A}\cdot\nabla s\right)\right)\right)+\nabla\times\left(\frac{1}{s}\left(\Sigma-\nabla s\times\mathbf{A}\right)\right)+\frac{i}{2\kappa_0}\left(\psi^*\nabla\psi-\psi\nabla\psi^*\right)$$
$$+|\psi|^2\mathbf{A}=\nabla\times H \tag{A.55}$$

$$\frac{1}{u_0}\left(\frac{\partial\Sigma}{\partial t}-\frac{\partial s}{\partial t}\frac{1}{s}(\Sigma-\nabla s\times\mathbf{A})-\nabla\frac{\partial s}{\partial t}\times\mathbf{A}-\nabla s\times\nabla\left(\frac{1}{s}\left(\Theta-\mathbf{A}\cdot\nabla s\right)\right)\right)-\nabla^2\left(\frac{1}{s}\left(\Sigma-\nabla s\times\mathbf{A}\right)\right)$$
$$+\frac{i}{2\kappa_0}\nabla\times\left(\psi^*\nabla\psi-\psi\nabla\psi^*\right)+|\psi|^2\frac{1}{s}(\Sigma-\nabla s\times\mathbf{A})-\mathbf{A}\cdot\nabla\times|\psi|^2=-\nabla^2 H \tag{A.56}$$

$$\frac{1}{u_0}\left(\frac{\partial\Theta}{\partial t}-\frac{\partial s}{\partial t}\frac{1}{s}(\Theta-\mathbf{A}\cdot\nabla s)-\mathbf{A}\cdot\nabla\frac{\partial s}{\partial t}-s\nabla^2\left(\frac{1}{s}(\Theta-\mathbf{A}\cdot\nabla s)\right)-\nabla\left(\frac{1}{s}(\Theta-\mathbf{A}\cdot\nabla s)\right)\cdot\nabla s\right)$$
$$+\frac{i}{2\kappa_0}\nabla\cdot(\psi^*\nabla\psi-\psi\nabla\psi^*)+|\psi|^2\frac{1}{s}(\Theta-\mathbf{A}\cdot\nabla s)+\mathbf{A}\cdot\nabla|\psi|^2=0 \tag{A.57}$$

Bibliography

[1] H. K. Onnes, "The superconductivity of mercury," Comm. Phys. Lab. Univ. Leiden **122,** 124 (1911).

[2] W. Meissner and R. Ochsenfeld, "Ein neuer effekt bei eintritt der supraleitfähigkeit," Naturwissenschaften **21,** 787–788 (1933).

[3] L. D. Landau and V. Ginzburg, "On the theory of superconductivity," Zh. Eksp. Teor. Fiz. **20,** 1064 (1950).

[4] J. Bardeen, L. N. Cooper, and J. R. Schrieffer, "Microscopic theory of superconductivity," Physical Review **106,** 162 (1957).

[5] L. GorâĂŹKov, "On the energy spectrum of superconductors," Sov. Phys. JETP **7,** 158 (1958).

[6] L. P. GorâĂŹkov, "Microscopic derivation of the Ginzburg-Landau equations in the theory of superconductivity," Sov. Phys. JETP **9,** 1364–1367 (1959).

[7] G. Eliashberg, "Interactions between electrons and lattice vibrations in a superconductor," Sov. Phys. JETP **11,** 696–702 (1960).

[8] G. Eilenberger, "Transformation of Gorkov's equation for type II superconductors into transport-like equations," Zeitschrift für Physik A Hadrons and nuclei **214,** 195–213 (1968).

[9] A. R. Pack, "Computational Exploration of Vortex Nucleation in Type II Superconductors Using a Finite Element Method in Ginzburg-Landau Theory," (2017).

[10] C. Bean and J. Livingston, "Surface barrier in type-II superconductors," Physical Review Letters **12,** 14 (1964).

[11] M. "Transtrum, "personal communication".

[12] M. K. Transtrum, G. Catelani, and J. P. Sethna, "Superheating field of superconductors within Ginzburg-Landau theory," Physical Review B **83,** 094505 (2011).

[13] S. J. Chapman, "Superheating field of type II superconductors," SIAM Journal on Applied Mathematics **55,** 1233–1258 (1995).

[14] A. J. Dolgert, S. J. Di Bartolo, and A. T. Dorsey, "Superheating fields of superconductors: Asymptotic analysis and numerical results," Physical Review B **53,** 5650 (1996).

[15] L. Kramer, "Stability limits of the meissner state and the mechanism of spontaneous vortex nucleation in superconductors," Physical Review **170,** 475 (1968).

[16] P. De Gennes, "Vortex nucleation in type II superconductors," Solid State Communications **3,** 127–130 (1965).

[17] V. Galaiko, "Stability limit of the superconducting state in a magnetic field for superconductors of the second kind," Sov. Phys. JETP **23,** 475–478 (1966).

[18] L. Kramer, "Breakdown of the superheated meissner state and spontaneous vortex nucleation in type ii superconductors," Zeitschrift für Physik A Hadrons and nuclei **259,** 333–346 (1973).

[19] H. Fink and A. Presson, "Stability limit of the superheated Meissner state due to three-dimensional fluctuations of the order parameter and vector potential," Physical Review **182,** 498 (1969).

[20] P. V. Christiansen, "Magnetic superheating of high-κ superconductors," Solid State Communications **7,** 727–729 (1969).

[21] P. Soininen and N. Kopnin, "Stability of superflow," Physical Review B **49,** 12087 (1994).

[22] D. Y. Vodolazov, "Effect of surface defects on the first field for vortex entry in type-II superconductors," Physical Review B **62,** 8691 (2000).

[23] L. Burlachkov, M. Konczykowski, Y. Yeshurun, and F. Holtzberg, "Bean–Livingston barriers and first field for flux penetration in high-T c crystals," Journal of applied physics **70,** 5759–5761 (1991).

[24] A. Y. Aladyshkin, A. Mel'Nikov, I. Shereshevsky, and I. Tokman, "What is the best gate for vortex entry into type-II superconductor?," Physica C: Superconductivity **361,** 67–72 (2001).

[25] M. Machida and H. Kaburaki, "Direct simulation of the time-dependent Ginzburg-Landau equation for type-II superconducting thin film: Vortex dynamics and V-I characteristics," Physical review letters **71,** 3206 (1993).

[26] A. E. Koshelev, I. A. Sadovskyy, C. L. Phillips, and A. Glatz, "Optimization of vortex pinning by nanoparticles using simulations of the time-dependent Ginzburg-Landau model," Physical Review B **93,** 060508 (2016).

[27] Q. Du, "Finite element methods for the time-dependent Ginzburg-Landau model of superconductivity," Computers & Mathematics with Applications **27,** 119–133 (1994).

[28] B. Oripov and S. Anlage, "Time-dependent Ginzburg-Landau treatment of RF Magnetic Vortices in Superconductors: Vortex-Semiloops in a Spatially Nonuniform Magnetic Field," arXiv preprint arXiv:1909.02714 (2019).

[29] A. T. Dorsey, "Vortex motion and the Hall effect in type-II superconductors: A time-dependent Ginzburg-Landau theory approach," Physical Review B **46,** 8376 (1992).

[30] B. Li and Z. Zhang, "A new approach for numerical simulation of the time-dependent Ginzburg–Landau equations," Journal of Computational Physics **303,** 238–250 (2015).

[31] H. Gao and W. Sun, "An efficient fully linearized semi-implicit Galerkin-mixed FEM for the dynamical Ginzburg–Landau equations of superconductivity," Journal of Computational Physics **294,** 329–345 (2015).

[32] I. A. Sadovskyy, A. E. Koshelev, C. L. Phillips, D. A. Karpeyev, and A. Glatz, "Stable large-scale solver for Ginzburg–Landau equations for superconductors," Journal of Computational Physics **294,** 639–654 (2015).

[33] M. P. Sørensen, N. F. Pedersen, and M. Ögren, "The dynamics of magnetic vortices in type II superconductors with pinning sites studied by the time dependent Ginzburg–Landau model," Physica C: Superconductivity and its applications **533,** 40–43 (2017).

[34] J. Deang, Q. Du, M. Gunzburger, and J. Peterson, "Vortices in superconductors: modelling and computer simulations," Philosophical Transactions of the Royal Society of London. Series A: Mathematical, Physical and Engineering Sciences **355,** 1957–1968 (1997).

[35] A. Benfenati, A. Maiani, F. N. Rybakov, and E. Babaev, "Vortex nucleation barriers in superconductors revisited," arXiv preprint arXiv:1911.09513 (2019).

[36] G. Catelani and J. P. Sethna, "Temperature dependence of the superheating field for superconductors in the high-κ London limit," Physical Review B **78,** 224509 (2008).

[37] F. P.-J. Lin and A. Gurevich, "Effect of impurities on the superheating field of type-II superconductors," Physical Review B **85,** 054513 (2012).

[38] M. Transtrum, "Information Geometry For Nonlinear Least-Squares Data Fitting And Calculation Of The Superconducting Superheating Field," (2011).

[39] A. Romanenko *et al.*, "Pathway to High Gradients in Superconducting RF Cavities by Avoiding Flux Dissipation," In *Proc. of International Particle Accelerator Conference (IPAC'18)*, (2018).

[40] M. Sunde, L. C. Serpell, M. Bartlam, P. E. Fraser, M. B. Pepys, and C. C. Blake, "Common core structure of amyloid fibrils by synchrotron X-ray diffraction," Journal of molecular biology **273,** 729–739 (1997).

[41] C. R. Wie, "High resolution X-ray diffraction characterization of semiconductor structures," Materials Science and Engineering: R: Reports **13,** 1–56 (1994).

[42] J. Kortright, D. Awschalom, J. Stöhr, S. Bader, Y. Idzerda, S. Parkin, I. K. Schuller, and H.-C. Siegmann, "Research frontiers in magnetic materials at soft X-ray synchrotron radiation facilities," Journal of Magnetism and Magnetic Materials **207,** 7–44 (1999).

[43] H. Padamsee *et al.*, *RF superconductivity for accelerators* (Wiley Online Library, 2008), Vol. 2011.

[44] S. Posen, N. Valles, and M. Liepe, "Radio Frequency Magnetic Field Limits of Nb and Nb 3 Sn," Physical review letters **115,** 047001 (2015).

[45] S. Posen and M. Liepe, "Advances in development of Nb 3 Sn superconducting radio-frequency cavities," Physical Review Special Topics-Accelerators and Beams **17,** 112001 (2014).

[46] Q. Du, M. D. Gunzburger, and J. S. Peterson, "Analysis and approximation of the Ginzburg–Landau model of superconductivity," Siam Review **34,** 54–81 (1992).

[47] H. Gao, "Efficient Numerical Solution of Dynamical Ginzburg-Landau Equations under the Lorentz Gauge," Communications in Computational Physics **22,** 182–201 (2017).

[48] M. Tinkham, *Introduction to superconductivity* (Courier Corporation, 2004).

[49] N. Kopnin, *Theory of nonequilibrium superconductivity* (Oxford University Press, 2001), Vol. 110.

[50] J. Eisenstein, "Superconducting elements," Reviews of Modern Physics **26,** 277 (1954).

[51] B. T. Matthias, T. H. Geballe, and V. B. Compton, "Superconductivity," Reviews of Modern Physics **35,** 1 (1963).

[52] B. W. Maxfield and W. McLean, "Superconducting penetration depth of niobium," Physical Review **139,** A1515 (1965).

[53] V. Novotny and P. Meincke, "Single superconducting energy gap in pure niobium," Journal of Low Temperature Physics **18,** 147–157 (1975).

[54] A. Godeke, D. Cheng, D. Dietderich, P. Ferracin, S. Prestemon, G. Sabbi, and R. Scanlan, "Limits of NbTi and Nb_3Sn, and Development of W&R Bi–2212 High Field Accelerator Magnets," IEEE transactions on applied superconductivity **17,** 1149–1152 (2007).

[55] B. Matthias, T. Geballe, S. Geller, and E. Corenzwit, "Superconductivity of nb 3 sn," Physical Review **95,** 1435 (1954).

[56] M. Hein, *High-temperature-superconductor thin films at microwave frequencies* (Springer Science & Business Media, 1999), Vol. 155.

[57] S. Posen and D. L. Hall, "Nb3Sn superconducting radiofrequency cavities: fabrication, results, properties, and prospects," Superconductor Science and Technology **30,** 033004 (2017).

[58] S. Posen, M. Checchin, A. Crawford, A. Grassellino, M. Martinello, O. Melnychuk, A. Romanenko, D. Sergatskov, and Y. Trenikhina, "Efficient expulsion of magnetic flux in

superconducting radiofrequency cavities for high Q 0 applications," Journal of Applied Physics **119,** 213903 (2016).

[59] R. D. Neidinger, "Introduction to automatic differentiation and MATLAB object-oriented programming," SIAM review **52,** 545–563 (2010).

[60] R. E. Carlson and F. N. Fritsch, "Monotone piecewise bicubic interpolation," SIAM journal on numerical analysis **22,** 386–400 (1985).

[61] G. Dattoli, S. Licciardi, R. Pidatella, and E. Sabia, "Hybrid complex numbers: the matrix version," Advances in Applied Clifford Algebras **28,** 58 (2018).

[62] M. K. Transtrum and J. P. Sethna, "Improvements to the Levenberg-Marquardt algorithm for nonlinear least-squares minimization," arXiv preprint arXiv:1201.5885 (2012).

[63] G. Blatter, M. V. Feigel'man, V. B. Geshkenbein, A. I. Larkin, and V. M. Vinokur, "Vortices in high-temperature superconductors," Reviews of Modern Physics **66,** 1125 (1994).

[64] A. Koshelev, "Depth profile of London length induced by nonuniform scattering rate maximizing breakdown magnetic field in type II superconductors," arXiv preprint arXiv:1901.05584 (2019).

[65] K. Atkinson, "Numerical integration on the sphere," The ANZIAM Journal **23,** 332–347 (1982).